Detection of
New Heavy Charged Gauge Bosons
with the Future CMS Detector

von

Carsten Hof

Diplomarbeit in Physik

vorgelegt der

Fakultät für Mathematik, Informatik und Naturwissenschaften
der Rheinisch-Westfälischen Technischen Hochschule Aachen

im Oktober 2005

angefertigt im

III. Physikalischen Institut A
Prof. Dr. Thomas Hebbeker

Zusammenfassung

Diese Diplomarbeit ist eine Machbarkeitsstudie zur Suche nach neuen geladenen Eichbosonen, basierend auf einem von Altarelli vorgeschlagenen Modell, mit dem CMS Detektor am LHC.

Dieses Modell beschreibt ein schweres Analogon zum Standard Modell W mit identischen Kopplungen, unterdrückter Kopplung an W und Z und unter anderem den Zerfall in ein geladenes Lepton und ein leichtes Neutrino. Dieses Teilchen, generisch als W' bezeichnet, wird im Kanal $W' \rightarrow \mu\nu$ mit Hilfe der vollständigen Detektorsimulation unter Einbeziehung von sich überlagernden Ereignissen (pile-up) entsprechend der Anfangsluminosität des LHC untersucht. Alle Standard-Modell-Untergründe werden berücksichtigt.

Ein solches schweres geladenes Boson kann mit einer integrierten Luminosität von einem Jahr LHC ($10\ \mathrm{fb}^{-1}$) mit dem CMS Detektor in einem Massenbereich von 0.1–4.6 TeV gefunden werden. Mit einer integrierten Luminosität von $300\ \mathrm{fb}^{-1}$ kann dieser Bereich bis auf 6.1 TeV ausgeweitet werden. Sollten keine Signale gefunden werden, so kann mit einem 95%-igen Vertrauensniveau ein W' mit einer Masse kleiner als 4.7 TeV bzw. 6.2 TeV ausgeschlossen werden.

Abstract

In this thesis a feasibility study of the search for a new heavy charged gauge boson according to the Reference Model by Altarelli with the CMS detector at the LHC is presented.

The model assumes the existence of a heavy carbon copy of the Standard Model W with identical couplings, a suppressed coupling to W and Z bosons, and, among others, the decay into a charged lepton and a light neutrino. These particles, generically denoted as W', have been investigated in the decay channel $W' \rightarrow \mu\nu$ using the full detector simulation and including minimum bias events (pile-up) according to the low luminosity phase of the LHC. All Standard Model backgrounds have been considered.

The discovery mass range for such new bosons is determined to be 0.1–4.6 TeV for an integrated luminosity of one year LHC operation (10 fb^{-1}). The range can be expanded to 6.1 TeV with an integrated luminosity of 300 fb^{-1}. If no signs appear 95% CL exclusion limits of 4.7 TeV and 6.2 TeV can be set respectively.

Contents

Chapter 1

Introduction

The principles of basic research, especially in the area of modern particle physics, reflect the human aspiration to gain deep insight into nature. Following Faust's tracks, physicists are questing for the unified theory (Theory of Everything, TOE), which explains the interaction between the "elementary particles" at the level of the fundamental forces, according to the maxim "was die Welt im innersten zusammenhält" [1].

To our today's knowledge four fundamental forces, the electromagnetic, the weak, the strong and the gravitational force, interact between twelve elementary fermionic particles by mediating bosonic particles. All forces except gravity have been implemented in the framework of gauge theories, combined in the "Standard Model of Particle Physics" (SM). The gauge groups model the fundamental degrees of freedom and reflect the importance of the underlying symmetries. The identification of basic symmetries has played a crucial role in the description of the fundamental reactions up to a very precise level. Nevertheless, the Standard Model contains many free parameters to be measured, since they cannot be predicted within the theory. Most physicists think of the SM as an "effective theory" on the way to a more general theory ("You have to be crazy to think the Standard Model is the last truth", Altarelli, 2005).

The Standard Model is unsatisfying in the fact, that it "only" describes, but does not explain things. Hints for theories beyond the Standard Model (BSM) arise from neutrino experiments, where oscillations from one type into another suggest neutrino masses. Another puzzle is the origin of particle masses, which is widely believed to be solved by the Higgs-mechanism.

The energy range, which can be investigated with the Large Hadron Collider (LHC) and its four experiments at CERN, plays an important role in testing the Standard Model and theories beyond. One of the main motivations to study centre of mass energies larger than the 200 GeV attained with the previous Large Electron Positron Collider (LEP) is the last undiscovered particle of the Standard Model: the Higgs spin-0 boson related to the Higgs-mechanism. From electroweak precision experiments and direct searches the allowed mass range for the Higgs mass is constrained to 115–300 GeV. Other signatures for "new" physics are expected to appear at the LHC energy scale: in Supersymmetric Theories (SUSY), where each Standard Model particle has its "Superpartner", the lightest Supersymmetric particle is supposed to have a mass explorable with the LHC.

Most theories beyond the Standard Model are built on an extension of the SM gauge groups. Since bosons are related to the generators of the gauge groups, the models give rise to new heavy charged gauge bosons, but also electrically neutral ones, generically denoted as W' and Z', respectively. Charged bosons decay among other things into a charged lepton accompanied by a neutrino e.g. $W' \to \mu\nu$. Due to the high mass of the bosons the leptons have large momenta and can be distinguished from softer leptons originating from other sources. Thus, the leptonic decays of such new charged gauge bosons lead to clear experimental signatures for the discovery of today unobserved physics.

In this thesis the feasibility of the detection of W' bosons with one of the LHC experiments, the Compact Muon Solenoid (CMS), is studied. Since the detector is optimised for the measurement of muons, the muon plus neutrino final state is used in this study. In preparation of the detector being operational from 2007 onwards, a study with the full detector simulation including underlying events is presented.

After an introduction into the Standard Model and selected theories yielding additional heavy charged gauge bosons, the CMS detector is described. In the following chapter the tools and the model, which are used to perform this search, are explained. Since a high quality reconstruction of high energetic muons and large missing transverse energies is an essential ingredient of this analysis, a separate chapter is dedicated to this topic. In the following the performed selection criteria to distinguish signal from background processes and the used statistical method, which is used for the signal significance determination, are described.

The final aim of the study is the determination of the mass range for the discovery of a W'. If no signatures for new physics appear a 95% exclusion limit is set.

Remarks

At this place units and conventions, which are used in this thesis, are stated. Instead of the *International System of Units* variables are given in the natural units of elementary particle physics by setting

$$\hbar \equiv 1 \qquad \text{and} \qquad c \equiv 1 \tag{1.1}$$

instead of

$$\hbar = 1.0546 \cdot 10^{-34} \text{ Js} \qquad \text{and} \qquad c = 2.9979 \cdot 10^{8} \text{ m/s} .$$

Since the energies in particles physics are tiny compared to daily life ones, physicists defined the unit of an "electron-volt", short eV. It is the energy gained by a particle carrying one elementary electric charge while moving through an electric field with a potential difference of one volt, thus

$$1 \text{ eV} = 1.6022 \cdot 10^{-19} \text{ J}. \tag{1.2}$$

By convention (1.1) all units can be expressed in terms of electron-volt, like distances (eV^{-1}), times (eV^{-1}), masses (eV) or momenta (eV).

The global CMS coordinate system is introduced here, which is used when no other coordinate system is explicitly quoted. The cartesian system is defined with the x-axis pointing towards the center of the LHC ring and perpendicular, directed skywards to the
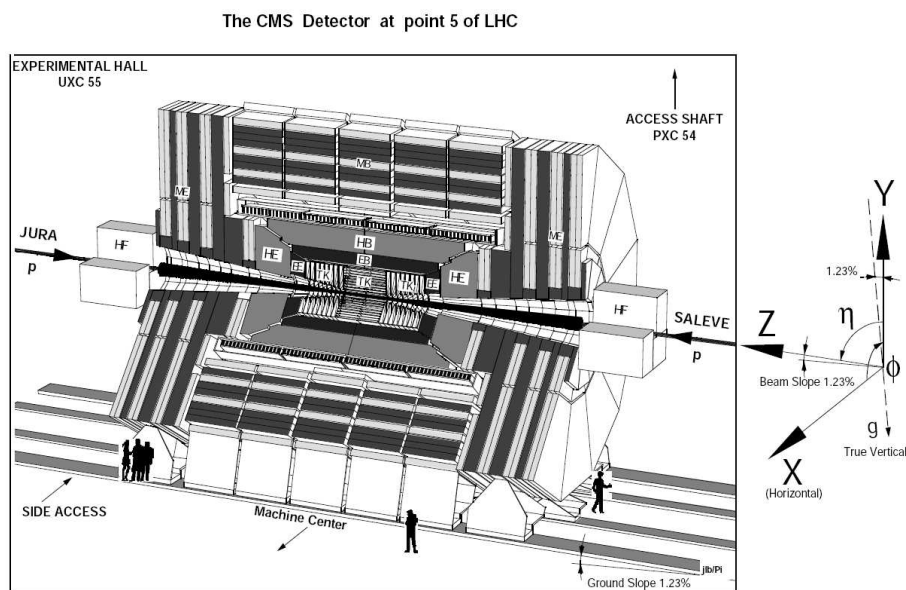
Figure 1.1: *The CMS detetor with the CMS global coordinate system [2].*

surface, the y-axis. The z-axis completes a right-handed system along the beam axis (see figure 1.1). The polar coordinates ϕ / θ are defined in the xy-plane / yz-plane referring to the x-axis / y-axis, respectively:

$$\tan\phi = \frac{y}{x} \qquad \text{and} \qquad \cos\theta = \frac{z}{\sqrt{x^2 + y^2}}. \tag{1.3}$$

Within this coordinate system "transverse" variables, tagged by a subscript "T" like in p_{T}, are defined as the absolute value of the projection of the variable (as vector) onto the xy-plane. The "longitudinal" component, denoted by "L", is the absolute value of the projection along the z-axis.

For a particle with a mass m, energy E and longitudinal momentum component p_{L} the "rapidity" y replaces as natural coordinate in high energy physics the polar angle θ in the following way:

$$y := \frac{1}{2} \ln\left(\frac{E + p_{\mathrm{L}}}{E - p_{\mathrm{L}}}\right). \tag{1.4}$$

It benefits from the fact that a difference in rapidity Δy is invariant under boosts along the z-axis, for example the distribution $\mathrm{d}N/\mathrm{d}y$ is unchanged. For practical issues the rapidity is approximated in the limit $m \ll E$ by the "pseudorapidity" η,

$$\eta := -\ln\tan\left(\frac{\theta}{2}\right). \tag{1.5}$$

Being only dependent on θ the pseudorapidity η can also be defined for particles with unknown mass.

Caution

This work is based on a developing software. All results are achieved with the bugs and preliminary algorithms of this software package, which is and will be developed on the way to a running CMS detector.

Chapter 2

The Standard Model

During the last century the fundamental constituents of matter and the interactions among them have been merged into one model of great beauty and simplicity known as the Standard Model of Particle Physics. All particles seem to be built up from quarks and leptons (see figure 2.1), which interact as point like, structureless, spin-1/2 particles (fermions). The interactions among them can be classified into four categories: gravitation, weak, electromagnetic and strong interaction, where the former can be neglected at distances considered in particle physics. They differ vastly in their range: whereas the electromagnetic and gravitational forces act over infinite distances, weak and strong interactions are limited to a very small region.

Force	Range [m]	Relative strength	Force carrier
Strong force	10^{-15}	1	8 gluons (g)
Electromagnetic force	∞	10^{-2}	photon (γ)
Weak force	10^{-13}	10^{-2}	W, Z^0
Gravitational force	∞	10^{-40}	graviton (?)

Table 2.1: *The fundamental forces with their range and strength (depending on the momentum transfer) and the force carrying bosons.*

Beside the gravitational force, all interactions can be described by local gauge theories, where the forces are carried by fundamental spin-1 gauge bosons. The gravitation is expected to be mediated through a spin-2 boson called graviton, but no direct evidence for this particle could be detected by now. While quarks participate in all interactions, leptons do not take part in strong interactions. The systematics of weak interactions with charged leptons such as the β-decay motivate the pairing of leptons in three families (see section 2.3). This is not only a nice ordering, but reflects basic symmetries of nature. For each generation an additive quantum number can be defined, which is conserved in all today investigated reactions of fundamental particles, except neutrino oscillations (lepton number conservation).

In the Standard Model there is no way to give mass to the gauge bosons. This is no problem for the massless photons and gluons, but in case of the W and Z^0 bosons[1] of the weak force with masses of 80.4 GeV and 91.2 GeV. The problem is solved by spontaneous

---

[1]Both have been discovered in 1983 at the Super Proton-Antiproton Synchrotron Sp$\overline{\text{p}}$S (see [4–10]).
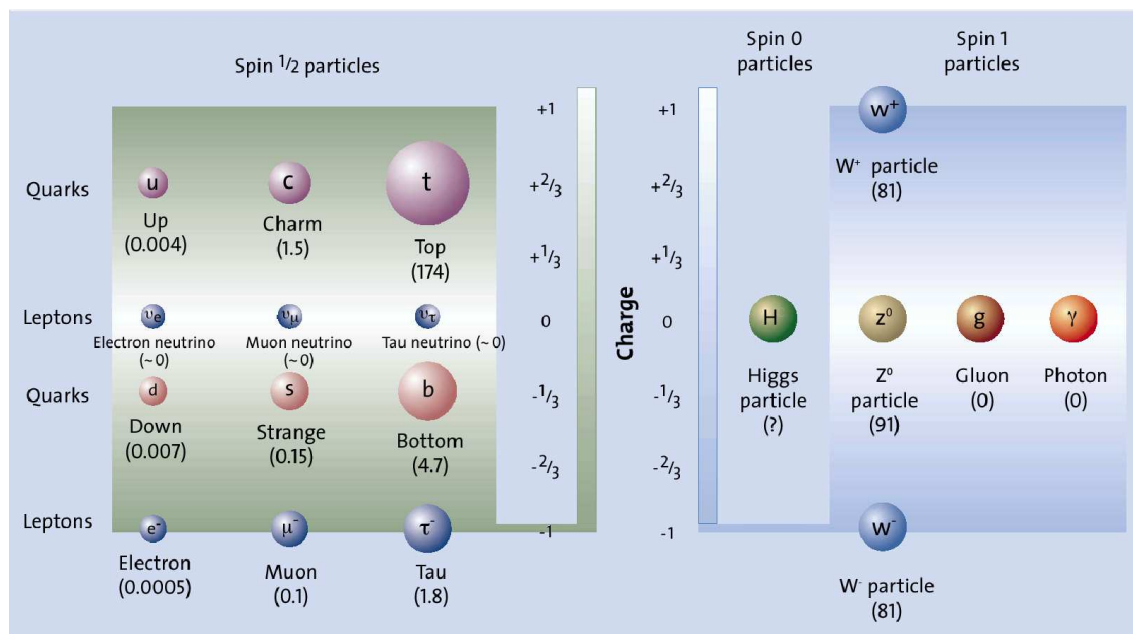
Figure 2.1: *Overview of the Standard Model particles, their charge and mass (in parenthesis, [GeV]) [3].*

symmetry breaking and the so called "Higgs-mechanism". It requires a new fundamental spin-0 particle, the Higgs boson, whose discovery or exclusion is one of the main tasks of the LHC and its experiments.

This chapter gives a brief overview of the Standard Model, enlighting also the fact, that the SM is very successfully *describing* but not *explaining* the surrounding nature in every detail. As this thesis deals with new heavy charged gauge bosons the second part of the chapter is dedicated to extensions, which provide additional heavy gauge bosons.

The Standard Model of elementary particle physics is based on the Glashow-Salam-Weinberg model of the weak interaction and Quantum Chromodynamics (QCD). A favoured supplement is the Higgs-mechanism and the Higgs particle, which provides a way to give mass to particles. For a detailed introduction into the Standard Model see [11–15].

2.1 Local Symmetries and Gauge Invariance

The fundamental particles within the Standard Model are described by space-time coordinate dependent fields $\psi(x)$. Symmetries observed in nature are mathematically reflected by the fact, that the solution of the equation of motion does not change under a certain unitary transformation[2]. In other words: a theory is invariant under a symmetry group G represented by a unitary operator U if the fields $\psi(x)$ and $\psi'(x)$ given by

$$\psi(x) \rightarrow \psi'(x) = U\psi(x) \tag{2.1}$$

---

[2]A transformation U is unitary, if the adjoint operator $U^\dagger$ equals the inverse operator U^{-1}. This is equivalent to the preservation of the inner product (within a Hilbert space) for all vectors x and y: $\langle Ux, Uy \rangle = \langle x, y \rangle$.

follow the same equation of motion.

In the framework of a Lagrangian field theory with a given Lagrangian $\mathcal{L}(\psi_i, \partial_\mu \psi_i)$ as a function of the fields ψ_i and their first derivatives $\partial_\mu \psi_i$ the equation of motion is the Euler-Lagrange equation

$$\frac{\delta \mathcal{L}}{\delta \psi_i} = \partial_\mu \left(\frac{\delta \mathcal{L}}{\delta(\partial_\mu \psi_i)} \right). \tag{2.2}$$

It can be derived by minimizing the action S, which is a functional of ψ_i and $\partial_\mu \psi_i$

$$S = \int d^4x \, \mathcal{L}(\psi_i, \partial_\mu \psi_i). \tag{2.3}$$

A symmetry acting in the way

$$\psi \to \psi + \delta\psi, \qquad \partial_\mu \psi_i \to \partial_\mu \psi_i + \delta \partial_\mu \psi_i, \qquad \mathcal{L} \to \mathcal{L} + \delta\mathcal{L} =: \mathcal{L} + \alpha \partial_\mu \mathcal{J}^\mu(x) \tag{2.4}$$

is exact if

$$\delta\mathcal{L} = 0. \tag{2.5}$$

Associated with each exact symmetry is a so called Noether current $j^\mu(x)$ and a corresponding charge Q

$$j^\mu(x) = \frac{\delta \mathcal{L}}{\delta(\partial_\mu \psi)} \delta\psi - \mathcal{J}^\mu \qquad \text{and} \qquad Q = -i \int d^3x \, j^0(x), \tag{2.6}$$

which are conserved

$$\partial_\mu j^\mu = 0 \qquad \text{and} \qquad \frac{dQ}{dt} = 0 \qquad \text{if} \qquad \delta\mathcal{L} = 0. \tag{2.7}$$

The gauge symmetries of the Standard Model are all local ones. From an aesthetic point of view this appears much more plausible, since global symmetries act on different space-time points in an exact manner - no matter how far they are separated or how they are causally connected. The local symmetries are implemented by making parameters of the gauge group G and thus their representations $U = U(x)$ space-time dependent. The elements $U(x)$ of G can be expressed in terms of their local, i.e. space-time dependent generators $\Lambda_a(x)$

$$\psi(x) \to U(x)\psi(x) = e^{i\epsilon_a \Lambda_a(x)}\psi(x). \tag{2.8}$$

They satisfy the Lie-Algebra with the structure constants f_{abc}

$$[\Lambda_a, \Lambda_b] = i f_{abc} \Lambda_c, \tag{2.9}$$

whose knowledge is sufficient to construct the whole group.

Any Lagrangian containing derivatives, like the Lagrangian for a free particle

$$\mathcal{L}_{\text{free}} = \overline{\psi}(i\gamma_\mu \partial^\mu - m)\psi, \tag{2.10}$$

is not invariant under local gauge transformations[3]. A solution known as minimal substitution is the replacement of the derivative ∂_μ by a covariant derivative D_μ, which satisfies

$$D_\mu \psi(x) \to e^{i\epsilon_a \Lambda_a(x)} D_\mu \psi(x). \tag{2.11}$$

---

[3]$\partial_\mu \psi(x) \to e^{i\epsilon_a \Lambda_a(x)} \partial_\mu \psi(x) + i\epsilon_a \partial_\mu \Lambda_a(x) e^{i\epsilon_a \Lambda_a(x)} \psi(x)$ spoils gauge invariance.

For this purpose it is necessary to introduce a vector field A_μ

$$D_\mu \psi(x) := (\partial_\mu + i\epsilon_a A_\mu(x))\psi(x), \qquad (2.12)$$

which transforms under the unitary operator $U(x)$ (see eqation (2.8)) as

$$A_\mu(x) \rightarrow A_\mu - \partial^\mu \Lambda_a(x). \qquad (2.13)$$

In addition a kinematic term for the field A_μ has to be added to the Lagrangian.

The process of restoring the gauge invariance of the Lagrangian and choice of the vector field A_μ is called gauging.

Aiming towards the understanding of quarks and leptons and their interactions in a framework of a local gauge theory, one has to discover the underlying fundamental symmetries of the different forces, i.e. to identify the basic degrees of freedom on which the symmetries operate. As will be discussed in the following sections the Standard Model is based on the gauge group

$$SU(3)_C \times SU(2)_L \times U(1)_Y.$$

The former term describes the colour degree of freedom of the theory of quarks, quantum chromodynamics. The rest reflects the symmetry of the electroweak unification of the weak and electromagnetic force, with its charges of weak isospin T_3 and electric charge Q, respectively. They are connected to the quantum number Y (hypercharge) related to the $U(1)_Y$ symmetry via the Gell-Mann-Nishijima formula

$$Q = T_3 + \frac{Y}{2}. \qquad (2.14)$$

2.2 Quantum Chromodynamics

The introduction of quarks[4] (spin-1/2, fractional charge) as constituents of hadrons, divided into (anti-)baryons as three-(anti-)quark-states and also mesons as quark-antiquark-states, can describe the huge variety of particles (Gell-Mann and Zweig). The ordering of the spectrum in the baryon-meson world is achieved by the assignment of a degree of freedom to the quarks known as flavour. This global flavour symmetry, which is also retrieved in the lepton sector ("quark-lepton-symmetry"), is described by the gauge group $SU(6)$. Due to the different charges and masses of the quarks and leptons the flavour symmetry is only an approximate one.

Historically, the concept of quark substructures showed two significant problems: first, free quarks have never been observed and second, baryons with three equal quarks, such as δ^{++} violate the Pauli principle. In 1964, only one year after the proposal of the quark-model, this drawback was bypassed by the introduction of a new "hidden" quantum number, called colour, which can hold the three values red (R), green (G) and blue (B) plus their three counterparts $(\overline{R}, \overline{G}, \overline{B})$. (Anti-)quarks carry (anti-)colour, whereas the known

---

[4]Many famous physicists denied the existence of quarks as particles for a long time and treated them only as a formal concept. In 2004 D. J. Gross, H. D. Politzer and F. Wilczek won the Nobel prize for the discovery of the asymptotic freedom in the theory of strong interactions.

hadrons appear as "colourless". Thus the hadrons transform as colour-singlets under this new degree of freedom based on the gauge group $SU(3)_C$. In general colour can be interpreted as the charge of the strong interaction. In analogy to optics a mixture of (anti-)red, (anti-)green and (anti-)blue quarks in case of baryons or colour plus anti-colour in case of mesons results in a "white" particle. The non-observability of free quarks is interpreted in such a way, that only colourless (white) particles can be seen. Experimental evidence has been gained for example by the measurement of the cross-section ratio

$$R := \frac{\sigma(e^- e^+ \rightarrow hadrons)}{\sigma(e^- e^+ \rightarrow \mu^- \mu^+)} = N_C \sum_{2m_q < E_{CMS}} Q_q^2, \tag{2.15}$$

which depends on the "colour factor" N_C, i.e. the number of colours and Q_q the charge of the quarks being available at a certain centre of mass energy E_{CMS}. The data taken with several experiments require $N_C \equiv 3$ (see figure 2.2).
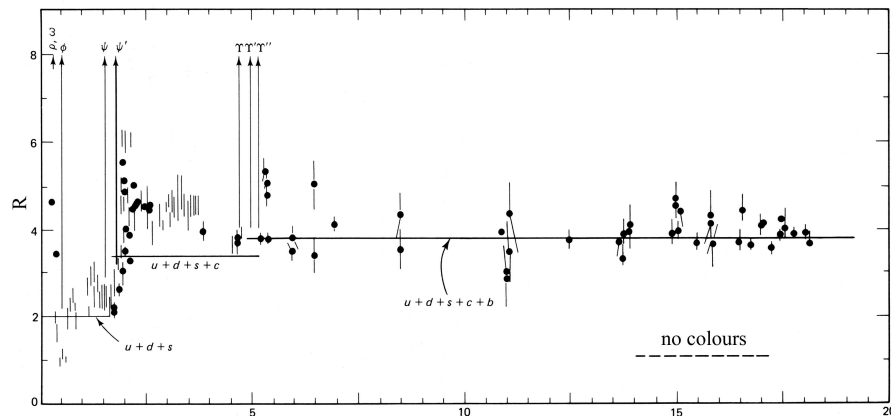
Figure 2.2: *The cross section ratio R extracted from experimental data [11].*

While the strength of the electromagnetic interactions, described by the fine structure constant α, increases with higher momentum transfer Q^2, the coupling constant of the strong interaction α_s decreases. This behaviour, called "asymptotic freedom", states that at small distances quarks behave like free particles. It describes also why it is not possible to see free coloured particles (confinement).

After the success of local gauge theories in the field of electromagnetic and weak interactions (see section 2.3) theorists tried to construct a theory of strong interactions between quarks, which is based on local gauge transformations with colour as the interaction charge.

In 1973 Gross and Wilczek discovered that non-abelian gauge groups can describe theories with asymptotic freedom and managed to formulate the theory of quantum chromodynamics (QCD) based on the local gauge group $SU(3)_C$. Strong interactions stay invariant under the colour transformation

$$U_C(x) = exp\left(i \frac{g_s}{2} \sum_{j=1}^{8} \lambda_j \beta_j(x) \right). \tag{2.16}$$

These are described by eight independent rotations β_j in the colour space, by the QCD coupling constant g_s and by the Gell-Mann-matrices λ_j. To guarantee the invariance of

the equations of motion eight additional vector fields G_j^μ and a covariant derivative D^μ have to be introduced:

$$D^\mu = \partial^\mu + i\frac{g_s}{2}\sum_{j=1}^{8} \lambda_j G_j^\mu.$$ (2.17)

The particles related to the vector fields are the eight different coloured gluons, which mediate the strong interaction. The first evidence for gluons was observed at the PETRA collider in 1979 in three jet events, where one jet originates from a massless radiated gluon. In contrast to photons, which electrically neutral, gluons carry the interaction charge (colour). Thus additional terms appear in the transformed gluon fields performing a rotation in the colour space (last term of (2.19)):

$$\psi(x) \quad \rightarrow \quad U_{\rm C}\,\psi(x)$$ (2.18)

$$G_j^\mu(x) \quad \rightarrow \quad G_j^\mu(x) - \partial^\mu\beta_j(x) - g_{\rm S}\,f_{jkl}\,\beta_k(x)\,G_l^\mu(x).$$ (2.19)

2.3   The GSW-Model of Electroweak Interactions

Symmetries, broken or not, like the broken flavour symmetry or the exact colour symmetry, do not only appear in QCD, but the way they are hidden in weak interactions makes them less obviously discernible. While the flavour symmetry is visible in the spectrum of particles and their approximate mass degeneracy, the observed universality of the Fermi coupling of weak-decay processes suggests the existence of a hidden symmetry in weak interactions. This is an outstanding fact since the weakly interacting particles have widely varying masses. The symmetry manifests itself not through the existence of degenerated multiplets, but through broken local symmetries.

In the 1960s Glashow, Salam and Weinberg (see [16–18]) were the first, who realised a unified theory of weak and electromagnetic interactions in the framework of a renormalizable field theory (GSW-Model). It is based on the gauge group $SU(2)_{\rm L}\times U(1)_{\rm Y}$.

In order to describe the interaction they assigned the quarks and leptons to representations of the gauge groups arranged in multiplets as shown in table 2.2. As seen first in β-decays by Wu et al. [19] parity is violated maximally in weak interactions and weak charged currents couple only to left-handed particles, where the handedness is determined by the projection operators

$$P_{\rm L} = \frac{1}{2}(1 - \gamma_5) \qquad \text{and} \qquad P_{\rm R} = \frac{1}{2}(1 + \gamma_5).$$ (2.20)

This experimental result is included in the Standard Model by the assignment of the left-handed fermions to $SU(2)_{\rm L}$ doublets, while the right-handed fermions transform as singlets trivial under $SU(2)_{\rm L}$.

Fermions (Spin 1/2)							
	Generation			Quantum Number			
	1.	2.	3.	Q	T	T_3	Y
Quarks	$\begin{pmatrix} u \\ d' \end{pmatrix}_{\mathrm{L}}$	$\begin{pmatrix} c \\ s' \end{pmatrix}_{\mathrm{L}}$	$\begin{pmatrix} t \\ b' \end{pmatrix}_{\mathrm{L}}$	2/3 −1/3	1/2 1/2	1/2 −1/2	1/3 1/3
	u_{R} $d_{\mathrm{R'}}$	c_{R} $s_{\mathrm{R'}}$	t_{R} $b_{\mathrm{R'}}$	2/3 −1/3	0 0	0 0	4/3 −2/3
Leptons	$\begin{pmatrix} \nu_e \\ e \end{pmatrix}_{\mathrm{L}}$	$\begin{pmatrix} \nu_\mu \\ \mu \end{pmatrix}_{\mathrm{L}}$	$\begin{pmatrix} \nu_\tau \\ \tau \end{pmatrix}_{\mathrm{L}}$	0 −1	1/2 1/2	1/2 −1/2	−1 −1
	e_{R}	μ_{R}	τ_{R}	−1	0	0	−2

Bosons (Spin 1)						
Interaction	Gauge Boson		Q	T	T_3	Y
Electromagnetic	γ		0	0	0	0
Weak	Z^0		0	1	0	0
	W		1	1	±1	0
Strong	$g_{1\dots8}$		0	0	0	0

Table 2.2: *The particles of the Standard Model with their electroweak quantum numbers. Fermions are assigned to left-handed doublets and right-handed singlets. The primes on the left-handed down-type-quarks indicate, that these are not the physical mass eigenstates, but the electroweak eigenstates. They are related via the 3×3 Cabbibo-Kobayashi-Maskawa-matrix. Q denotes the electromagnetic charge, Y the weak hypercharge and T_3 the third component of the weak isospin, T.*

Except for the Higgs sector (see below) the Lagrangian is completely dictated by (the desired feature of) gauge invariance and renormalisability[5]. It can be separated into the following parts:

$$\mathcal{L}_{\mathrm{GSW}} = \mathcal{L}_{\mathrm{fermion}} + \mathcal{L}_{\mathrm{gauge}} + \mathcal{L}_{\mathrm{Higgs}} + \mathcal{L}_{\mathrm{Yukawa}} \tag{2.21}$$

The first term describes the kinematic of the free fermion fields and their interaction with the gauge fields. It has the form

$$\mathcal{L}_{\mathrm{fermion}} = i\overline{\psi}\gamma^\mu D_\mu \psi \tag{2.22}$$

---

[5]Renormalisability reflects the fact, that the predicted interaction probabilities stay finite by including higher order corrections and self-couplings of bosons. As proved by 't Hooft local gauge invariance is a condition for the renormalisability of gauge theories with massless and massive gauge bosons. It can be proved, that the Lagrangian can only contain terms whose dimension is less than or equal to 4.

with ψ as the combined spinor of all fermionic fields and D_μ as the covariant derivative of the $SU(2)_L \times U(1)_Y$ gauge group[6]

$$\psi = \begin{pmatrix} \nu_{e_L} \\ e_L \\ \vdots \\ t_R \end{pmatrix}, \qquad D_\mu = \partial_\mu + i\,g\,\frac{T_a}{2}W_\mu^a + i\,g'\,B_\mu Y. \tag{2.23}$$

Since any arbitrary special unitary group SU(N) is built up by $N^2 - 1$ generators and the unitary groups U(N) by N^2 generators, the gauge group $SU(2)_L \times U(1)_Y$ contains 3 + 1 gauge fields. These are denoted by W_μ^a ($a = 1, 2, 3$) and B_μ. The variables g and g' represent the coupling constants of the unified electroweak theory[7] and the matrices T_a (Pauli matrices) and Y, the generators of the corresponding groups $SU(2)_L$ and $U(1)_Y$.

The boson fields W, Z^0 and the massless photon (A_μ) corresponding to the observed mass eigenstates are the linear combinations

$$W_\mu^\pm = \frac{1}{\sqrt{2}}\left(W_\mu^1 \mp iW_\mu^2\right) \tag{2.24}$$

$$Z_\mu = -B_\mu \sin\theta_W + W_\mu^3 \cos\theta_W \tag{2.25}$$

$$A_\mu = B_\mu \cos\theta_W + W_\mu^3 \sin\theta_W, \tag{2.26}$$

where the electroweak mixing angle (Weinberg angle) is given by the coupling constants

$$\cos\theta_W = \frac{g}{\sqrt{g^2 + g'^2}} \qquad \text{and} \qquad \sin\theta_W = \frac{g'}{\sqrt{g^2 + g'^2}}. \tag{2.27}$$

By inserting the fields $W_\mu^\pm$, Z_μ and A_μ into (2.22) one receives a representation of the interaction of gauge bosons and fermions by the exchange of currents. By construction the charged W bosons couple only to left-handed particles and right-handed antiparticles.

With the introduction of the covariant derivative (2.23) and the addition of a kinematic term for the gauge bosons (see section 2.1), the Lagrangian (2.21) contains terms, which are bilinear in the gauge fields and thus describe the interactions among them. The occurrence of such terms is not trivial, since they do not occur in case of the photon.

$$\mathcal{L}_{\text{gauge}} = -\frac{1}{4}W_{\mu\rho}W^{\mu\rho} + B_{\mu\rho}B^{\mu\rho} \tag{2.28}$$

using the field tensors

$$W_{\mu\rho} = \left(\partial_\mu W_\rho^a - \partial_\rho W_\mu^a - g\epsilon_{abc}W_\mu^b W_\rho^b\right)T_a \tag{2.29}$$

$$B_{\mu\rho} = \partial_\mu B_\rho - \partial_\rho B_\mu. \tag{2.30}$$

T_a are the generators and ϵ_{abc} are the structure constants of the $SU(2)_L$ describing the self interaction of the gauge fields.

Up to now the electroweak theory is a well formulated gauge theory describing the discovered particle spectrum, especially the gauge bosons W and Z^0. But there is one

---

[6]Equation (2.23) is only a symbolic notation! W_μ^a acts only on the left-handed fermions (isospin doublets), while B_μ acts on both, right- and left-handed particles.

[7]The unification is not perfect, since it contains not only *one* coupling constant.

problem: none of the particles have masses, neither the fermions nor the massive gauge bosons. The simple addition of mass terms like $m^2 Z_\mu Z^\mu$ to the Lagrangian spoils local gauge invariance. One solution is the spontaneous symmetry breaking via the Higgs-mechanism.

2.4 The Higgs-Mechanism

By the inclusion of a scalar field (Higgs boson) into the model the short range of the weak interaction can be accommodated by giving mass to the gauge bosons. Via the Higgs-mechanism the $\mathrm{SU(2)_L} \times \mathrm{U(1)_Y}$ symmetry is broken spontaneously without destroying the gauge invariance of the Lagrangian. Since spontaneous symmetry breaking also arises in Left-Right Symmetric Models (see chapter 3) to break parity (and to give mass to particles), the formalism is discussed in greater detail in case of the Standard Model Higgs boson.

In the simplest nontrivial implementation the Higgs boson field ϕ transforms as an isospin doublet under the gauge group $\mathrm{SU(2)_L}$.

$$\Phi(x) = \begin{pmatrix} \phi^+(x) \\ \phi^0(x) \end{pmatrix} = \frac{1}{\sqrt{2}} \begin{pmatrix} \phi_1(x) + i\phi_2(x) \\ \phi_3(x) + i\phi_4(x) \end{pmatrix}. \tag{2.31}$$

The Higgs field couples to the gauge bosons ($\mathcal{L}_{\mathrm{Higgs}}$) as well as to the fermions ($\mathcal{L}_{\mathrm{Yukawa}}$)

$$\mathcal{L}_{\mathrm{Higgs}} = (\mathbf{D}_\mu \Phi(x))^\dagger (\mathbf{D}^\mu \Phi(x)) - V(\Phi) \tag{2.32}$$

$$\mathcal{L}_{\mathrm{Yukawa}} = \overline{\psi}\, \Phi_i(x)\, \mathbf{C_i}\, \psi + h.c. \qquad (i = 1, 2), \tag{2.33}$$

where the matrix $\mathbf{C_i}$ contains the masses of the fermions i.e. the strength of the coupling to the Higgs field. The potential $V(\Phi)$,

$$V(\Phi) = \mu^2 \Phi^\dagger \Phi + \lambda (\Phi^\dagger \Phi)^2 \tag{2.34}$$

is chosen to be symmetric $V(\Phi) = V(-\Phi)$, so that only even powers of Φ occur and higher orders are neglected. To have a reasonable theory the potential has to tend to infinity for the limit $\Phi \to \pm\infty$, thus $\lambda > 0$ and must have a lower bound. As shown in figure 2.3 the potential has only a non-trivial minimum for $\mu^2 < 0$, which is given by

$$\Phi^\dagger \Phi = -\frac{\mu^2}{2\lambda} =: \frac{v^2}{2}. \tag{2.35}$$

Only in this case it is possible to break the $\mathrm{SU(2)_L} \times \mathrm{U(1)_Y}$ symmetry. A possible solution, which sets the vacuum expectation value of the charged Higgs field ϕ^+ to zero and guarantees the photon mass to be zero is

$$\Phi(x) = \frac{1}{\sqrt{2}} \begin{pmatrix} 0 \\ \rho(x) \end{pmatrix} = \frac{1}{\sqrt{2}} \begin{pmatrix} 0 \\ v + h(x) \end{pmatrix}. \tag{2.36}$$

Then the neutral part of the Higgs field can be expressed in terms of the vacuum expectation value v and a scalar field $h(x)$. By the special choice of the vacuum expectation the $\mathrm{SU(2)_L}$ as well as the $\mathrm{U(1)_Y}$ is broken, but the $\mathrm{U(1)_{em}}$ symmetry remains untouched.
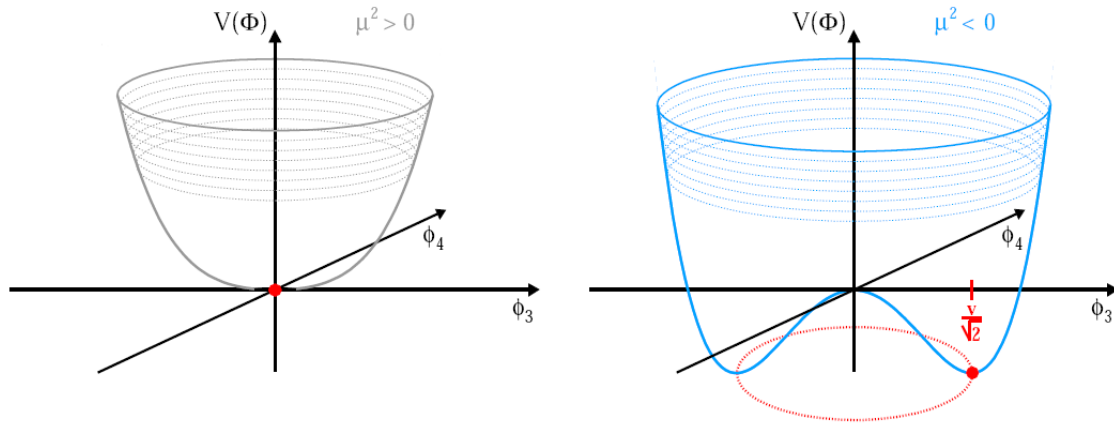
Figure 2.3: *The Higgs potential [20]. A non trivial minimum exists only for $\mu^2 < 0$.*

The Goldstone boson arising naturally in a broken symmetry is absorbed as longitudinal degree of freedom of the massive gauge bosons W and Z^0.

Replacing $\Phi(x)$ in equation (2.32) by (2.36) mass terms like $\frac{1}{4}g^2v^2W_\mu^+W^{-\mu}$ arise and give mass to the weak gauge bosons:

$$m_{Z^0} = \frac{1}{2}\sqrt{g^2 + g'^2}\,v, \qquad m_W = \frac{1}{2}gv, \qquad m_\gamma = 0, \qquad m_{\text{H}} = v\sqrt{2\lambda}. \qquad (2.37)$$

The interaction of the fermions with the Higgs field leads to mass terms and to couplings to the Higgs field $h(x)$, which are proportional to the fermion mass ($\mathcal{L}_{\text{Yukawa}}$).

Chapter 3

Beyond the Standard Model

The Standard Model is up to now in excellent agreement with experiments. Nevertheless it contains numerous free parameters such as Yukawa couplings. Vicariously, some of the mysteries of the SM should be mentioned here:

- **Gauge sector:**
  The Standard Model is based on three different gauge groups associated with arbitrary coupling constants. From the theoretical and aesthetic point of view one unified gauge group, which contains the SM as a subgroup, seems to be much more satisfying. In addition such a theory should also be able to predict the parameters such as the coupling constants.

- **Fermion sector:**
  The assignment of the left-handed fermions to doublets and the right-handed to singlets is only justified by the fact, that it fits to data. There is no explanation why charged weak currents are strictly left-handed as well why there are three fermion generations. Their mixing and the masses given through Yukawa couplings stay arbitrary in the SM.
  The hierarchical pattern of the quark masses m_t, $m_b \gg m_c$, $m_s \gg m_u$, m_d, but also for charged leptons $m_\tau \gg m_\mu \gg m_e$ (for neutrinos the mass hierarchy still has to be confirmed) might be hints for additional hidden symmetries.

- **Neutrino mass:**
  Today's experiments only yield upper limits for neutrino masses, but the recently observed neutrino oscillations require neutrinos to have a non vanishing mass [21]. In the Standard Model a neutrino mass can not be implemented ad hoc. By choice of the multiplets there is no simple theoretical solution. Since Dirac neutrinos[1] are not foreseen in the Standard Model, they can only be added to the Standard Model as gauge singlets, which would naturally result in neutrino masses of the order of their charged counterparts [22]. Since there are no gauge singlet or triplet Higgs scalars, also Majorana masses[2] cannot be generated either [22]. However, it is possible to add terms to the Lagrangian, which result in neutrino masses, but they predict a new mass scale beyond the SM [15].

---

[1]Dirac particles are distinguishable from their antiparticles.
[2]Majorana particles are their own antiparticles.

- **Higgs Problem:**

  As shown in section 2.4 the choice of the Higgs sector and the vacuum expectation value is quite arbitrary. Beside that there are more fundamental problems: due to quantum loop corrections the mass of the Higgs should be naturally in the order of the Planck scale (hierarchy problem). Unless there appears no new physics at the TeV-scale, a light Higgs favoured by LEP data cannot be explained [15].

- **Others:**

  Gravitation is still far outside the Standard Model, since its addition spoils the feature of renormalisability. Theories beyond the Standard Model, like String Theories, try to address these unification of local gauge invariance and the principle of equivalence. Another puzzle of nature is the quantisation of the electric charge. One would expect, that a fundamental theory predicts the value of the elementary electric charge.

Thus to judge the meaning and importance of tests, which stress the Standard Model, it is necessary to work in a more general framework and be aware in which direction it can be modified.

The following section presents some of the extensions, which are interesting in the context of a W' search and their physical motivation. As one of the favoured models the Left-Right-Symmetric Model will be discussed in detail.

3.1   Left-Right-Symmetric Models

Within the Standard Model the origin of parity violation in weak interactions stays unexplained. A priori the multiplets are explicitly designed to break parity in the weak sector. As displayed in table 2.2 the left-handed particles are assigned to doublets, whereas the right-handed particles do not participate in weak interactions, since they are $SU(2)_L$ singlets. The introduction of parity violation within the Standard Model has nothing to do with the spontaneous symmetry breaking of the gauge groups or an other mechanism, but has been included by hand.

Left-Right-Symmetric Models (LRSM) [23–25] address this problem and provide an attractive extension of the Standard Model (for a review see [15, 22]). The general feature of these models is the intrinsic exact parity symmetry of the Lagrangian and an additional $SU(2)$ gauge group, resulting in an observable W' (and Z'). To match the low-energy behaviour of maximum parity violation in weak interactions (see section 2.3), the symmetry is spontaneously broken by a scalar Higgs field.

In addition LRSM incorporate full quark-lepton symmetry and turn the quantum number of the $U(1)$ from hypercharge Y to the value of baryon-minus-lepton number $B-L$. Finally, in choosing an appropriate Higgs sector the theory gives a natural explanation for the smallness of the neutrino masses, by relating it to the observed suppression of V + A currents. Variants of the model can be derived from Grand Unified Theories, Superstring inspired models or other theories based on extended gauge groups, which contain the LSRM as a subgroup.

3.1.1 Technical Realisation

In order to remedy the apparent arbitrariness of nature to have only strictly left-handed couplings in weak interactions, the electroweak gauge group of the Standard Model is extended by a a right-handed sector (the strong sector remains untouched). The simplest realisation is a Left-Right-Symmetric Model. It is based on the gauge group

$$SU(2)_{\mathrm{L}} \times SU(2)_{\mathrm{R}} \times U(1)_{\widetilde{Y}}. \tag{3.1}$$

The SM fermion doublets are mirrored by arranging the right-handed singlets of the Standard Model together to form another SU(2) doublet. In the lepton sector this can only be done by predicting a neutrino singlet ν_{R} for each generation, which is a massive Majorana particle (see below)

$$u_{\mathrm{R}}, d_{\mathrm{R}} \rightarrow \begin{pmatrix} u_{\mathrm{R}} \\ d_{\mathrm{R}} \end{pmatrix}; \qquad \nu_{\mathrm{R}}, l_{\mathrm{R}} \rightarrow \begin{pmatrix} \nu_{\mathrm{R}} \\ l_{\mathrm{R}} \end{pmatrix}. \tag{3.2}$$

Both doublets cannot be assigned to the same SU(2) gauge group, since this would result in a vector current instead of the observed V - A current in weak interactions. Because of the right-handedness of the fermions the group is indexed by an "R". The according quantum numbers are shown in table 3.1.

The quantum number of the $U(1)_{\widetilde{Y}}$ can be determined by taking into account, that the right- and left-handed fermions are assigned to different SU(2) transformations, but have the same electric charge. Thus the U(1) acts on both of them in the same manner. This results in the modified Gell-Mann-Nishijima formula

$$Q = T_{3\mathrm{L}} + T_{3\mathrm{R}} + \frac{1}{2}(B - L) \tag{3.3}$$

with $T_{3\mathrm{R},3\mathrm{L}}$ as third component of the right and left isospin and Q as the charge matrix. Thus computing $\widetilde{Y}$ for right- and left-handed quarks and leptons:

$$\text{Quarks:} \quad \begin{pmatrix} \frac{1}{2} & 0 \\ 0 & -\frac{1}{2} \end{pmatrix} + \begin{pmatrix} \frac{1}{2}\widetilde{Y}_l & 0 \\ 0 & \frac{1}{2}\widetilde{Y}_l \end{pmatrix} = \begin{pmatrix} q_{\nu_{\mathrm{R,L}}} & 0 \\ 0 & q_{l_{\mathrm{R,L}}} \end{pmatrix} \stackrel{!}{=} \begin{pmatrix} 0 & 0 \\ 0 & -1 \end{pmatrix} \tag{3.4}$$

$$\text{Leptons:} \quad \begin{pmatrix} \frac{1}{2} & 0 \\ 0 & -\frac{1}{2} \end{pmatrix} + \begin{pmatrix} \frac{1}{2}\widetilde{Y}_q & 0 \\ 0 & \frac{1}{2}\widetilde{Y}_q \end{pmatrix} = \begin{pmatrix} q_{u_{\mathrm{R,L}}} & 0 \\ 0 & q_{d_{\mathrm{R,L}}} \end{pmatrix} \stackrel{!}{=} \begin{pmatrix} +2/3 & 0 \\ 0 & -1/3 \end{pmatrix} \tag{3.5}$$

$$\Rightarrow \widetilde{Y}_l = -1 \qquad \text{and} \qquad \widetilde{Y}_q = 1/3. \tag{3.6}$$

Comparing this result with the difference of baryon B and lepton number L one ends up in the equation

$$\widetilde{Y} = B - L. \tag{3.7}$$

Thus, the quantum number of the U(1)-generator can be identified with a physical meaningful quantity, compared to the hypercharge Y in the Standard Model.

Fermions (Spin 1/2)						
	Multiplets	Quantum Number				
		T_{L}	$T_{3\mathrm{L}}$	T_{R}	$T_{3\mathrm{R}}$	$\widetilde{Y} = B - L$
Quarks	$\begin{pmatrix} u \\ d' \end{pmatrix}_{\mathrm{L}}$	1/2 1/2	1/2 −1/2	0 0	0 0	1/3 1/3
	$\begin{pmatrix} u \\ d' \end{pmatrix}_{\mathrm{R}}$	0 0	0 0	1/2 1/2	1/2 −1/2	1/3 1/3
Leptons	$\begin{pmatrix} \nu \\ l \end{pmatrix}_{\mathrm{L}}$	1/2 1/2	1/2 −1/2	0 0	0 0	−1 −1
	$\begin{pmatrix} \nu \\ l \end{pmatrix}_{\mathrm{R}}$	0 0	0 0	1/2 1/2	1/2 −1/2	−1 −1

Table 3.1: *The particles of the Left-Right-Symmetric Model with their quantum numbers. The left-handed doublets transform trivial under the right-handed SU(2) and vice versa. For the sake of clearness the flavour index as well as the colour index of the quark doublets have been dropped.*

Similar to the Standard Model the fermionic Lagrangian is uniquely fixed by gauge invariance. It can be separated in a right-handed and left-handed part by collecting the right- and left-handed fields in spinors ψ_{R} and ψ_{L}, respectively.

$$\mathcal{L}_{\mathrm{fermion}} = i\overline{\psi}_{\mathrm{L}}\gamma^{\mu}D_{\mathrm{L}\mu}\psi_{\mathrm{L}} + i\overline{\psi}_{\mathrm{R}}\gamma^{\mu}D_{\mathrm{R}\mu}\psi_{\mathrm{R}} \tag{3.8}$$

with the left- and right-handed covariant derivative

$$D_{\mathrm{L}\mu} = \partial_{\mu} + i\,g_{\mathrm{L}}\,\frac{\vec{T}_{\mathrm{L}}}{2}\cdot\vec{W}_{\mathrm{L}\mu} + i\,g'\,\frac{B-L}{2}\,B_{\mu} \tag{3.9}$$

$$D_{\mathrm{R}\mu} = \partial_{\mu} + i\,g_{\mathrm{R}}\,\frac{\vec{T}_{\mathrm{R}}}{2}\cdot\vec{W}_{\mathrm{R}\mu} + i\,g'\,\frac{B-L}{2}\,B_{\mu} \tag{3.10}$$

As stated before the Lagrangian is completely invariant under the interchange L ↔ R. The introduction of a Higgs sector is necessary to give mass to the fermions and thus add terms proportional to $\overline{\psi}\Phi\psi$ to the Lagrangian. The simplest solution within LRSM is Φ as a 2×2 matrix, whose transformation properties are dictated by ψ_{L}, ψ_{R}. The Higgs field Φ as well as $\widetilde{\Phi} := T_2\,\phi^*\,T_2$ transform as doublets under $\mathrm{SU(2)_R}$ and $\mathrm{SU(2)_L}$ and trivial under $\mathrm{U(1)_{B\text{-}L}}$, so that the most general coupling of the fermions to ϕ is given by

$$\mathcal{L}_{\mathrm{Yukawa}} = -\sum_{i,j}\left\{\overline{\psi}_{\mathrm{L}i}\,\Gamma^{\psi}_{ij}\,\Phi\,\psi_{\mathrm{R}j} + \overline{\psi}_{\mathrm{L}i}\,\Delta^{\psi}_{ij}\,\widetilde{\Phi}\,\psi_{\mathrm{R}j} + h.c.\right\}, \tag{3.11}$$

where i and j denote the flavour indices and Γ^{ψ}_{ij} and Δ^{ψ}_{ij} describe the Yukawa coupling to the Higgs i.e. the mass of the particles.

The charge of the Higgs fields can be determined from the modified Gell-Mann-Nishijima formula (3.3) similar to equation (3.4)

$$Q\Phi = \left[\frac{1}{2}T_3, \Phi\right] = \begin{pmatrix} 0 \cdot \phi_{11} & \phi_{12} \\ -\phi_{21} & 0 \cdot \phi_{22} \end{pmatrix} \tag{3.12}$$

using

$$\Phi = \begin{pmatrix} \phi_{11} & \phi_{12} \\ \phi_{21} & \phi_{22} \end{pmatrix} \qquad \text{and} \qquad \widetilde{Y}(\Phi) = 0. \tag{3.13}$$

Therefore ϕ_{11} and ϕ_{22} are electrically neutral scalars.

3.1.2 Spontaneous Parity Breaking

Before discussing the spontaneous symmetry breaking of parity, a sufficient definition for parity within Left-Right-Symmetric Models is given. There is an obvious symmetry: every left-handed field in the fermion sector has a right-handed counterpart and also the gauge bosons $\vec{W}_L$ and $\vec{W}_R$ correspond to each other. A mathematical formulation of this transformation, interpreted as parity transformation, is

$$\vec{W}_{L,R}^{\mu}(x) \longrightarrow \epsilon(\mu)\vec{W}_{R,L}^{\mu}(\widehat{x}) \tag{3.14}$$

$$B^{\mu}(x) \longrightarrow \epsilon(\mu)B^{\mu}(\widehat{x}) \tag{3.15}$$

$$\psi_{L,R}(x) \longrightarrow V_{R,L}^{\psi}\gamma^0\psi_{R,L}(\widehat{x}) \tag{3.16}$$

$$\Phi(x) \longrightarrow \Phi^{\dagger}(\widehat{x}) \tag{3.17}$$

using the definitions

$$\widehat{x} := \begin{pmatrix} x^0 \\ -\vec{x} \end{pmatrix} \qquad \text{and} \qquad \epsilon(\mu) = \begin{cases} 1 & \text{for } \mu = 0 \\ -1 & \text{for } \mu = 1, 2, 3. \end{cases} \tag{3.18}$$

To conserve the invariance of the Lagrangian under this parity transformation the same coupling constants to both $SU(2)$ groups and additional constraints involving the arbitrary unitary matrices $V_{L,R}^{\psi}$ are required

$$g_R = g_L, \qquad \left(V_R^{\psi}\right)^{\dagger}\Gamma_{\psi}V_L^{\psi} = \Gamma_{\psi}^{\dagger}, \qquad \left(V_R^{\psi}\right)^{\dagger}\Delta_{\psi}V_L^{\psi} = \Delta_{\psi}^{\dagger}. \tag{3.19}$$

The simplest choice assumes $V_{L,R}^{\psi} = \mathbf{1}$.

Since the Higgs field Φ, which has been introduced to give mass to the fermions, is neither able to break the gauge group of the LRSM (see equation 3.1) to the GSW gauge groups $SU(2)_L \times U(1)_Y$ nor to $U(1)_{em}$, the Higgs sector has to be enlarged for this purpose. Since the Higgs fields, which are required to break down the symmetry, are not unique, there are several interesting realisations [26], which cannot all be discussed in this context. Instead the simplest model, referred to as minimal LR-model, with three scalar multiplets ϕ, Δ_L, Δ_R will be presented [25]. The latter Higgs fields are complex $SU(2)$ triplets with lepton number $L = -2$, which can be written as

$$\Delta = \frac{1}{\sqrt{2}}\sigma_a\delta_a = \begin{pmatrix} \delta_3 & \delta_1 - i\delta_2 \\ \delta_1 + i\delta_2 & -\delta_3 \end{pmatrix}, \tag{3.20}$$

where σ_a denotes the Pauli matrices.

The charge of the Higgs is obtained by

$$Q\Delta = \left[\frac{1}{2}\sigma_3, \Delta\right] + 1 \cdot \Delta = \begin{pmatrix} \Delta_{11} & 2 \cdot \Delta_{12} \\ 0 \cdot \Delta_{21} & \Delta_{22} \end{pmatrix} \tag{3.21}$$

and thus leading to doubly charged as well as single charged and neutral Higgs scalars.

The vacuum expectation values are chosen so that both SU(2) and the U(1)$_{\text{B-L}}$ are broken, but the U(1)$_{em}$ symmetry remains:

$$\langle\phi\rangle_0 = \frac{1}{\sqrt{2}} \begin{pmatrix} v & 0 \\ 0 & w \end{pmatrix}, \qquad \langle\Delta_{\text{L,R}}\rangle = \frac{1}{\sqrt{2}} \begin{pmatrix} 0 & 0 \\ u_{\text{L,R}} & 0 \end{pmatrix}. \tag{3.22}$$

In addition, the assumption of the order of magnitude relations

$$|u_{\text{L}}|^2 \ll |v|^2 + |w|^2 \ll |u_{\text{R}}|^2 \tag{3.23}$$

is motivated by the breaking scheme, which has been established in the SM. The difference in the symmetry of the Higgs potential, reflected by the vacuum expectation values and the symmetry of the Lagrangian, results in the following spontaneous symmetry breaking:

$$SU(2)_{\text{L}} \times SU(2)_{\text{R}} \times U(1)_{\text{L-B}} \times P \stackrel{u_{\text{R}}}{\to} SU(2)_{\text{L}} \times U(1)_{\text{Y}} \stackrel{v,w}{\to} U_{\text{em}}. \tag{3.24}$$

P symbolically denotes the parity symmetry which is broken in the first step.

3.1.3   Experimental consequences and the W'

During the symmetry breaking (3.24) the first stage gives mass to the W_{R} and Z_{R}, which are bosons in the right-handed sector. The properties of the W_{R} are different compared to the Standard Model W and thus, match with the given definition of a W'. At this intermediate stage one obtains the Standard Model with additional Higgs bosons related to Φ and the Δ's. In addition right-handed neutrinos occur, which have to be very heavy (see below). The parity symmetry of the Lagrangian is broken by the Δ-Higgs bosons, whose vacuum expectation value is not parity conserving. Thus, the appealing feature of the LRSM are the recovered parity conservation at energies at the scale of the W_{R}.

The masses of the other boson fields, W_{L} and Z_{L}, result from the subsequent symmetry breaking. This step is in principle equivalent to the Higgs-mechanism in the Standard Model and the arising bosonic fields can therefore be identified with the Standard Model W and Z^0.

The symmetry breaking pattern dictates, that the vacuum expectation value for Δ_{R} is greater than those for Δ_{L} and ϕ. Since the former is related to the W_{R} field and the later to W_{L}, the mass of the W_{R} boson is larger than the W_{L}. Exactly speaking the fields W_{R} and W_{L} do not correspond to physical mass eigenstates $W_{1,2}^{\pm}$ one on one, but are a mixing of both fields:

$$\begin{pmatrix} W_1^{\pm} \\ W_2^{\pm} \end{pmatrix} = \begin{pmatrix} \cos\xi & -\sin\xi\, e^{i\lambda} \\ \sin\xi\, e^{-i\lambda} & \cos\xi \end{pmatrix} \begin{pmatrix} W_{\text{L}}^{\pm} \\ W_{\text{R}}^{\pm} \end{pmatrix}. \tag{3.25}$$

The mixing angle and the (CP-violating) phase can be calculated as a function of the vacuum expectation values

$$e^{i\lambda} = -\frac{vw^*}{|vw|}, \qquad \xi \simeq \frac{2\,|vw|}{|v|^2 + |w|^2} \left(\frac{M_1}{M_2}\right)^2.$$
(3.26)

The masses of the two eigenstates are then given by [22]

$$M_1^2 \simeq \frac{1}{4}g^2(|v|^2 + |w|^2), \qquad M_2^2 \simeq \frac{1}{4}g^2(|v|^2 + |w|^2 + 2\,|u_{\rm R}|^2).$$
(3.27)

The mass of W_1 is the Standard Model mass of the W, whereas the mass of the W_2 is dictated by the breaking scale $u_{\rm R}$ of $SU(2)_{\rm R}$. Since the mass scale has not been observed, $u_{\rm R}$ has to be sufficiently large and thus the mixing can be assumed to be zero as it is done in this work.

Beside the additional vector bosons and numerous Higgs scalars, an important feature of LRSM models is the generation of neutrino masses. Due to the existence of right-handed neutrinos, the neutrinos obtain Majorana masses through the symmetry breaking (see $\mathcal{L}_{\rm Yukawa}$). Through a see-saw mechanism [27, 28] the Standard Model neutrinos obtain small masses, whereas the right-handed neutrinos N obtain masses in the order of the breaking mass scale $u_{\rm R}$

$$m_{\rm N} \sim u_{\rm R} \sim M_2, \qquad m_{\nu_l} \sim m_l^2/m_N.$$
(3.28)

3.2 Other Models with Additional Bosons

As stated before Left-Right-Symmetry can occur in models with larger gauge symmetry groups as intermediate state of a symmetry breaking pattern. Thus, the variety of such models is in principle arbitrary large [29]: they range from $SO(10)$ over Supersymmety to Extra Dimensions. Little Higgs models being in the actual focus of some theorists, are mentioned here as a theory predicting a W' at energies of the LHC.

Little Higgs

Little Higgs models provide a relative new formulation of the physics of electroweak symmetry breaking. The key features of those models are summarized here:

- The Higgs fields are Goldstone bosons, which are associated with some global symmetry breaking at a higher scale.

- The Higgs fields acquire a mass and become pseudo Goldstone bosons via symmetry breaking at the electroweak scale.

- The Higgs fields remain light since they are protected by the global symmetry and free from a 1-loop quadratic sensitivity to the cutoff scale.

The interested reader is referred to dedicated papers (for example see [30]).

Here the motivation of new gauge bosons within these models should be mentioned briefly: In addition to the Standard Model gauge bosons, a set of heavy gauge bosons are

included in Little Higgs models having the same quantum numbers. By the choice of the gauge coupling constants, the Higgs boson quadratic divergences, induced by SM gauge boson loops, are canceled by quadratic divergences of the new heavy gauge bosons.

These new particles are expected to appear at the TeV-scale and should be detected at the LHC. Moreover, the entire reasonable parameter space of Little Higgs models can already be discovered or excluded with one year of LHC data [31].

3.3 The W' Reference Model

Given the large numbers of models which predict new heavy charged gauge bosons, it is a natural approach to use a simplified ansatz for such a search. After a discovery of signatures related to a new boson, detailed studies can be performed to distinguish between these models and to determine whether the boson belongs to a Little Higgs model, a Left-Right-Symmetric or a totally different one. The advantage of such an approach is the independence from other constraints. For example a search for a W' within a LRSM in the decay $W' \to \mu\nu_{\mathrm{R}}$ channel is confronted with the problem of right-handed massive neutrinos. In this case additional assumptions have to be made to get a discovery limit. Following the tradition of direct searches at colliders this study is based on the Reference Model first discussed by G. Altarelli [32].

The Reference Model is obtained by simply introducing ad hoc new heavy gauge bosons, two charged W' vector bosons as well as one neutral Z', as carbon copies of the Standard Model ones. The couplings are chosen to be the same as for the ordinary W and Z^0 bosons. The only parameters are the masses of the new vector bosons. While the coupling of the so constructed bosons with leptons is comparable to those obtained in extended gauge theories, the couplings to the massive Standard Model gauge bosons are enlarged [32]. For W' masses larger than 500 GeV this leads to a W' width larger than its mass. Since such a state is not interpreted as a particle any more, the couplings of W' and Z' to the Standard Model W and Z^0 are suppressed manually in the Reference Model, This results in a moderate width for the new gauge bosons.

This suppression arises in extended gauge theories in a natural manner: if the new gauge bosons and the SM ones belong to different gauge groups, vertices of the kind $Z'Z^0Z^0$ or $W'W^{\pm}Z^0$ are forbidden. They can only occur after symmetry breaking due to mixing of the gauge group eigenstates to mass eigenstates. These vertices are then suppressed by a factor of the order of $(W^{\pm}/W')^2$. With these assumptions the Reference Model has comparable branching ratios (see table 3.2) and thus is a reasonable approach for a direct search.

Additional neutrinos are not taken into account within the model. This work is based on the study of Reference Model W' bosons decaying into a muon and a light non-detectable particle such as the muon neutrino of the Standard Model. The model is implemented in leading order in the event generator PYTHIA and used as starting point for the full detector simulation (see chapter 6).

Branching Ratios						
Model	Reference Model			LRSM ($M_{\nu_R} = 0.5$ TeV)		
$M_{W'}$	1 TeV	2 TeV	5 TeV	1 TeV	2 TeV	5 TeV
$W'^+ \rightarrow \overline{\mathrm{d}}\ \mathrm{u}$	24.2%	24.0%	23.9%	26.7%	24.6%	24.0%
$W'^+ \rightarrow \overline{\mathrm{d}}\ \mathrm{c}$	1.2%	1.2%	1.2%	1.4%	1.3%	1.2%
$W'^+ \rightarrow \overline{\mathrm{d}}\ \mathrm{t}$	0.0%	0.0%	0.0%	0.0%	0.0%	0.0%
$W'^+ \rightarrow \overline{\mathrm{s}}\ \mathrm{u}$	1.2%	1.2%	1.2%	1.4%	1.3%	1.0%
$W'^+ \rightarrow \overline{\mathrm{s}}\ \mathrm{c}$	24.2%	24.0%	23.9%	26.6%	24.5%	24.0%
$W'^+ \rightarrow \overline{\mathrm{s}}\ \mathrm{t}$	0.0%	0.0%	0.0%	0.0%	0.0%	0.0%
$W'^+ \rightarrow \overline{\mathrm{b}}\ \mathrm{u}$	0.0%	0.0%	0.0%	0.0%	0.0%	0.0%
$W'^+ \rightarrow \overline{\mathrm{b}}\ \mathrm{c}$	0.0%	0.0%	0.0%	0.0%	0.0%	0.0%
$W'^+ \rightarrow \overline{\mathrm{b}}\ \mathrm{t}$	24.3%	25.0%	25.1%	26.7%	25.5%	25.1%
$W'^+ \rightarrow \mathrm{l}^+\ \nu_{\mathrm{l}_{(R)}}$	8.2%	8.2%	8.2%	5.7%	7.6%	8.1%

Table 3.2: *Comparison of the branching ratios of the W' in a Left-Right-Symmetric Model and the Reference Model for different masses obtained by* PYTHIA *v6.319. The mass of the massive Majorana neutrino in the LRSM is set to 500 GeV. For W' masses much larger than the Majorana neutrino mass the branching ratios are identical.*

Production of a W' Boson

The production of a W' in a proton-proton collision is comparable to that of a W boson. From constraints of Lorentz-invariance and renormalisability the matrix element for the coupling of a W' to two fermions i and j has the form

$$\mathcal{M} = -\frac{1}{\sqrt{2}}\, i\, g\, W'_\mu \overline{\psi}_i\, \gamma^\mu (a + b\gamma_5)\, \psi_j\, U_{i,j}. \tag{3.29}$$

As mentioned before the coupling constant g is assumed to be identical with the SM one. Therefore also the constants a and b describing the vector- and axialvector-fraction of the interaction are set in coincidence to the SM ($a = 1$, $b = $ -1). $U_{i,j}$ is the Cabibbo-Kobayashi-Maskawa matrix connecting fermions i and j.

The partial width of a W' resulting from the coupling to a quark q_i and an antiquark $\overline{q}_j$ is

$$\Gamma_{i,j} = \frac{N_C\, G_F\, M_W^2\, M_{W'}}{6\sqrt{2}}\, |U_{i,j}| \tag{3.30}$$

with the colour factor N_C and the Fermi coupling constant G_F. Due to the close relation of the W' to the W of the Standard Model the full W' width $\Gamma_{W'}$ (see figure 3.2) can be expressed in terms of the W width Γ_W

$$\Gamma_{W'} \simeq \begin{cases} \frac{M_{W'}}{M_W}\Gamma_W & \text{for } M_{W'} < 180 \text{ GeV} \\ \frac{4}{3}\frac{M_{W'}}{M_W}\Gamma_W & \text{for } M_{W'} \gg 180 \text{ GeV} . \end{cases} \tag{3.31}$$

For W' masses below the top mass ($\sim$ 180 GeV) the kinematically allowed decay channels are identical for the SM W and the W'. For W' masses beyond 180 GeV the decay $W' \rightarrow tb$
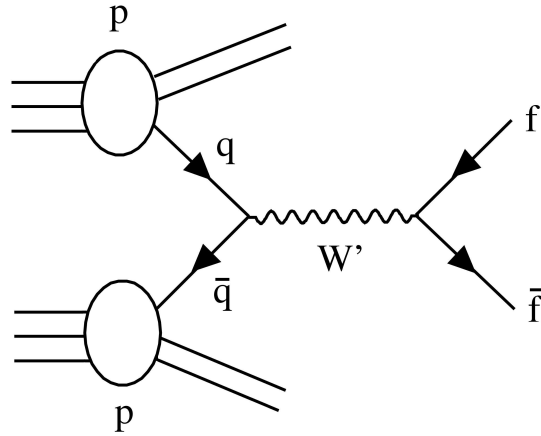
Figure 3.1: *Feynman graph of the W' production in lowest order. A quark-antiquark pair annihilates into a W' and decays into a fermion pair.*

opens. Since the phase space is enlarged it results in an increase of the width[3] by a factor of about $4/3$. In the intermediate region the factor is between 1 and $4/3$ since the decay into a tb-pair is in principle possible, but suppressed because the quark pair has to be produced offshell.

From the tree level Feynman graph (see figure 3.1) the differential production cross section at leading order for a W' can be calculated [32]

$$\frac{d\sigma}{dy}(pp \rightarrow W' + X) = \frac{4\pi^2}{3M_{W'}^3} \sum_{i,j} \int dx_i\, dx_j\, f_i(x_i, M_{W'}^2) f_j(x_j, M_{W'}^2) \Gamma_{i,j} \qquad (3.32)$$

with $f_i(x_i, M_{W'}^2)$ as the probability to find a parton i with a proton's momentum fraction x_i at the energy scale of the W' mass. The according integrated cross section obtained from PYTHIA is plotted in figure 3.2 for the range relevant in this study.

3.4 Previous Searches

The previous searches can be separated in two categories: the first kind uses the generic W' based on Altarelli's Reference Model. The strongest mass limits based on this model are obtained in direct searches at colliders, in particular at the TEVATRON. The second kind of searches assumes a special model, mostly the already presented Left-Right-Symmetric Model. These searches test predictions of the model from which limits on the W' mass can be derived.

3.4.1 Direct Searches

The today's world limit on the W' mass from direct searches is held by the CDF experiment located at the TEVATRON. They used 110 pb^{-1} of data collected in $p\overline{p}$-collisions at a

---

[3]Estimate: due to the small mixing between the quark generations the W can mainly decay to du, sc and $l\nu$. Taking the quark colour into account one obtains $(3 \cdot 2 + 3) = 9$ different decays. A heavy W' has the additional quark-antiquark decay into tb and thus $(3 \cdot 3 + 3) = 12$ possible decays. This results in a rise of the W' width by a factor $12/9 = 4/3$.
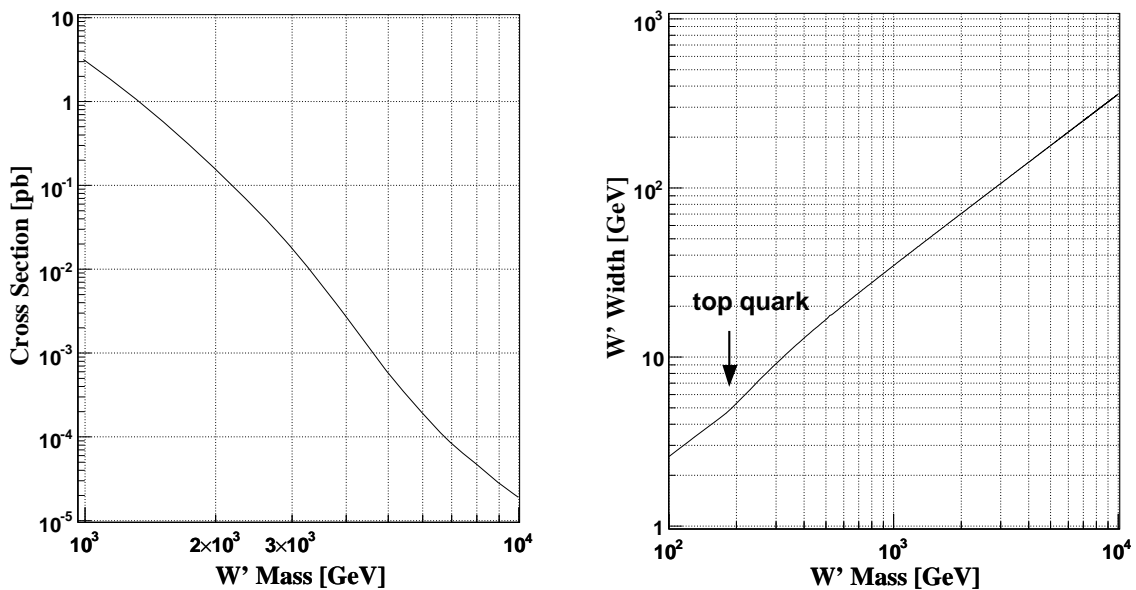
Figure 3.2: *The cross section (left) and the width of the W' as a function of its mass obtained by* PYTHIA *v6.319. The small kink in the width at around 200 GeV results in the additional decay channel of the W' into a top and bottom quark, which is kinematically not allowed for the SM W.*

centre of mass energy $\sqrt{s} = 1.8$ TeV during 1992–95. A lower mass bound is set by the determination of a limit on the ratio of the branching fractions

$$\frac{\sigma(W' \to e\nu)}{\sigma(W \to e\nu)}.$$

Since the cross section of the W' is mass dependent, a mass limit can be obtained. Knowing the SM expectations for the number of $e\nu$-events in different transverse invariant mass bins, the maximal number of W' events $N_{W'}^{95}$ compatible with the measurement at 95% confidence level has been determined using Poisson probability. An upper limit on the branching ratio is given by

$$\left(\frac{\sigma(W' \to e\nu)}{\sigma(W \to e\nu)}\right)_{95} = \frac{N_{W'}^{95} A_{\mathrm{W}}}{A_{W'} N_{\mathrm{W}}}$$

taken the detector acceptances A_{W}, $A_{W'}$ for W and W', respectively, into account. Comparing this ratio as a function of the W' mass with the expected ratio obtained by the W' Reference Model implemented in PYTHIA results in a lower mass limit of 754 GeV. Combining this limit with the CDF $W' \to \mu\nu$ channel limit, calculated in the same manner, lifts the bound to 786 GeV [33].

Recent studies within the DØ experiment give rise to a lower bound of 965 GeV [34].

3.4.2 Indirect Searches

Because of the variety of indirect searches, which make different assumptions about the coupling of the new gauge bosons, the Higgs sector and the (right-handed) neutrino sector, only some ideas for experiments resulting in W' mass limits are given (for an review see [35]).

- K_{L}-K_{S}-mass difference:

  The K_{L}-K_{S}-mass difference can receive important contributions from box diagrams including the exchange of new heavy charged gauge bosons like the one shown in figure 3.3. Since the mass difference of the K_{L}-K_{S}-system is known from experiments to be $\Delta m = m_{\mathrm{K_L}} - m_{\mathrm{K_S}} = (3.483 \pm 0.006) \cdot 10^{-12}$ MeV [36] a mass limit of the order of $M_{W_{\mathrm{R}}} > 1.6$ TeV can be derived depending on the assumed couplings [37].

- **Neutrinoless Double β-Decay:**

  The existence of a new heavy (right-handed) gauge boson coupling to massive Majorana neutrinos gives rise to additional Feynman graphs for the neutrinoless β-decay. The most important contribution arises from the graph shown in figure 3.3. Two neutrons both decay into a right-handed W'. If one W' decays into a lepton and a Majorana neutrino, the other W' can absorb it, since the (heavy right-handed Majorana) neutrino is its own antiparticle, and can create a lepton. Up to now there have not been any observations of this kind of neutrinoless β-decay. From the upper bound on the cross section a limit on the W' mass of 310 GeV can be derived [38].

Further constraints on the W' mass have been derived from cosmological considerations concerning supernovae, electro-weak fits to data from neutrino-hadron, neutrino-electron and electron-hadron interactions, neutron and muon decay and further more (see [36]).
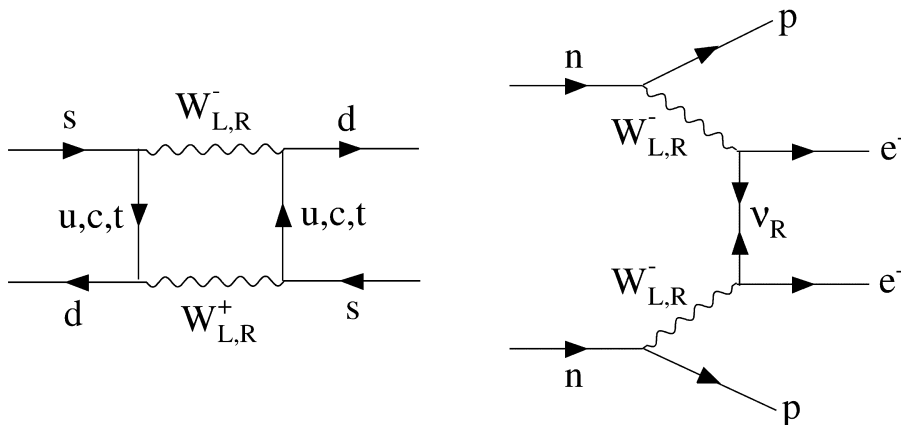
Figure 3.3: *Additional Feynman graphs arising in case of an existing W' in $K_{\mathrm{L}} - K_{\mathrm{S}}$-oscillations and neutrinoless double β-decay.*

Chapter 4

The CMS Detector at the LHC

Today's world largest particle physics laboratory, CERN, situated on the border between France and Switzerland, was founded on september 29, 1954. From the original twelve signatories of the CERN convention the membership has grown to 20 members.

Since its foundation CERN made the way to breakthroughs in the understanding of fundamental particles and their interactions: the discovery of neutral currents in 1973, the discovery of the W and Z bosons in 1983, the high precision measurements of weak interactions at the LEP experiments and lately the exploration of a new state of matter (possibly the quark-gluon-plasma) are just some of the historical highlights. Beside the importance of CERN in the physics community it is also known for its social and cultural relevance.

Figure 4.1: *The Large Hadron Collider at CERN with its four experiments ALICE, ATLAS, CMS and LHCb.*

4.1 The Large Hadron Collider

From 2007 onwards CERN will host the most powerful collider in the world: the Large Hadron Collider (LHC). Aiming for a deeper knowledge of the fundamental constituents of matter and their interactions protons and also heavy ions will be collided. This section discusses the properties of the LHC machine, designed to provide physicists with a general tool to explore the TeV-energy scale.

4.1.1 Physics at proton-proton colliders

The energy loss per revolution of a particle with mass m and energy E due to synchrotron radiation in a circular collider with radius R, is proportional to $E^4/(m^4 R)$. This determines the LEP collider to be the last electron-positron collider of these dimensions.

The use of protons with a 2000 times higher mass avoids the problem of huge radiative energy loss, but with the drawback of not colliding elementary particles. Instead of point-like particles the constituents of protons, namely quarks and gluons, interact with only a fraction of the proton energy[1]

$$\sqrt{s'} = \sqrt{x_a x_b s}. \tag{4.1}$$

x_a and x_b refer to the energy-fractions carried by the interacting partons, respectively, whereas $\sqrt{s'}$ is the centre of mass energy of the colliding partons and $\sqrt{s}$ the centre of mass energy of the protons. Thus, the centre of mass energy has to be larger compared to an electron-electron machine.

For the discovery of new particles it is not sufficient to achieve a high amount of energy, but it is also necessary to produce collisions with a significant rate. The number of events N_{event} for a special process with a cross section σ_{event} at a collider luminosity $\mathcal{L}$ is given by

$$N_{\text{event}} = \mathcal{L}\,\sigma_{\text{event}}. \tag{4.2}$$

Assuming a Gaussian beam distribution with widths σ_x and σ_y in x- and y-direction, respectively, the luminosity is approximately given by

$$\mathcal{L} = \frac{n_b\,N_b^2\,f}{4\pi\sigma_x\sigma_y}. \tag{4.3}$$

N_b yields the number of particles per bunch, n_b the number of bunches per beam and f the revolution frequency. All these parameters have to be tuned in order to achieve the highest possible luminosity and thus the best capability for new discoveries.

The cross section of a special partonic process (like $q\bar{q} \to W' \to \mu\nu$) depends on the cross section $\hat{\sigma}$ of the proton partons (partonic cross section), graphically modeled by Feynman graphs. Since only two partons interact directly within a pp-collision the cross section is also dependent on the partons densities (given as parton density functions, pdf) inside the proton,

$$\sigma = \int dx_1 \int dx_2\; f_1(x_1, Q^2) f_2(x_2, Q^2)\,\hat{\sigma}. \tag{4.4}$$

---

[1] As a rough estimate: $\sqrt{s'} \approx 1/6\sqrt{s}$. The factor $1/6$ results from 3 sea quarks within each proton carrying half of the proton's momentum.

The pdf $f_i(x_i, Q^2)$ equals the probability to find a parton inside the proton carrying the momentum fraction x_i at the energy scale Q.

In hard scatterings the interaction energy and thus the rest frame is not known, because the proton remnants, which carry a sizable fraction of the protons' energy, escape undetected at small angles mainly through the beam pipe. Thus, only energy and momentum conservation in the transverse plane can be used to find non-interacting particles such as neutrinos.

Since the LHC is aiming for rare events the luminosity and thus the number of particles per bunch are chosen as large as possible. This has the drawback of having several interactions in one beam crossing. For the high luminosity phase ($\mathcal{L} = 10^{34}$ cm^{-2} s^{-1}) of the LHC there are up to 20 interactions at once, mainly QCD events (so called minimum bias). For the detectors this results in an extreme challenge to identify interesting physics processes out of the enormous amount of collisions.

The proton with its quark-gluon substructure enlarges the challenge. Since most of events are created by two interacting partons colour charged fractions of the two protons leave the interaction point and produce additional jets. Since these particles carry small transverse momenta they vanish mainly through the beam pipe (beam remnants).

In figure 4.2 the cross section and the event rate at the LHC design luminosity for various processes as a function of the centre of mass energy $\sqrt{s}$ is given. A remarkable aspect of the LHC physics is the wide cross section range of processes under investigation. While the total cross section is dominated by QCD events like $qq \rightarrow qq$, $qq \rightarrow gg$ or $qg \rightarrow qg$, rare events like the production of new gauge bosons like Z' or W' are investigated with expected cross sections, which are smaller by a factor 10^{10}. The multiplicity of QCD events makes it difficult to detect a signal in final states containing only jets. Due to its lower background leptonic and semi-leptonic physics processes are preferred and thus the identification and measurement of leptons especially in the high p_{T}-range is a crucial task for the LHC experiments.

4.1.2   The LHC design

With a centre of mass energy of 14 TeV and a design luminosity of $\mathcal{L} = 10^{34}$ cm^{-2} s^{-1} 2808 bunches of $1.15 \cdot 10^{11}$ protons each will be accelerated in the 27 km long former LEP[2] tunnel about 100 m below surface and will collide every 25 ns at four interaction points where the experiments ALICE[3], ATLAS[4], CMS[5] (plus TOTEM[6]) and LHCb[7] are located. The two multi-purpose detectors ATLAS and CMS aim at rare events with highest luminosities ($\mathcal{L} = 10^{34}$ cm^{-2} s^{-1}), whereas the low luminosity experiments LHCb ($\mathcal{L} = 10^{32}$ cm^{-2} s^{-1}) and TOTEM ($\mathcal{L} = 2 \cdot 10^{29}$ cm^{-2} s^{-1}) are investigating B-physics and protons from elastic scattering at small angles, respectively. Due to the general layout of the accelerator the LHC can also be operated with heavy ion beams. In addition to the ATLAS and CMS

---

[2]**L**arge **E**lectron **P**ositron Collider
[3]**A** **L**arge **I**on **C**ollider **E**xperiment
[4]**A** **T**oroidal **LHC** **A**pparatu**S**
[5]**C**ompact **M**uon **S**olenoid
[6]**TOT**al and **E**lastic **M**easurement
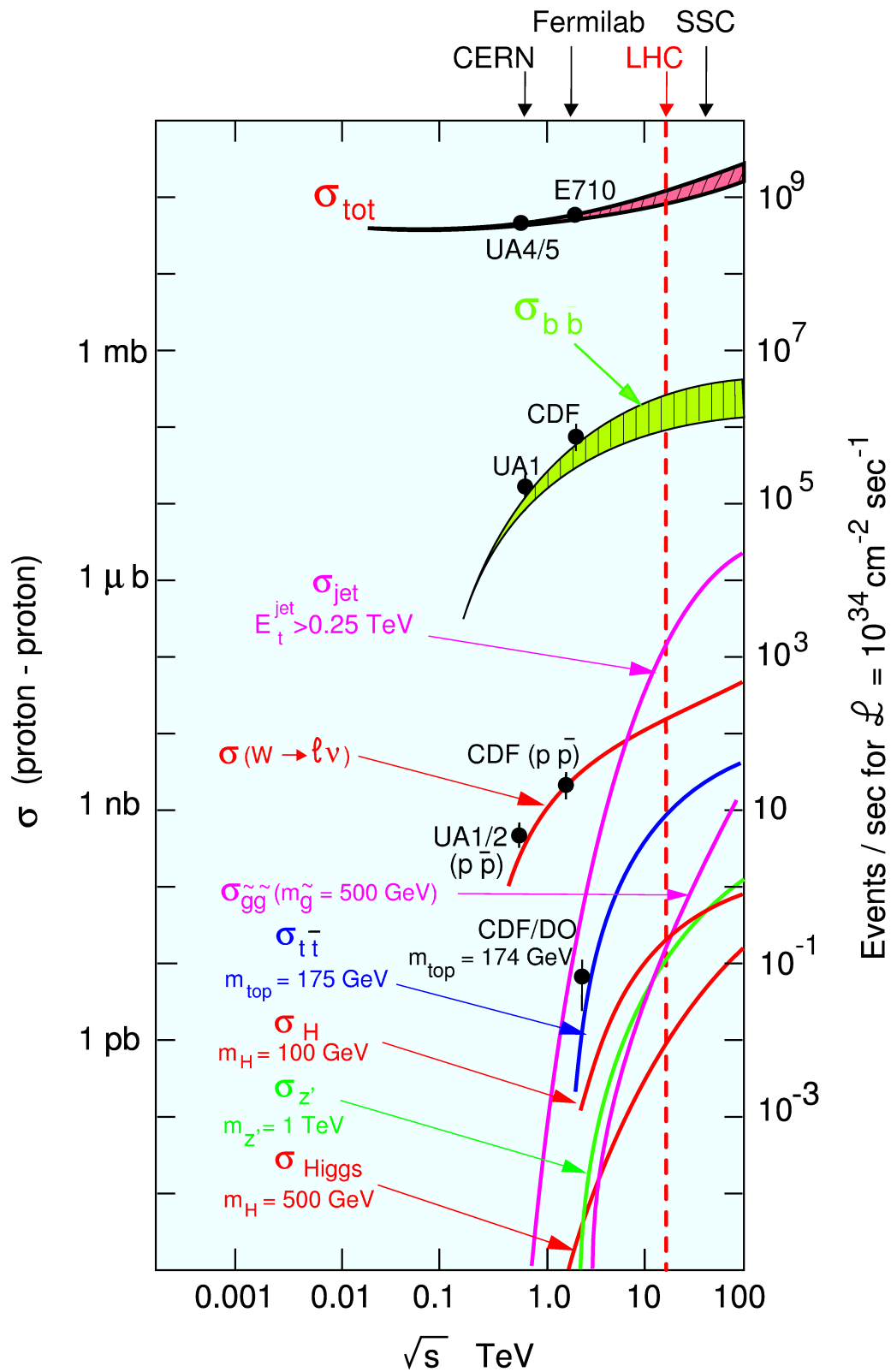[7]The **L**arge **H**adron **C**ollider beauty experiment

Figure 4.2: *Cross sections and event rates for different processes as a function of the centre of mass energy at proton-proton colliders [39].*

experiments the LHC has one dedicated heavy ion experiment ALICE aiming at a peak luminosity of $\mathcal{L} = 10^{27}\,\text{cm}^{-2}\,\text{s}^{-1}$ for Pb-Pb collisions.

Parameter	Value	Unit
Momentum at collision	7	TeV
Dipole field at 7 TeV	8.33	T
Quadrupole gradient	220	T/m
Circumference	26659	m
Design Luminosity	10^{34}	$\text{cm}^{-2}\,\text{s}^{-1}$
Number of bunches	2808	
Particles per bunch	$1.1 \cdot 10^{11}$	
DC beam current	0.56	A
Stored energy per beam	362	MJ
Ultimate Dipole Field	9	T
Injection Dipole Field	0.4	T
Ramp Time	20	min
Magnet Coil inner diameter	56	mm
Distance between beams	194	mm

Table 4.1: *LHC design parameters [40].*

The LHC is designed as a superconducting collider accelerating two beams of equally charged particles with separate magnet dipole fields and vacuum chambers in the main arcs. The beams share common sections only at the four interaction points and at the insertion region. To allow an operating magnetic field of 8.4 T the 1232 dipole magnets are cooled with superfluid helium to a temperature of 1.9 K. A highly sophisticated system of magnets is used to focus the beam and thus to guarantee a continuous operation.

The high centre of mass energy of 14 TeV can only be achieved by accelerating the bunches of particles stepwise using several already existing CERN pre-accelerator facilities. The upgraded Linac 2 will deliver protons of 50 MeV energy with an intensity of 180 mA and pulses of about 20 μs to the PS (Proton Synchrotron). The modified PS with its two new radiofrequency systems (RF), will feed the SPS (Super Proton Synchrotron) with bunches of 25 ns spacing and an energy of 26 GeV.

The SPS itself, upgraded with a new superconducting RF system, will accelerate the protons to an energy of 450 GeV and fill finally the LHC. One full injection of the LHC requires twelve cycles of the SPS synchrotron and each SPS fill requires three or four cycles of the PS synchrotron. Counting 21.6 s for every SPS and 3.6 s for every PS cycle with some additional injection and machine adjustment cycles the minimum LHC injection time is 16 minutes. Further 20 minutes are needed for ramping the 2808 proton bunches in the LHC from 450 GeV to 7 TeV. Thus after a total time of about 40 minutes LHC is ready for collisions at the highest centre of mass energies.

Due to interactions of the beams with their environment the luminosity lifetime is expected to be about 15 h; the anticipated time of data taking is around 6 to 12 hours per fill due to the luminosity decrease from collisions. With these parameters the maximum total

integrated luminosity per year is expected to be between 80 fb^{-1} and 120 fb^{-1} depending on the average operational time of the machine.

In 2007 the LHC will operate for a few weeks at a luminosity up to $\mathcal{L} = 10^{32}$ cm^{-2} s^{-1} colliding 43 on 43 proton bunches. For 2008 the collider is planned to be driven for 100 days at pp-luminosities close to $\mathcal{L} = 2 \cdot 10^{33}$ cm^{-2} s^{-1} with initially 75 ns and later 25 ns bunch spacing. For the following years the LHC tends towards the design luminosity of $\mathcal{L} = 10^{34}$ cm^{-2} s^{-1} with colliding bunches every 25 ns.

4.2   The CMS Detector

CMS is a general-purpose detector which is built from various sub-components to measure the particles which are directly or indirectly created within a pp-collision. According to the energy loss of the decay products in matter the subdetectors with their different tasks are placed shell-like around the interaction point. Elements close to the beam line are built with as little material as possible to suppress multiple scattering and absorption of particles before their identification in the dedicated detector parts.

A first proposal of the CMS detector has been presented during the LHC workshop [41], which took place in Aachen in 1990. The proposal is based on a solenoid magnet with a highly performant muon system and a compact design.

Since then much effort has been spent on the research and development of the whole detector. Today's design as shown in figure 4.3 consists of a 4 Tesla solenoidal superconducting magnet, 13 m long with an inner diameter of 5.9 m. The view of the detector is dominated by the iron return yoke surrounding the magnet with five so called wheels and two endcaps made of three discs each. In total CMS has a length of 21 m and an outer diameter of 15 m resulting in a weight of around 12500 t.

For an experiment hosted at a pp-collider it is natural to optimise the muon system in first place: among the leptons, muons can be separated easily from other particles and their measurement up to the TeV-energy region is not complicated by bremsstrahlung as in the case of electrons. The design goal of a very good and redundant muon system is realized by three different technologies, a strong uniform magnetic field of 4 Tesla and a nearly hermetic solid angle coverage up to $|\eta| = 2.4$.

Inside the magnet coil the electromagnetic and hadronic calorimeter as well as the main tracker are placed. This has the advantage that the calorimeter performance is not affected by the coil and a high intrinsic resolution is guaranteed. The strong magnetic field reduces the arrival of soft charged hadrons and other low energetic particles in the calorimeter and guarantees a highly performant electromagnetic calorimeter.

In addition, the bending of charged tracks improves the momentum resolution inside the tracker. A high quality central tracker with robust track and detailed vertex reconstruction is built to support the muon system and the calorimeter. The CMS detector is equipped with an all silicon inner tracker to achieve a good spatial resolution for tracks within an environment of high particle fluxes. Due to the high track multiplicities expected at the enormous luminosity and a bunch crossing rate of 40 MHz this is an important task. A pixel vertex detector is mounted close to the beam pipe to detect secondary vertices arising for example from B-mesons and τ-leptons.
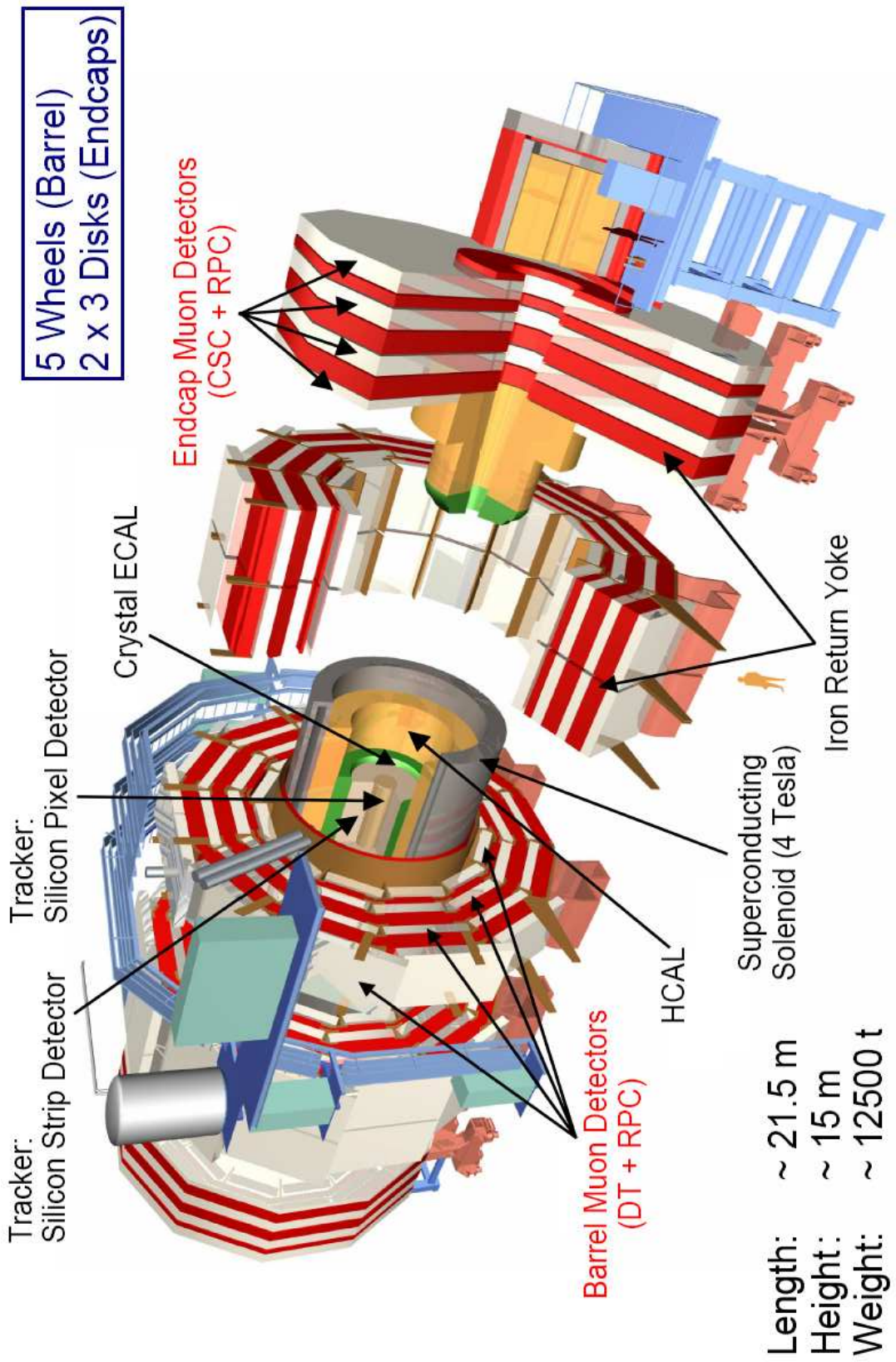
Figure 4.3: *The Compact Muon Solenoid [42].*

In the following sections the CMS detector is briefly described, starting from the innermost part and following a particle track to the outermost instruments. Details can be found in [2, 39, 43–47].

4.2.1 The Silicon Pixel Detector

Several interesting events at the LHC are likely to contain secondary vertices, e.g. from b- or c-quarks or from τ-leptons. These particles are created at the pp-collision point, but travel a few millimeters before they decay at a secondary vertex. To allow for an efficient observation of these decays a high-resolution pixel detector is mounted as close as possible to the interaction point. Due to the close neighbourhood to the beam the detector is exposed to high particle fluxes resulting in a limited lifetime for this detector component. The pixel detector is expected to provide space point information with a high
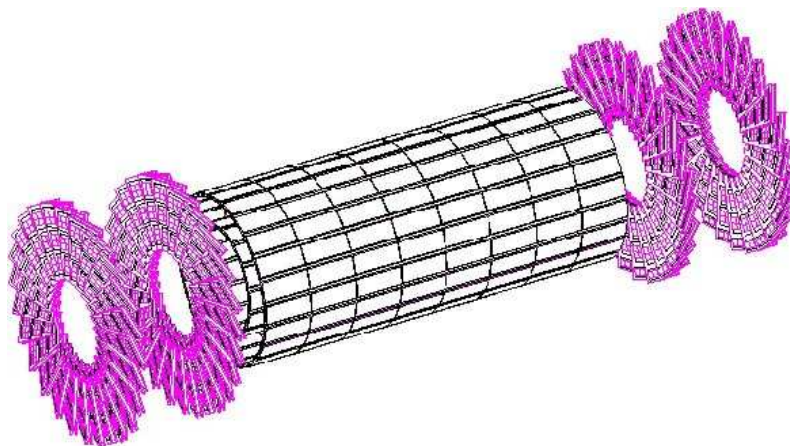
Figure 4.4: *The CMS pixel detector is centred around the beam pipe and represents the innermost layer of the CMS tracking system [43] (see also figure 4.5)*

resolution and a minimum of two pixel hits per track to improve the ability to distinguish secondary vertices originating from long-lived objects against jets arising from light quarks and gluons. Therefore the CMS pixel system (see figure 4.4) consists of two barrel layers and two pairs of forward and backward end discs. For the low luminosity configuration the inner barrel layers reside 41–45 mm and 70–74 mm away from the nominal beam axis. When reasonable operation of the innermost layer is no longer provided, it will be removed and a new layer will be installed at 107–112 mm.

The endcap discs with a radius from 60–150 mm are placed at ± 32.5 cm and ± 46.5 cm in z-direction. They complete the η-coverage for at least two pixel hits up to $|\eta| = 2.4$ for tracks originating from the centre of the interaction region. The radiation environment close to the interaction region will cause damage to the pixel sensors and readout chips and hence limit their lifetime. However, a silicon detector is a good compromise between radiation hardness, cost, occupancy and achievable space point resolution. With a pixel size of 150 μm $\times$ 150 μm one obtains a hit resolution of about 10 μm in the rϕ-plane and 17 μm in the rz-plane, under the assumption of an overall alignment precision within 10 μm.

The readout is performed analog to profit from effects of charge sharing among the pixels due to the 4 T magnetic field. Using charge interpolation among several pixels a higher hit resolution is obtained. To minimize the effect of radiation damages within the silicon the approximately 39 million pixels are operated at a temperature of -10°C.

Finally the pixel detector allows fast and efficient track seed generation from which the track reconstruction can start, extrapolating the particles into the silicon strip detector and further on.

4.2.2 The Silicon Strip Tracker
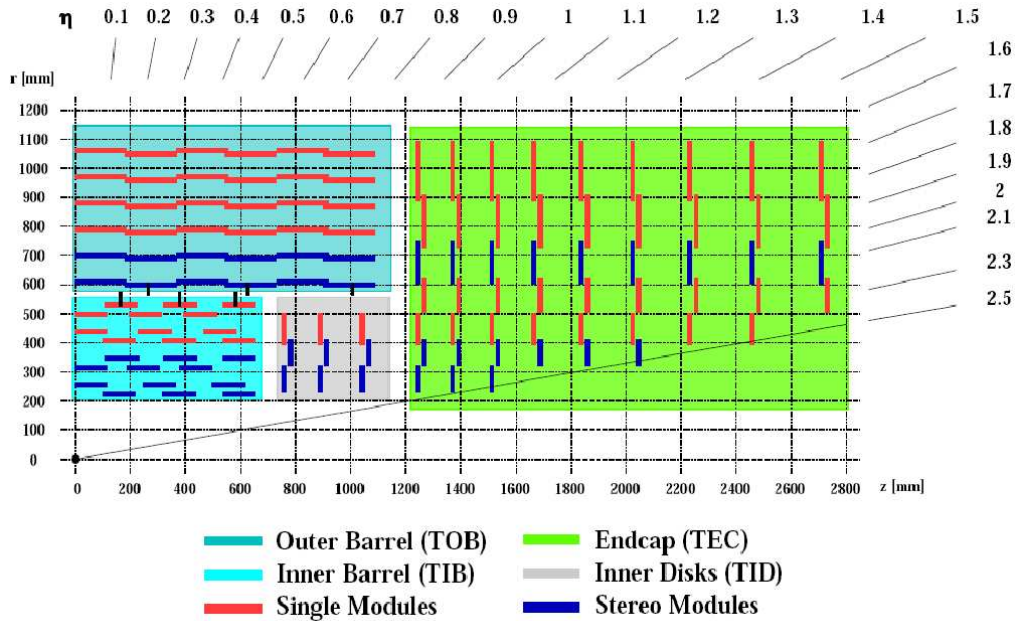
Figure 4.5: *Cross section of one quarter of the CMS silicon tracker [43].*

In the challenging environment of the LHC the detection of high-p_T leptons plays an essential role in the separation of signal from background. Therefore the task of the tracker is a precise measurement of the transverse momentum up to the TeV-regime. This is achieved by a high point resolution of the tracks bended in the magnetic field and a large number of measurements along the track. In conjunction with the pixel detector the tracker improves the impact parameter resolution with a sophisticated pattern recognition.

The silicon strip tracker (see figure 4.5) covers a cylindrical volume with a length of about 5.4 m and a radius between 0.2 and 1.2 m. An active area of approximately 210 m^2 is divided into ten barrel layers and nine discs in each outer endcap plus three mini-discs arranged as shown in figure 4.5 and 4.6.

The high rate of underlying events in one collision and a bunch crossing every 25 ns results in a very high charged particle flux in the tracker. Due to the strong magnetic field charged particles with less than a few GeV transverse momentum cannot leave the tracker and spiral until they are absorbed. At a radius of 25 cm still 0.1 charged particles incident per 1 cm^2 every 25 ns. Thus the tracking system requires a high granularity to separate
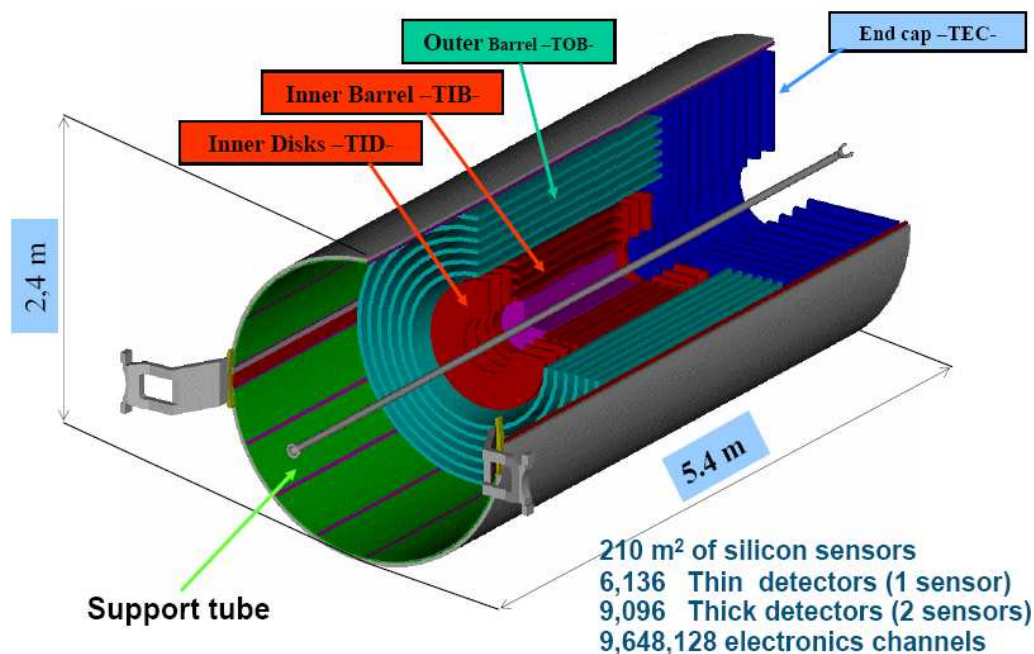
Figure 4.6: *The CMS full silicon inner tracking system. It consists of an outer and inner barrel, two endcaps and two inner discs. In addition the pixel detector is visible in the centre. The overall construction resides inside a support tube [43].*

close tracks. It must be radiation hard, but should consist of as little material as possible e.g. to reduce conversion of photons before reaching the calorimeter.

The tracker covers an $|\eta|$-range smaller 2.5, in which electrons and muons are reconstructed with an efficiency larger than 98%, a fake track rate below 1%, and an expected momentum resolution, which is approximately given by [48]

$$\frac{\Delta p_{\mathrm{T}}}{p_{\mathrm{T}}} = 0.15\, p_{\mathrm{T}}\,[\text{ TeV}] \oplus 0.5\% \qquad (4.5)$$

for isolated charged leptons. As shown by detector simulations a good determination of the track parameters with only 4–6 hits allows fast and clean pattern recognition. The whole tracker has to be kept at -10°C to ensure that the silicon survives the high radiation environment of the LHC.

4.2.3 The Electromagnetic Calorimeter

The electromagnetic calorimeter (ECAL) [2] measures the energy and the direction of electromagnetically interacting particles like electrons, photons or parts of the electromagnetic fraction of jets with high precision by absorbing these particles inside scintillating crystals. To meet the LHC requirements of radiation hardness and to achieve a high energy resolution, $PbWO_4$, with its high density and therefore short radiation length[8] X_0 and

---

[8]The energy of a high-energetic electron ($E \gg 1$ MeV) has dropped to 1/e - on average - after passing the distance of one radiation length X_0.
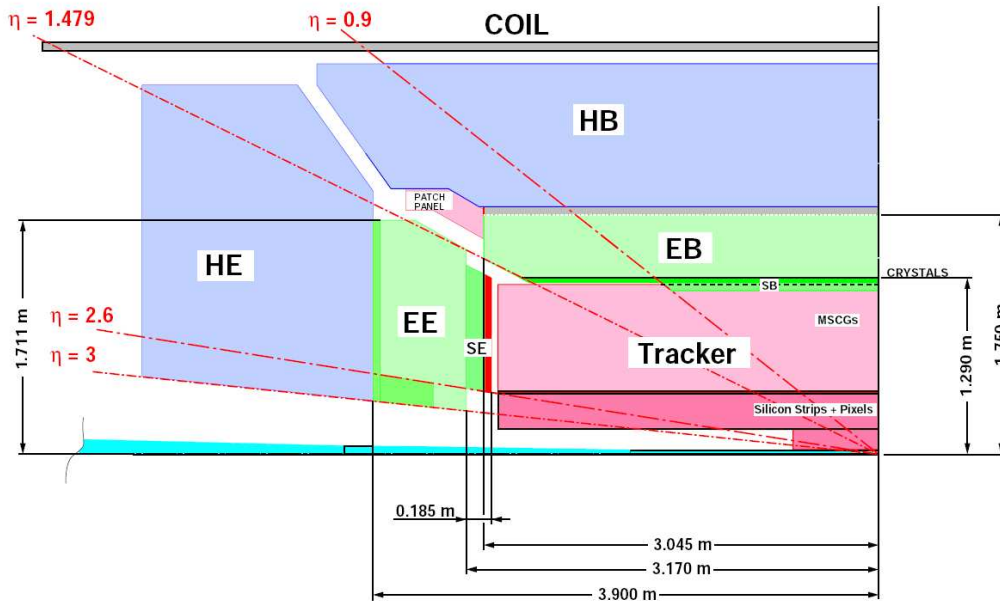
Figure 4.7: *One quadrant of the CMS calorimeters [2]. The tracker is surrounded by the barrel electromagnetic (EB) and hadronic barrel calorimeter (HB). In the direction of the beam line the calorimeter is completed by the electromagnetic (EE) and hadronic endcap calorimeter (HE) .*

small Moliere radius[9] of 22 mm has been chosen. It allows a very compact electromagnetic calorimeter which fits into the design of CMS.

Special efforts have been made for the development of crystals, photodetectors, electronics and software to meet the challenging LHC requirements of an average of 1000 charged tracks penetrating the ECAL every 25 ns. The readout is done by special avalanche photodiodes in the barrel and vacuum photo triodes in the endcaps, which are both insensitive to high magnetic fields. They amplify the light gained from the crystals and measure the energy deposit.

Because of the strong temperature dependence of the crystal light yield and of the diode gains, the temperature inside the calorimeter has to be kept constant within 0.1 K to guarantee a precise operation of the ECAL [2].

The ECAL is built of a cylindrical barrel with a length of around 6 m, an inner radius of 1.3 m and an outer radius of 1.8 m. Endcaps are located in forward and backward direction at ±3.2 m with an extension of 0.7 m along the z-direction. With these dimensions the crystals hermetically cover an $|\eta|$-range up to 3.0. The precision of the energy measurement for electrons and photons is limited by the radiation dose, the amount of pileup energy deposited and the tracker coverage up to $|\eta| = 2.5$. The shape of the approximately 60000 barrel and 20000 endcap crystals is chosen so that their front face (22 x 22 mm^2) points to the interaction region (pseudo-projective geometry). This corresponds to a granularity of $\Delta\eta \times \Delta\phi = 0.0175 \times 0.0175$ in the ECAL barrel which grows progressively with η to a maximum of $\Delta\eta \times \Delta\phi \approx 0.05 \times 0.05$. The typical crystal depth of 230 mm is identical to

---

[9]In a cylinder with a radius of a Moliere radius on average 95% of the electromagnetic shower energy is contained.

26 radiation lengths X_0. For trigger purposes arrays of 5×5 crystals are grouped to one ECAL trigger tower which coincide with the HCAL tower granularity.

The neutral pion and photon separation is improved by an endcap preshower detector installed in front of each ECAL endcap [49]. It consists of a lead absorber to initiate photon showers and covers a range from $1.65 < |\eta| < 2.61$. Its thickness of 2.8 X_0 is well adapted to guarantee a 95% conversion probability and to prevent a degradation of the excellent crystal calorimeter energy resolution. The readout is performed by silicon sensors which act as energy sampling devices. The Preshower detector improves the π^0/γ but also the $e^\pm/\pi^\pm$ separation and enhances the spatial resolution of the calorimeter.

The energy resolution of a calorimeter can be described by the following formula

$$\frac{\sigma(E)}{E} = \frac{a}{\sqrt{E[\text{GeV}]}} \oplus \frac{b}{E[\text{GeV}]} \oplus c \tag{4.6}$$

using the notation $g \oplus h := \sqrt{g^2 + h^2}$. The term a, called stochastic term, reflects the shower fluctuations, the photon-statistics and the fluctuation of the transverse leakage of the produced shower in the calorimeter. The design value of a was defined to be 2.7% and 5.7% for the barrel and the endcap calorimeter, respectively. The so called noise term b comprises the electronic noise including dark currents and pileup of overlapping events. The noise term corresponding to a cluster of 5×5 crystals is expected to be about 150 MeV (210 MeV) for the barrel and 205 MeV (245 MeV) for the endcaps at low (high) luminosity. The constant term c of about 0.55% results from intercalibration errors, crystal non-uniformity and shower leakage.

4.2.4   The Hadronic Calorimeter

The CMS detector is equipped with four kinds of hadronic calorimeters [44], featuring a good segmentation, moderate energy resolution and full angular coverage up to $|\eta| = 5$. As displayed in figure 4.7 the barrel hadronic calorimeter (HB) is inserted into the magnet coil and surrounds the electromagnetic calorimeter up to a pseudorapidity of $|\eta| = 1.3$. It is completed by two endcap hadron calorimeters (HE), $|\eta| \leq 3$, also located inside the solenoid and extended by the two (very) forward calorimeters (HF), surrounding the beam pipe $11\,\text{m}$ away from the interaction point. In addition the central shower containment is improved with an array of scintillators located outside the magnet labeled as outer hadronic calorimeter (HO).

The HCAL measures the hadronic component of jets and other hadronic particles. Due to the hermetic layout of both, the electromagnetic and hadronic calorimeters, the transverse component of the energy imbalance can be calculated, and neutrinos or other particles not interacting inside the detector, can be seen indirectly.

Hadronic Calorimeter: Barrel and Endcaps

For the HB and HE placed inside the magnet the collaboration decided to use a sampling calorimeter made of brass and plastic scintillators, which are read out by wavelength-shifting plastic fibres. The HB is divided into two cylindrical sections, which are segmented

into 18 identical wedges. Each wedge, aligned parallel to the beam axis, consists of alternating 17 layers of 5–8 cm brass and readout scintillators divided into segments of the size $\Delta\eta \times \Delta\phi = 0.087 \times 0.087$. It is sandwiched by stainless steel for structural strength.

The HE consists of 18 20°-modules, each made of 19 layers of brass and scintillator with the same transverse segmentation as the HB to match the trigger tower granularity of the ECAL. While the HB has a minimum depth of 5.8 nuclear interaction lengths[10] λ_I, the HE consists of at least 10 interaction lengths λ_I.

The Forward Calorimeters

The HF calorimeters (1.65 m length, 1.4 m radius) are made of steel absorbers and embedded radiation hard quartz fibres, which provide a fast collection of Cherenkov radiation by photomultipliers. With a depth of roughly 9 λ_I it is a crucial tool to improve missing energy detection and also useful to tag forward jets to reduce backgrounds in signal reactions without associated jet production in forward direction.

Charged particles entering the HF produce particle showers in which only electrons and positrons are fast enough to produce Cherenkov light. Thus the calorimeter is mainly sensitive to the electromagnetic component of showers, providing a very clean and fast signal. In addition it is used for luminosity monitoring.

Outer Hadronic Calorimeter

In the barrel region a particle has to pass about 8 nuclear interaction lengths until it reaches the magnet. That means, that for a 300 GeV pion 5% of the energy would be deposited beyond the outer limits of the HB. To improve the shower containment two layers of scintillators are located outside the solenoid but in front the first muon station. This extends the total depth of the HB to 11.8 λ_I with an improvement in linearity and resolution.

The overall resolution of the complete calorimeter system including both, electromagnetic and hadronic, calorimeter is given by [44]

$$\frac{\Delta E}{E} = \frac{100\%}{\sqrt{E[\text{GeV}]}} \oplus 4.5\% \tag{4.7}$$

for energies between 30 GeV and 1 TeV.

4.2.5 The Superconducting Solenoid

The CMS detector is equipped with a superconducting solenoid [45] bending the tracks of the charged particles and thus allow to measure their transverse momentum. The superconducting coil with a length of 13 m and a diameter of about 5.9 m is located inside the barrel wheels, which constitute the return yoke (see figure 4.3). The magnet is cooled with liquid helium. As shown in figure 4.8 the magnetic field reaches up to 4 T and is especially in the endcaps quite inhomogeneous. Fully operational the magnet stores an energy of 2.7 GJ.

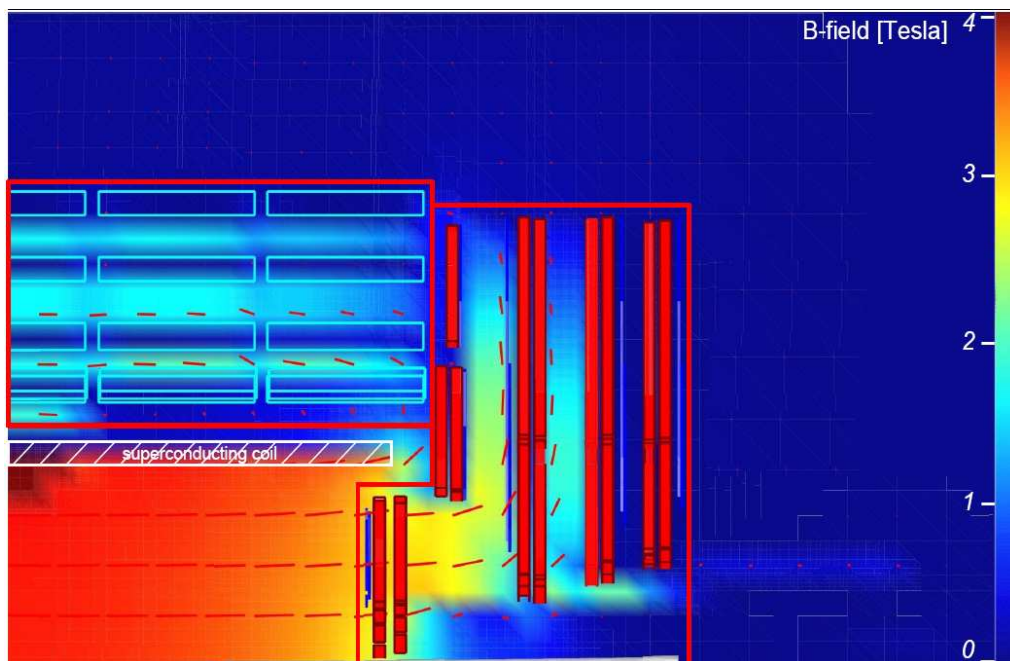[10]On average a hadronic interaction occurs at one nuclear interaction length λ_I.

Figure 4.8: *The magnetic field within one quarter of the CMS detector. Picture generated using* IGUANACMS *[50].*

4.2.6 The Muon System

As implied by the name of the detector, CMS is specially focused on triggering and reconstruction of muons, which give clear signatures for a variety of physics processes, like the "golden channel" for Standard Model Higgs searches $H \rightarrow ZZ \rightarrow 4\mu$ or the decay of new heavy gauge bosons $Z' \rightarrow \mu\mu$ and $W' \rightarrow \mu\nu_\mu$. In the muon system the momentum as well as the charge of muons is determined by measuring the track bending due to the magnetic field with three different types of gaseous detectors.

The choice of the detector technology is driven by the very large surface to be covered, the precision needed and the different background radiation environments. Beside the crucial features of muon identification and bunch crossing assignment, the p_T measurement especially for high momentum muons is given by the muon system. It has a spatial resolution of the order of 100 μm. Due to the multiple scattering of the muons in the iron of the return joke the overall p_T resolution for low momentum muons ($p_\mathrm{T} < 200$ GeV) is determined by the tracker.

The muon system, which is embedded in the iron return yoke of the magnet, consists of four stations, arranged as concentric cylinders around the beam pipe in the barrel region and as discs perpendicular to the beam line in the endcaps. The 10 interaction lengths before the first muon station and another 10 from the iron yoke before the last station, guarantee that no other particles than muons (with an energy of more than 5 GeV) and neutrinos pass the muon system and ensure the muon identification to be above 95%.

Three different technologies are employed in the hermetic muon system: in the barrel drift tubes (DT) are installed, where the occupancy, the background noise and the residual magnetic field are relatively low compared to the endcaps where cathode strip chambers (CSC) are used. In addition, resistive plate chambers (RPC) provide in both regions an

independent measurement for trigger purposes with a superior time, but a lower spatial resolution. The muon system covers regions up to $|\eta| = 1.2$ for DTs, $|\eta| = 2.4$ for CSCs and RPCs.

The Drift Tube Chambers

In the barrel region of the CMS muon system drift tube chambers are used to cover the large area and to fit the environment: the pollution from radiation and charged particles is one of the lowest inside CMS and the almost uniform magnetic field inside the chambers has a strength less than 1 T, because the flux is contained in the iron yoke (see figure 4.8).

Figure 4.9: *Picture of one CMS wheel equipped with drift tubes chambers and resistive plate chambers fixed on top of them (silver metallic rectangular solids) [51].*

The drift tube system consists of four concentric cylinders with growing diameter centered around the beam pipe. From inside to outside these so called stations are named MB1 to MB4 (Muon Barrel). With a length of 2.5 m the chambers follow the segmentation of the return yoke they are mounted at (see figure 4.9). Each wheel is divided into 12 azimuthal sectors which cover approximately 30° each. One such segment, a single "chamber", is the basic unit in the DT system, which consists in total out of 250 chambers.

A chamber is made of three "superlayers" (SL, the MB4 chambers consist of only two), where the inner[11] and outer so called ϕ-SL are separated maximally to increase the lever arm for the track measurement in the $r\phi$-bending plane. To be able to reconstruct a 3D-segment within a single chamber, the middle superlayer is rotated by 90° providing the

---

[11]Viewpoint from the interaction point respectively.
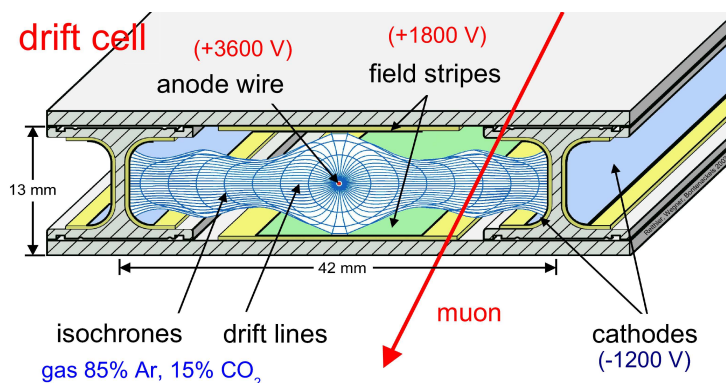
Figure 4.10: *Cross section of a CMS drift cell with drift lines of electrons and isochrones [52].*

z-coordinate (Θ-SL[12]). Both types of superlayers have the same substructure of four layers of drift tube cells.

A basic cell (see figure 4.10) has an outer width of 42 mm and a height of 13 mm. The length is depending on the superlayer type: constant 2.5 m the for ϕ-SLs and varying for the Θ-SLs, depending on the station. Along the centre a 50 μm gold plated steel wire, serving as anode, is stretched, which is fixed at the ends. In a single cell only the absolute distance to the wire can be measured. This left-right ambiguity is resolved by staggering the four layers of cells inside a superlayer by half a cell width.

The cathodes located at the edges of the cell are mounted at "I"-shaped aluminium beams, which isolate one cell from the other. In addition field shaping electrodes at the top and bottom of a cell are improving the linearity of the space-drifttime-relation. The cells are flushed with a gas mixture of 85% Ar and 15% CO_2, which provides good quenching properties, and a drift velocity of about 55 μm/ns.

This results in a maximum drift time of about 380–400 ns, which equals the time of about 16 bunch crossings. Inside a cell a hit can be measured with a precision of approximately 190 μs [53] and an efficiency larger than 99%.

Cathode Strip Chambers

The cathode strip chambers are located in an environment of a highly non-uniform magnetic field (up to 3.1 T, see figure 4.8), a high flux of charged particles and an intense rate of neutron background (background rate up to 1000 Hz/cm^2). Fixed on the endcap iron return yokes in a plane perpendicular to the beam, the CSC system is arranged in four discs per endcap (ME1 to ME4, Muon Endcap, counted from the interaction point outwards).

Beside the innermost station which is divided into three concentric rings of chambers all other stations consist of two rings. These rings are segmented into 18 trapezoidal chambers for the inner rings of the ME2–ME4 and into 36 chambers for the other rings. Apart from

---

[12]This kind of SL is missing in the outermost stations (MB4). Thus a 3D segment reconstruction within this chambers is not possible. The r-coordinate is always given by the location of the detector component.
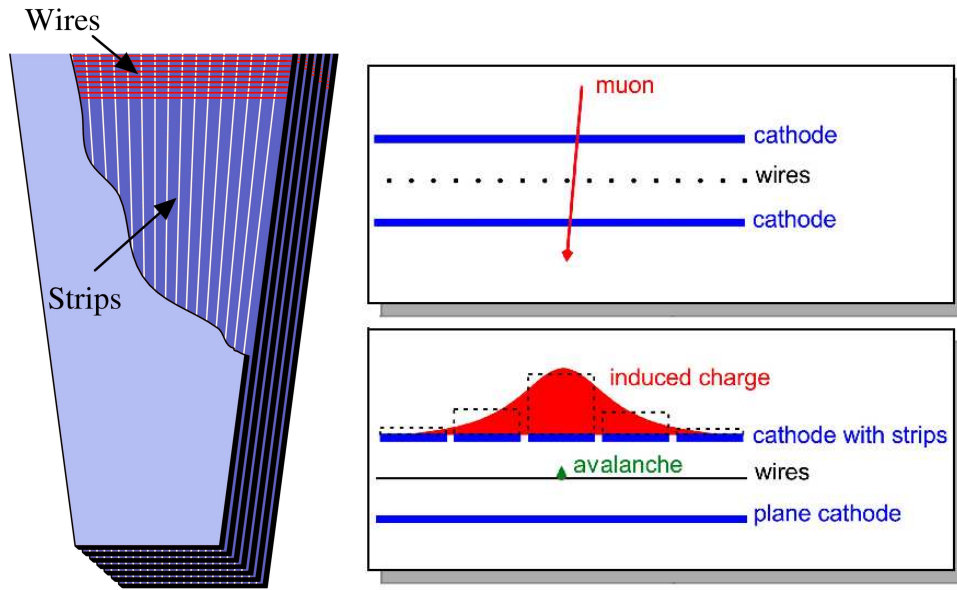
Figure 4.11: *Sketch of an endcap CSC (left) and its functional principle [46].*

the outermost ring of the first station ME1 all chambers have overlaps in the rϕ-plane to avoid dead regions.

The CSC system is constructed to achieve a high muon detection efficiency, to provide a robust and background rejecting pattern recognition and to improve the bunch crossing assignment. A single chamber is composed of six equal layers of active volume. Each layer is a multi-wire proportional chamber (see figure 4.11) defined by an array of 50 μs anode wires sandwiched between two parallel cathode planes, which are separated by a 9.5 mm gas gap (filled with a mixture of 30% Ar, 50% CO_2 and 20% CF_4). The cathodes are segmented into strips, which are aligned perpendicular to the wires in radial direction. Their width is chosen to cover a constant $\Delta\phi$-slice between 2 and 5 mrad and thus are also trapezoidal. A voltage of 4.1 kV is applied.

The chambers of the ring with the closest distance to the interaction point show minor differences in their mechanical construction: due to the high magnetic field of about 3 T in the z-direction and the resulting skewed drift of electrons, the gas gap is only 6 mm wide. The high-voltage counts roughly 3 kV and the wires, having a diameter of 30 μm are strung at a 25° angle in the chamber plane.

The CSCs are fast detectors suitable for triggering since the signals are read out from the strips as well as from the wires. Electrons from the gas ionisation along a muon track drift to the array of wires and develop an avalanche due to the increasing electric field. The moving charges induce a signal on several strips of the cathode plane. The interpolation of induced charges between adjacent strips results in a very fine spatial resolution of about 50 μm at normal muon incidence [46], which is used to measure the curvature of the track in the rϕ-plane. Simultaneously, the signal on the wires is read out to gain a measurement of the radial coordinate with a coarse precision of a few mm.
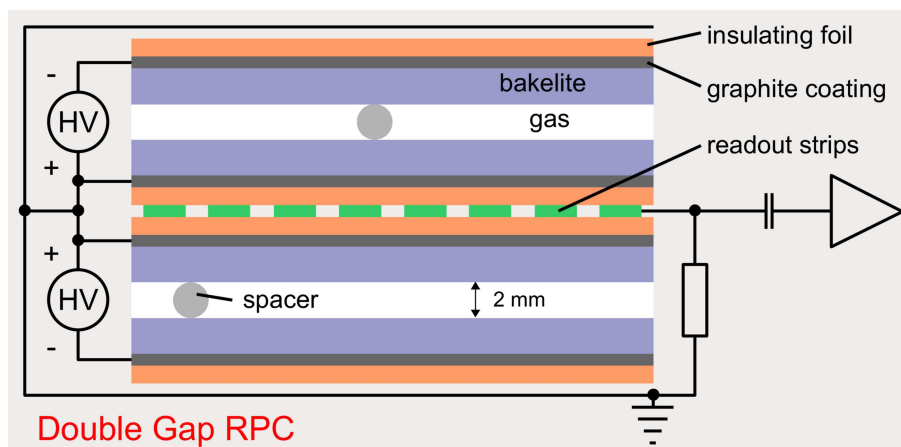
Figure 4.12: *Cross section of a double gap resistive plate chamber.*

Resistive Plate Chambers

The resistive plate chamber system is complementary to the other muon detectors: with their reasonable spatial resolution, but excellent time resolution of a few nanoseconds they are specifically designed for trigger purposes and add robustness and redundancy to the muon system.

In the barrel region the RPC chambers are directly attached to the DT chambers. The first two DT stations are sandwiched by RPCs to provide at least four measurements even for lower energetic muons, while only one RPC is attached to the outer two stations, respectively. In the endcaps, trapezoidal shaped resistive plate chambers are combined with the CSC system, resulting again in four discs which cover a range up to $|\eta| = 2.4$.

A single RPC chamber is made of a pair of parallel bakelite plates, separated by a 2 mm small gap filled with a gas mixture of 96% $C_2H_2F_4$, 3.5% i-C_4H_{10} and 0.5% SF_6 (for streamer supression). For an improved efficiency per station double gap RPCs (see figure 4.12) are used. To apply the high voltage of 9.5 kV the highly resistive plates are coated with graphite electrodes. Insulated aluminium strips are placed inbetween the two single resistive plate chambers as a common readout.

This double-gap layout is chosen to compensate the weaker induced signal caused by the operation of the RPCs in the "avalanche" mode rather than in the more common "streamer" mode, to sustain higher rates. However, the gas amplification is reduced and an improved electronic gain is required.

In the barrel the RPC readout strips, with a length of 80 or 120 cm, are aligned parallel and in the endcaps, with a length of 25 to 80 cm, perpendicular to the beam line. The width is determined to cover always $(5/16)°$ in the ϕ-coordinate and thus increases with the distance to the beam. By signal interpolation of adjacent strips this coordinate is measured, while the position parallel to the strip is only constrained by the strip length.

A critical point in the operation of the RPCs is the flatness of the bakelite surface. Local bumpiness results in an increase of the electric field and causes intrinsic noise. A solution for surface smoothing is the treatment of the bakelite electrodes with linseed oil, which also absorbs UV quanta from avalanches. CMS has made the choice of oiling all barrel and endcap RPCs up to $|\eta| = 1.6$. The remaining RPCs are supposed to be non-oiled to avoid

potential aging effects, which might be related to degeneracy of the oil in this region due to very high particle fluxes [54].

The momentum resolution $\Delta p_T / p_T$ of the muon system stand-alone is expected to be 8–15% (20–40%) for muons with transverse momenta of 10 GeV (1 TeV) depending on η. In combination with the tracker the resolution can be improved to 1–1.5% (6–17%).

4.2.7 The CMS Trigger and Data Acquisition

The LHC environment presents challenges to the trigger and data acquisition system [39, 47] much more demanding than those encountered at past and present experiments worldwide. The bunch crossing rate of 40 MHz and an average of 20 interactions per bunch crossing plus additional overlapping events result in approximately 10^9 interactions per second. CMS has more than 10^8 readout channels resulting in a data rate of the order of 10^{15} bits per second at full operation. After zero suppression still 1 MB of data will be recorded for one bunch crossing. Since today's permanent storage devices such as tape drives are only able to cope with a data rate of about 100 Hz, the events containing "interesting" physics are sorted out and written to tape. Thus the stored number of events is reduced by a factor of 10^7.

Trigger	Low luminosity		High luminosity	
	Threshold [GeV]	Rate [kHz]	Threshold [GeV]	Rate [kHz]
Inclusive isolated electron/photon	29	3.3	34	6.5
Di-electron/di-photon	17	4.3	19	3.3
Inclusive muon	14	2.7	20	6.2
Di-muons	3	0.9	5	1.7
Single tau-jet	86	2.2	101	5.3
Two tau-jets	59	1.0	67	3.6
1-jet, 3-jets, 4-jets	177, 86, 70	3.0	250, 110, 95	3.0
Jet * $E\!\!\!/_T$	88 * 46	2.3	113 * 70	4.5
Electron * jet	21 * 45	0.8	25 * 52	1.3
Muon * jet	./.	./.	15 * 40	0.8
Minimum-bias (calibration)		0.9		1.0
Total		16.0		33.5

Table 4.2: *The CMS L1 trigger table at low ($\mathcal{L} = 2 \cdot 10^{33}$ cm^{-2} s^{-1}) and high luminosity ($\mathcal{L} = 10^{34}$ cm^{-2} s^{-1}). The listed thresholds correspond to values at which the efficiency of the trigger is 95% of its maximum value. The n-jet trigger selection depends on the p_T-threshold for the highest energetic jet in an n-jet event. The combined triggers like "Electron * Jet" demand the fulfillment of both citeria at once. For details see [39, 47].*

The CMS level-1 trigger is designed to reduce the initial bunch-crossing rate of 40 MHz to 10^5 events read out per second. Using only coarse detector data from muon detectors and calorimeters the first level trigger generates dead time free decisions every 25 ns with

the thresholds and rates given in table 4.2. Due to the limited storage capacity of detector readout buffers the decision must be available 3.2 μs after the corresponding bunch crossing.

The reduction of the rate is performed in several steps, which form a series of progressively more complex, but also time consuming levels. The first level (level-1 trigger) lowers the passed rate of events from 40 MHz to 100 kHz. The following levels comprised as high-level trigger (HLT) have more time for the decision and further reduce the rate to finally 100 Hz. The first level is based on custom pipelined hardware processors, whereas the HLT is based on PC farms.

If an event is accepted at level 1 the full detector information is read out and passed to the high-level trigger online farm of about 1000 commercial CPU's. Highly sophisticated algorithms are used to reconstruct the event. If events contain "interesting" physics they are written to tape with a rate of 100 Hz.

4.2.8   Luminosity Monitoring

Since the luminosity relates the cross section σ to the event rate according to equation (4.2), it is the most important parameter of the LHC apart from the centre of mass energy. Therefore the precise determination and monitoring of the luminosity is necessary during the whole operation of the LHC. There are several methods to provide such a measurement. Two of them are discussed here.

Direct Measurements

In practice two methods are used to measure the luminosity directly at colliders. By the measurement of the beam parameters, such as the bunch geometry and the particle density within the beam, the luminosity can be directly obtained from equation (4.3). This method does not result in a very precise luminosity measurement ($\Delta\mathcal{L}/\mathcal{L} \approx 10\%$) because an accurate measurement of the beam currents and especially of the beam size at the interaction point is difficult.

The second direct method is based on equation (4.2). If the rate of a special process can be measured precisely and its cross section is well known from theoretical calculations, the luminosity is given as the ratio of both. The precision for this luminosity determination is limited by experimental corrections to the rate, like detector acceptance and efficiencies. The precision of the luminosity measurement, which can be achieved with this method, is comparable to the first method.

Measurement via the Optical Theorem

Using the TOTEM detector the luminosity will be determined through the measurement of the total cross section. It is based on the simultaneous measurement of small angle elastic scattering and of the total inelastic rate. The total cross section σ_{tot} can be expressed in terms of the number of elastic and inelastic interactions N_{el} and N_{inel} within an integrated luminosity L_{int} by

$$N_{\mathrm{inel}} + N_{\mathrm{el}} = L_{\mathrm{int}}\, \sigma_{\mathrm{tot}}. \tag{4.8}$$

Taking the optical theorem into account, which relates the total cross section σ_{tot} to the imaginary part of the forward scattering amplitude $F(0)$,

$$\sigma_{\mathrm{tot}} = \frac{4\pi}{p^*}\,\mathrm{Im}(F(0)) \tag{4.9}$$

one can transform the differential elastic scattering at zero angle,

$$\left(\frac{d\sigma_{\mathrm{el}}}{d\Omega^*}\right)_{\theta=0°} = |F(0)|^2 = (\mathrm{Re}(F(0)))^2 + (\mathrm{Im}(F(0)))^2 \tag{4.10}$$

into

$$\left(\frac{d\sigma_{\mathrm{el}}}{d\Omega^*}\right)_{\theta=0°} = (1+\rho^2)(\mathrm{Im}(F(0)))^2 = (1+\rho^2)\left(\frac{p^*\sigma_{\mathrm{tot}}}{4\pi}\right)^2. \tag{4.11}$$

p^* is the momentum of the scattering particles in the rest frame and ρ has been defined as ratio $\rho = \mathrm{Re}(F(0))/\mathrm{Im}(F(0))$.

Replacing the differential cross section per rest frame solid angle Ω^* by the differential cross section per momentum transfer t related by

$$\left(\frac{d\sigma_{\mathrm{el}}}{dt^*}\right)_{t=0} = \frac{\pi}{p^{*2}}\left(\frac{d\sigma_{\mathrm{el}}}{d\Omega^*}\right)_{\theta=0°} \tag{4.12}$$

one obtains

$$\left(\frac{d\sigma_{\mathrm{el}}}{dt^*}\right)_{t=0} = \frac{\sigma_{\mathrm{tot}}^2}{16\pi}(1+\rho^2). \tag{4.13}$$

Replacing the cross sections partly by event rates results in

$$\left(\frac{dN_{\mathrm{el}}}{dt}\right)_{t=0} = (1+\rho^2)\,\sigma_{\mathrm{tot}}\left(\frac{N_{\mathrm{el}}+N_{\mathrm{inel}}}{16\pi}\right), \tag{4.14}$$

thus

$$\sigma_{\mathrm{tot}} = \left(\frac{dN_{\mathrm{el}}}{dt}\right)_{t=0}\frac{16\pi}{N_{\mathrm{el}}+N_{\mathrm{inel}}}\frac{1}{1+\rho^2}. \tag{4.15}$$

The TOTEM experiment will measure dN_{el}/dt at small t and N_{el} with its so called Roman Pots, while simultaneously measuring N_{inel} with a forward inelastic detector (also part of TOTEM, see [55]) and the CMS hadronic forward calorimeter. Using equation (4.15) the total cross section σ_{tot} can be calculated and used within formula (4.8) to obtain the luminosity.

Using this method the cross section is expected to be determined with an error smaller than 5% [55].

Chapter 5

Simulation and Reconstruction

To simulate the possibility of a W' boson detection in a special production and decay channel, so called Monte Carlo simulations are performed. The first stage of such a simulation is the generation of an elementary physics process in which the W' is created from two proton constituents. Subsequently the W' is forced to decays into a muon and a neutrino. This task is performed by "generators" like PYTHIA. As a result one obtains a creation and decay chain, which conforms to an isolated processes without any interaction with matter.

Although many interesting features of a process, like the angular distribution of the decay products, can already be studied with the events at generator level, a full simulation of the particles interacting with the detector material is necessary to predict a possible detection. Huge efforts have been made to model the CMS detector in detail and to simulate the response of particles within the active detector volume. For a realistic simulation the material distribution of the whole detector has to been known and parametrised in order to track particles through it. An important component of the simulation is also the modeling of the readout system. The retrieved "readout information" obtained from the simulation is used to reconstruct and identify the particles and their tracks and to determine their properties. Comparing the reconstructed events with the generator input gives physicists a feedback on the expected detector performance and the possibility to check the algorithms used for the reconstruction.

The advantage of such a computer simulation is obvious: without any detector component being built the detector can be studied and the design goals can be validated. Already at this level selection criteria for the analysis of a special process can be defined in order to extract a clear signal. In the ideal case the detector simulation results in the same output as a running detector. An analysis, which has been developed with simulated data, can therefore be adopted easily to data taken from the detector.

5.1 The CMS Simulation Chain

In order to give an overview of the detector simulation sequence the used programs are explained in their timely order following figure 5.1. In each subsequent step the output of the former program is used as input for the following. Technically the sequence is separated into four steps:
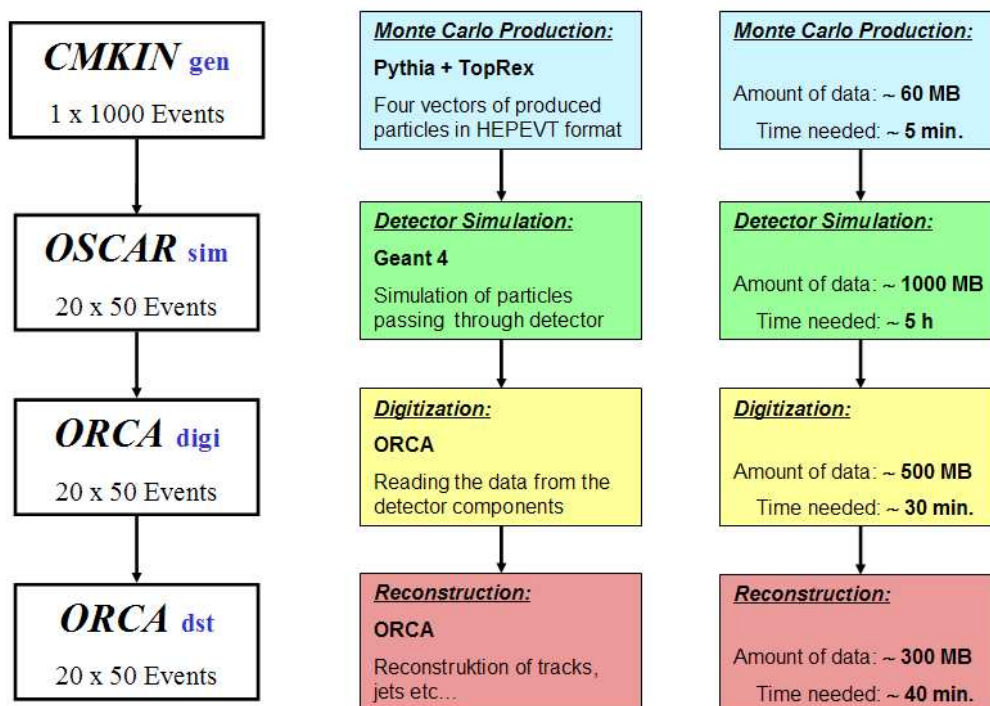
Figure 5.1: *The CMS chain for the full detector simulation [56]. In the left column the used programs are shown with a possible division of events per job. While at generator level (CMKIN) all events can be processed in one job, the further simulation (OSCAR, ORCA) is done in parallel splitting the 1000 events in 50 events per job. The parallel processing is necessary to obtain the fully simulated data in a reasonable time (for processing times and obtained amount of data see right column).*

- CMKIN:
  The first step is the creation of the particle under study and its subsequent decay at generator level e.g. in case of a W' a process of the form $q\bar{q} \to W' \to \mu\nu$. In CMS this part is performed by the Fortran based CMKIN [57] program, which is an interface to various event generators like PYTHIA [58, 59], HERWIG [60], TopRex [61] and many more. It is steered by "data cards" (for an example see appendix A.1), which specify the process to be generated and the parameters to be used. Generators are not experiment specific. The centre of mass energy and the process, in which the W' should be created in pp-collisions are given as input. Additional parameters and switches varying for the different generators can be set. The CMKIN interface provides the flexibility to change all parameters depending on the event generator. In addition selection criteria can be implemented already at this stage to avoid the simulation of events, which can not be detected for some reasons e.g. because they are outside the η-acceptance region of the detector under study.
  As a result one obtains the decay chain of a process in the so called HEPEVT format. For each particle its type, mother particle, momentum, energy, mass and the point of creation is given (see figure 5.2).

- OSCAR:
  Up to now the physical processes are simulated in vacuum with no interactions of the

```
  I particle/jet KS     KF  orig     p_x        p_y        p_z         E          m

  1 !p+!         21   2212    0     0.000      0.000   7000.000   7000.000      0.938
  2 !p+!         21   2212    0     0.000      0.000  -7000.000   7000.000      0.938
==================================================================================
  3 !dbar!       21     -1    1     0.813      0.549    982.048    982.048      0.000
  4 !u!          21      2    2     0.646      1.501   -924.578    924.580      0.000
  5 !dbar!       21     -1    3    29.744      5.783    884.355    884.874      0.000
  6 !u!          21      2    4   -50.149    -15.717   -131.855    141.942      0.000
  7 !W'+!        21     34    0   -20.404     -9.933    752.501   1026.816    698.269
  8 !mu+!        21    -13    7   110.513    319.001    439.999    554.594      0.106
  9 !nu_mu!      21     14    7  -130.918   -328.934    312.502    472.223      0.000
==================================================================================
 10 (W'+)        11     34    7   -20.404     -9.933    752.501   1026.816    698.269
 11 gamma         1     22    4    -0.187      1.856   -308.772    308.778      0.000
 12 nu_mu         1     14    9  -130.918   -328.934    312.502    472.223      0.000
 13 mu+           1    -13    8   109.994    317.549    437.986    552.058      0.106
 14 gamma         1     22    8     0.520      1.452      2.013      2.536      0.000
    ...          ..     ..    .     .....      .....      .....      .....      .....
```

Figure 5.2: *Event listing of a W′ generated by the Monte Carlo program* PYTHIA. *For each particle some status codes, their mother particle, momentum components, energy and mass are given. While the first two lines describe the overall reaction (p on p, each having 7 TeV momentum in z-direction), the second part summarizes the reaction at parton level: an anti-d-quark and an u-quark, which undergo initial state radiation (details are not shown in the listing), create a positively charged W′. The W′ subsequently decays into a muon and a neutrino. The last part of the listing (several 100 lines) shows the detailed reaction of all involved particles including "beam remnants", initial and final state radiation and the decay of short lived particles.*

occurring particles with matter. The **O**bject-Oriented **S**imulation for **CMS A**nalysis and **R**econstruction OSCAR [62] takes the CMKIN output as input and tracks the particles through the detector. Since the detailed detector is parametrised (material distribution and properties, magnetic field *etc.*) OSCAR simulates the decay of (long lived) particles, but also the energy loss and scattering of particles along their tracks. With the help of GEANT4 [63] (**Ge**ometry **an**d **T**racking) each particle and its decay products are traversed through the detector simulating the interaction with the material.

Due to the high multiplicity of particles and the various interactions within the detector material, this part of the simulation needs a large amount of computing time.

- ORCA-Digitisation:

  In the next step the readout is simulated by the **O**bject-Oriented **R**econstruction for **CMS A**nalysis ORCA [64]. According to the signal deposits given by OSCAR, the response of the detector and of the readout electronics is simulated.

  Before performing the digitisation of the detector signals, background from minimum bias events can be mixed with the signal event (see figure 5.3). Due to the high luminosity and the short time between two bunch crossings particles from previous collisions still pass through the detector while new collisions occur. This enlarges the occupancy and thus the difficulty of track reconstruction and bunch crossing assignment. By the mixture of underlying events with the signal event these effects can be studied.
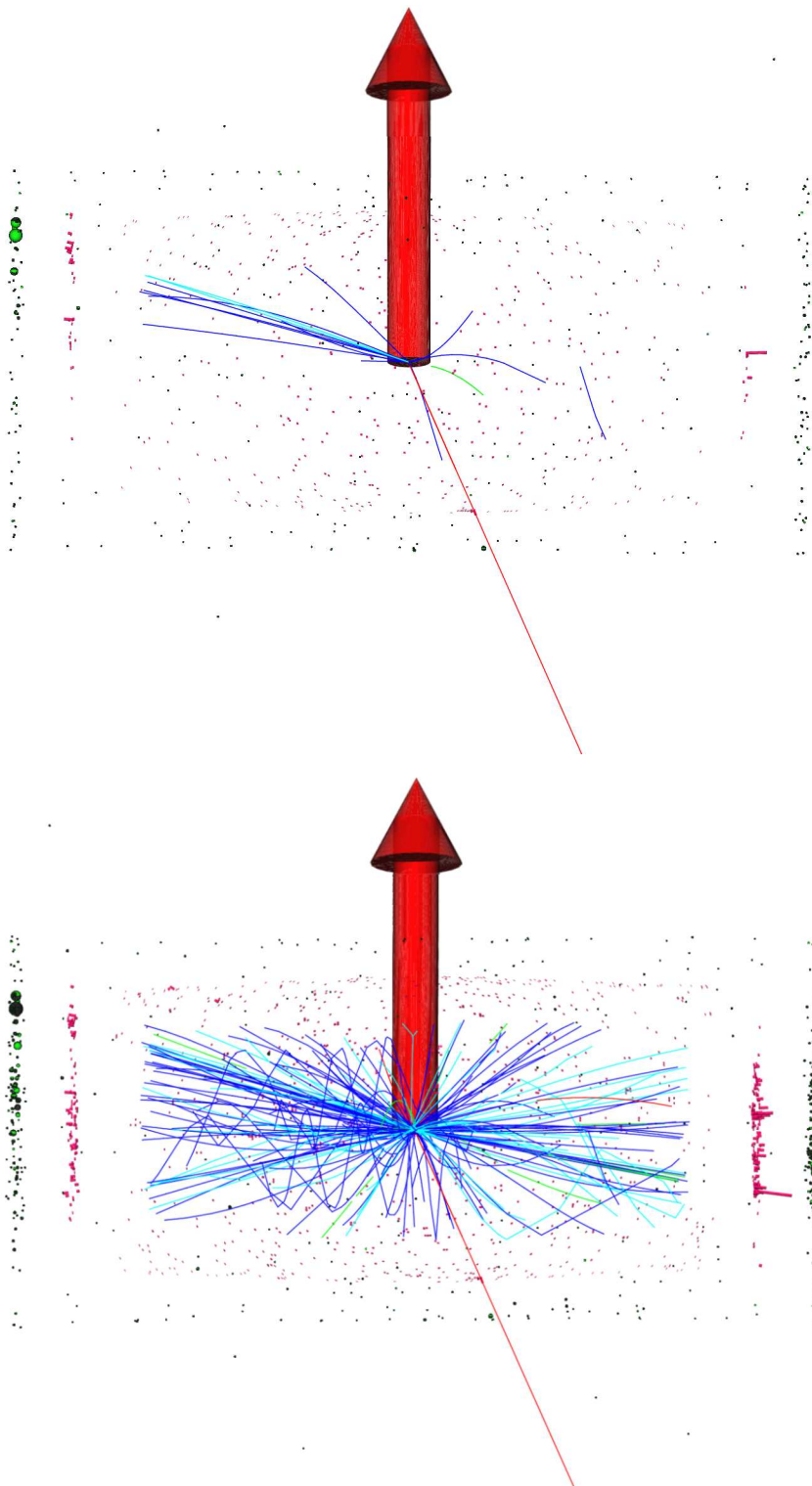
Figure 5.3: *Event display (*IGUANACMS*) showing an identical event, once with pileup events (below) once without (above). The tracks within the tracker ($p_{\mathrm{T}} > 5$ GeV, blue = pions, green = electrons, red = muons, red arrow = transverse missing energy, cyan = rest) and the energy deposit in the ECAL (barrel + endcap, purple) and the HCAL (barrel, green) are shown.*

- ORCA-Reconstruction:
  The final part is the reconstruction of high-level objects, like identified particles, jets or vertices and their parameters. This part of the CMS software is implemented as flexible as possible, so that it is used for the reconstruction of simulated events as well as for data originating from an operational CMS detector. Since the rate of recorded events will be limited to 100 Hz, triggers set constraints on the passed events. This emulation of the triggers has been included into the CMS simulation framework and dedicated physics analyses are performed to study trigger efficiencies. By defining trigger parameters special data samples can be extracted, e.g. a high-p_T muon sample and the effect of triggers on a dedicated analysis can be investigated.
  The CMS framework is designed in an object-oriented way to allow maximum flexibility. Several algorithms can be used at the same time for the reconstruction of one object (use of different jet algorithms or special TeV-muon reconstructors). The output is stored in so called DST-files, which contain the reconstructed objects in a persistent way. With the ORCA interface these files can be interactively analysed. For details of the access to simulated and reconstructed data using ORCA see [65].

- IGUANACMS:
  This program is not part of the simulation chain, but allows the graphical display of the intermediate results. It is derived from the modular toolkit IGUANA [50], which is used for interactive visualisation and analysis. With the help of a graphical user interface simulated and later also real data can be displayed. It allows an interactive view of the detector including physics events and detailed information about the physics objects. IGUANACMS is able to visualise the output of each production step and is thus a helpful tool for the understanding of event topologies or detector effects.

5.2 CMS and the Grid

The generated amount of data from the experiments located at the LHC will exceed by far the data volume encountered at past and present experiments worldwide (for details see [66]). The detector will produce approximately 1 TBit/s raw data that has to be stored. The total amount expected is about 5–6 petabytes per year running at high luminosity. Thus, the requirements of data handling are very large in terms of computational power, data storage capacity, data access performance and the associated human resources for operation and support. Since it is not feasible to fund all of the resources at one site it has been agreed that the LHC computing service will be implemented as a geographically distributed computing data grid.

The computing grid is based on the idea of connecting different low cost computer clusters. By interconnecting them using specific software, called middleware, one can parallelise the execution of jobs and achieve almost the same performance as with a huge expensive supercomputer.

The institutes participating at the LHC experiments are developing a common grid infrastructure, the LHC Computing Grid (LCG). It is adapted to the special requirements of high energy physics experiments and will consist of a hierarchical structure. As a test run the official Monte Carlo production, i.e. the generation of fully detector simulated
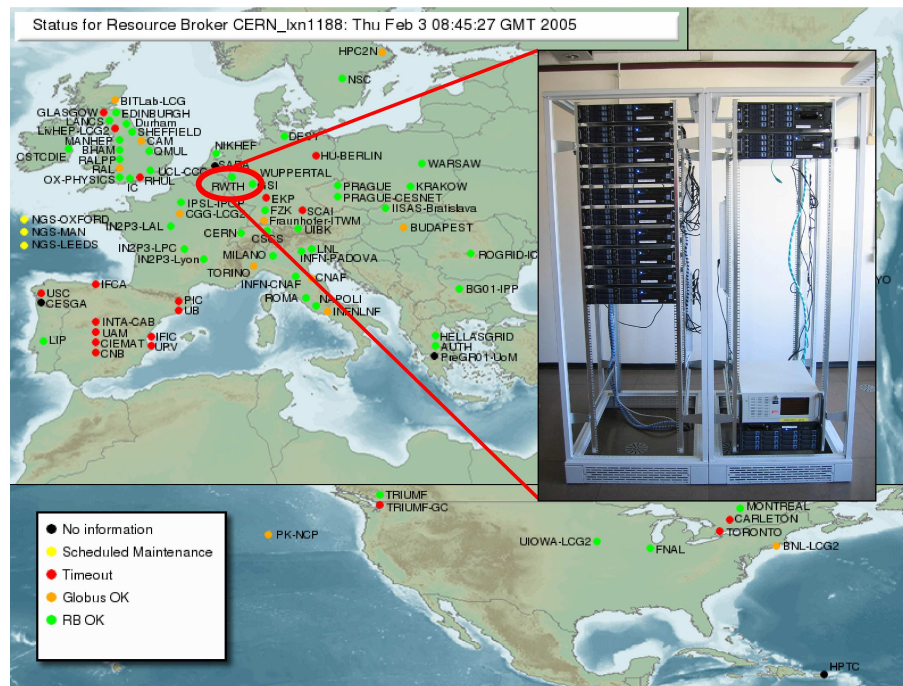
Figure 5.4: *The graphic shows the sites of the LHC Computing Grid community. As an example the new grid cluster installed at Aachen III. Phys. Inst. since May 2005 is displayed.*

events (explained in the previous chapter), is already performed using the evolving grid structure.

According to the grid idea the simulated data samples are calculated all over the world and are written to local storage elements, which are accessible via the grid. The analysis of a special data set is performed, if possible, at the same site where the data, which should be processed, are located. ORCA-jobs, which analyse a dedicated event sample, e.g. a *WW*-sample, are shipped to the site, where the data are located and the analysis is ran on the local grid-cluster. After finishing, the results of the analysis are sent back to the submitting person. In difference to past experiments the data are not transfered to the physicist who wants to analyse them, but the jobs are sent to the data.

CRAB

Recently the CMS community has developed a bunch of PYTHON scripts to simplify the handling of interactive ORCA analysis jobs, which are processed using the LHC Computing Grid. The collection of tools are pooled in the **CMS R**emote **A**nalysis **B**uilder CRAB.

Given a prepared ORCA analyis job CRAB builds the according jobs ready for the submission into the grid. Via a configuration file the user can specify the data sample and the kind of data to be analysed. CRAB takes these inputs to locate the data sample within a database and sets the destination where the job is executed automatically. Further parameters like the number of jobs and the number of events to be processed per job can be set to optimise the job execution. After the grid job creation, CRAB can be used for the job submission and the monitoring of the job status. The output of processed jobs can be retrieved, or, in case of job failures, a resubmission can take place.

Chapter 6

The W' at Generator Level

Before starting with the analysis of the full detector-simulated data, the properties of the W' are presented. In an experiment the W' can only be investigated indirectly through its decay products. Therefore the W' and the decay $W' \rightarrow \mu\nu$, based on Altarelli's Reference Model are reviewed at generator level using PYTHIA. The study of these basic properties gives a deeper insight in the nature of the reaction and can help to develop selection criteria.

6.1 W' Production Properties

The cross section and width of the W' have already been discussed in chapter 3.3. The W' cross section (total and $W' \rightarrow \mu\nu$) and the number of W' events decaying into muons for an integrated luminosity of 10 fb^{-1} are stated in table 6.1 for different W' masses.
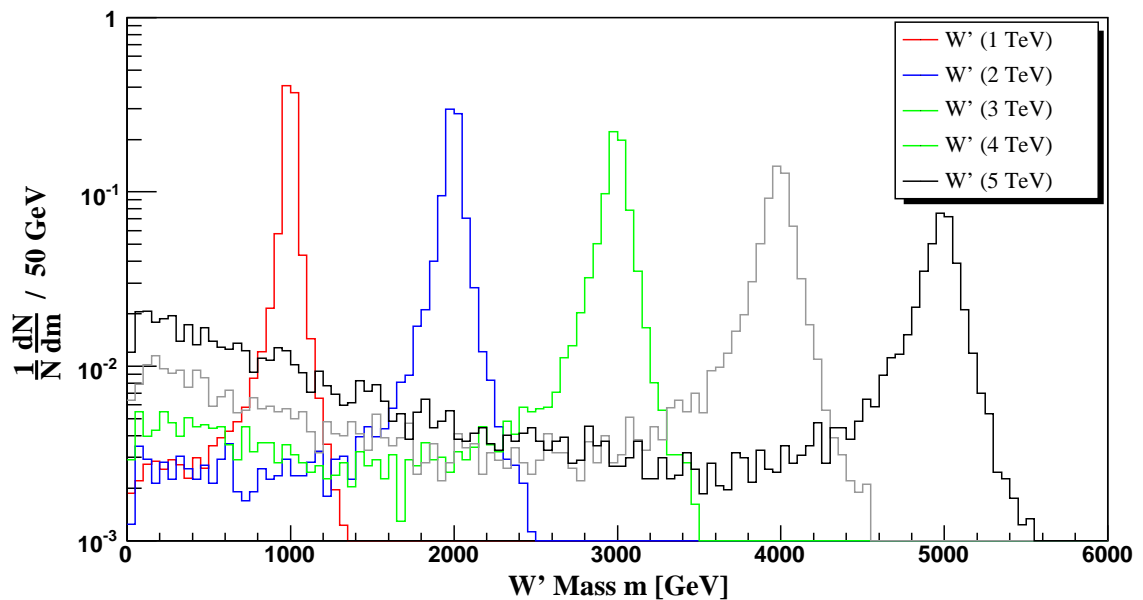
Figure 6.1: *The normalized mass distribution of W' bosons with different masses show a Breit-Wigner resonance at the nominal mass (peak). For a 5 TeV W' mass the distribution has a significant off-shell part (left of the peak).*

Process	Cross Section [fb]		Events in 10 fb^{-1}	
	Total	$W' \to \mu\nu$	Total	$W' \to \mu\nu$
$q\bar{q} \to W'$ (1 TeV)	$3.79 \cdot 10^4$	$3.11 \cdot 10^3$	379000	31100
$q\bar{q} \to W'$ (2 TeV)	$1.93 \cdot 10^3$	$1.58 \cdot 10^2$	19300	1580
$q\bar{q} \to W'$ (3 TeV)	$2.23 \cdot 10^2$	$1.82 \cdot 10^1$	2230	182
$q\bar{q} \to W'$ (4 TeV)	$3.50 \cdot 10^1$	$2.87 \cdot 10^0$	350	29
$q\bar{q} \to W'$ (5 TeV)	$7.41 \cdot 10^0$	$6.07 \cdot 10^{-1}$	74	6
$q\bar{q} \to W'$ (6 TeV)	$2.31 \cdot 10^0$	$1.90 \cdot 10^{-1}$	23	2
$q\bar{q} \to W'$ (7 TeV)	$1.04 \cdot 10^0$	$8.56 \cdot 10^{-2}$	10	1
$q\bar{q} \to W'$ (8 TeV)	$5.72 \cdot 10^{-1}$	$4.69 \cdot 10^{-2}$	6	< 1

Table 6.1: *W' cross section at the LHC centre of mass energy of 14 TeV for various W' masses. Also the cross sections times branching ratio for the process $q\bar{q} \to W' \to \mu\nu$ are given. For an integrated luminosity of 10 fb^{-1} the expected number of events are stated.*

6.1.1 W' Mass Distribution

The W' mass distributions, normalized to the cross section, for nominal masses of 1–5 TeV (see figure 6.1) have different shapes, depending on the production process.

W' bosons with a mass of 1 TeV are almost all produced within the so called Breit-Wigner resonance around the nominal mass. In contrast to that, the 5 TeV W' bosons are spread over a range of 0–5.5 TeV and have a smaller fraction in the Breit-Wigner resonance. Since heavy gauge bosons occur only as intermediate states they can be either produced at the nominal mass (on-shell), or with a lower mass (off-shell). However the off-shell production is strongly suppressed. If the centre of mass energy provides enough energy for the production of a massive particle, the on-shell part dominates as in the case of a 1 TeV W'. For larger W' masses the off-shell suppression has a smaller effect than the kinematic constraints and more and more W' bosons are produced with a mass substantially smaller than the nominal mass.

6.1.2 W' Momentum and Energy Distribution

At a collider the interacting partons carry large longitudinal p_{L} but only little transverse momenta p_{T}. Although the mass distributions of the W' bosons of various nominal masses are totally different, the transverse and longitudinal momenta of the W' bosons displayed in figure 6.2 are nearly identical. This is not obvious since the required energy for a 1 TeV W' is much smaller than the energy needed for a 5 TeV W'.

The transverse momentum of the W' is determined by the transverse momentum of the colliding partons and the initial state radiation, i.e. by the transverse momentum of the particles, which are emitted by the partons before they create the W'. Independent from the W' mass the boson's p_{T} is mainly below 100 GeV and thus small compared to its mass.

The longitudinal momenta, determined by the longitudinal momenta of the colliding partons, are significantly larger. While the longitudinal momentum distribution has its maximum at zero, momenta $|p_{\mathrm{L}}|$ up to 3 TeV show, that often one of the partons carries a
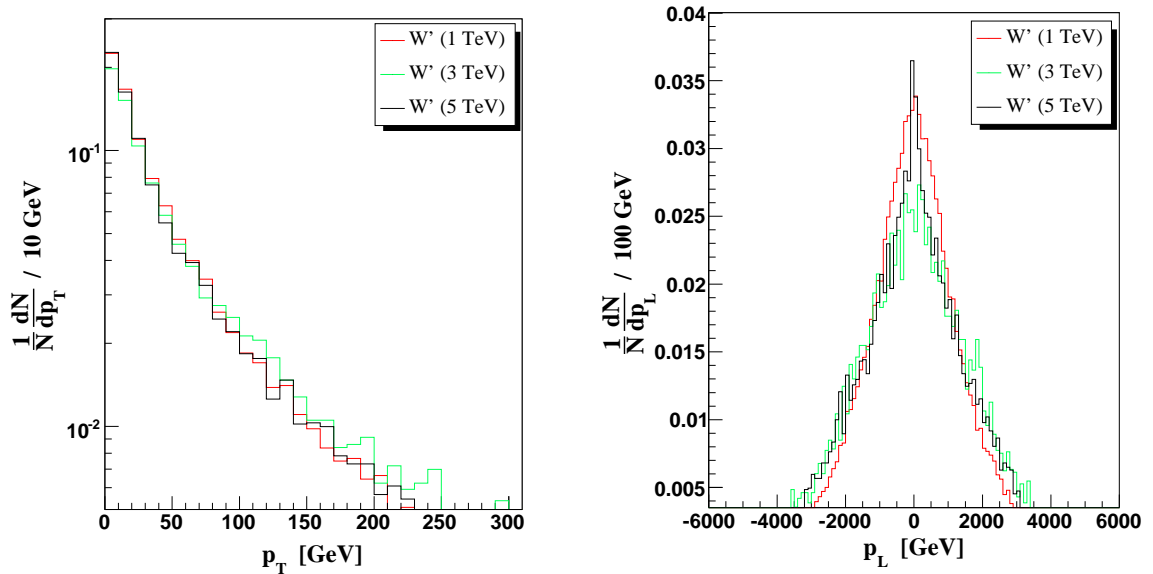
Figure 6.2: *Transverse (left) and longitudinal (right) momentum of the W'. Only a slight dependence on the W' mass is visible in the distributions. While the transverse momenta are small compared to the W' mass, the longitudinal momenta reach up to 3 TeV.*

significant larger momentum than the other. Due to the off-shell production of very heavy bosons, also a W' with a nominal mass of 5 TeV can carry a large longitudinal momentum.

The energy of the W' is given by its mass and its longitudinal momentum, since the transverse momentum is negligible compared to its longitudinal momentum. Therefore the energy distribution is given as a mixture of the mass distribution (Breit-Wigner resonance plus off-shell fraction) and the longitudinal momentum distribution (see figure 6.3).

6.1.3 W' Angular Distributions

The angular distributions of the W' bosons are explicable by the momentum distributions. Due to the large longitudinal momenta compared to the transverse, the W' bosons are mainly flying along the beam direction. Most of the W' bosons leave the interaction point under θ-angles smaller than 15° (see figure 6.4).

Since the W' production has no preferred direction in the transverse plane, the ϕ-angle distribution is uniform as shown in figure 6.4.

6.2 W' Decay into a Muon and a Neutrino

The properties of the muon and the neutrino are dominated by the properties of the W'. Without any detector effects the distributions are studied at generator level.

6.2.1 Transverse Momentum

In the rest frame of the decaying W' the energy of the muon and the neutrino is simply one half of the W' mass $M_{W'}$, respectively. Thus, in principle the energy measurement of the lepton can be used for the determination of the W'. However this measurement suffers from
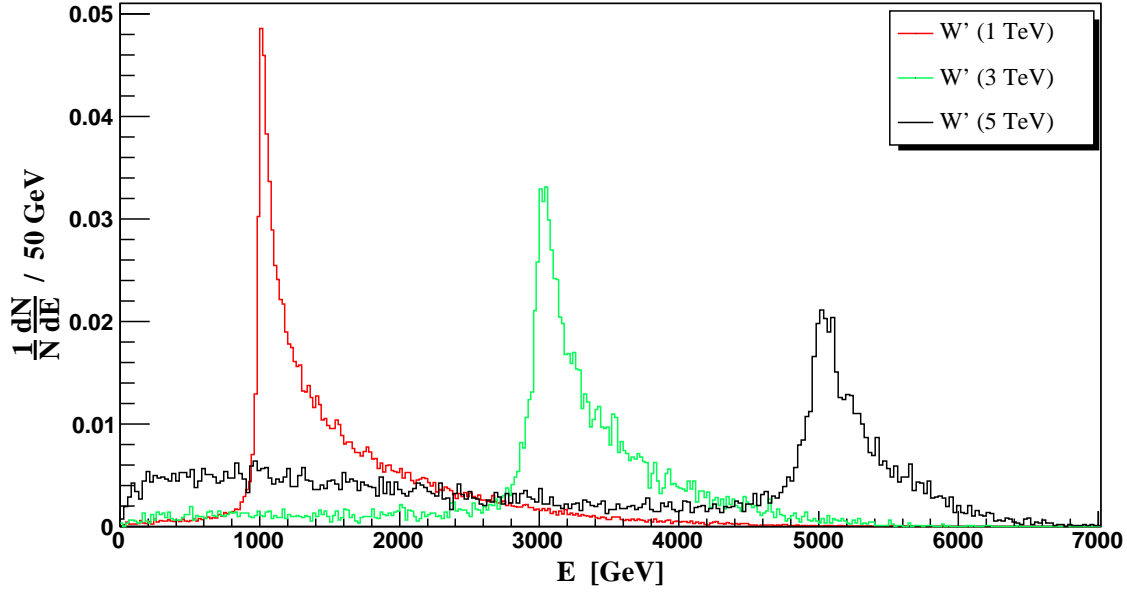
Figure 6.3: *W′ energy distribution for various W′ masses. The graphs are determined by the mass distribution (figure 6.1) as well as by the longitudinal momenta distribution (figure 6.2) of the W′.*

a general problem concerning neutrinos at colliders: they are only indirectly detectable as an energy imbalance, which can only be determined in the transverse plane, since a sufficient amount of energy is taken away through the beam pipe. Therefore it is difficult to reconstruct the rest frame of the $W′$ at a collider experiment precisely. Fortunately, the transverse momentum of the muon, which is invariant under boosts along the z-axis, comprises also information about the mass.

In the rest frame of the $W′$ the angular distribution of the muon and the neutrino is given by the V-A structure of the weak charged current [32]

$$\frac{1}{\sigma}\frac{d\sigma}{d\cos\theta^*} \sim (1 + \cos\theta^*)^2, \tag{6.1}$$

with θ^* as the scattering angle in the $W′$ rest frame (see figure 6.6).

To get an estimate of the p_T-distribution one can assume the production of the $W′$ without any transverse momentum. The polar angle θ^* of the muon in the rest frame is then given by its transverse momentum

$$\cos\theta^* = \left(1 - \frac{4p_{T_\mu}^2}{M_{W′}^2}\right)^{\frac{1}{2}}. \tag{6.2}$$

Substituting the cosine in equation (6.1) one obtains

$$\frac{1}{\sigma}\frac{d\sigma}{dp_{T_\mu}} \sim \frac{p_{T_\mu}}{M_{W′}^2}\left(1 - \frac{4p_{T_\mu}^2}{M_{W′}^2}\right)^{-\frac{1}{2}}\left(1 - \frac{2p_{T_\mu}^2}{M_{W′}^2}\right). \tag{6.3}$$

For small transverse momenta p_{T_μ} the terms in brackets are equal to 1 and the distribution grows linearly with p_{T_μ}. Tending towards $p_{T_\mu} = M_{W′}/2$ the distribution shown in
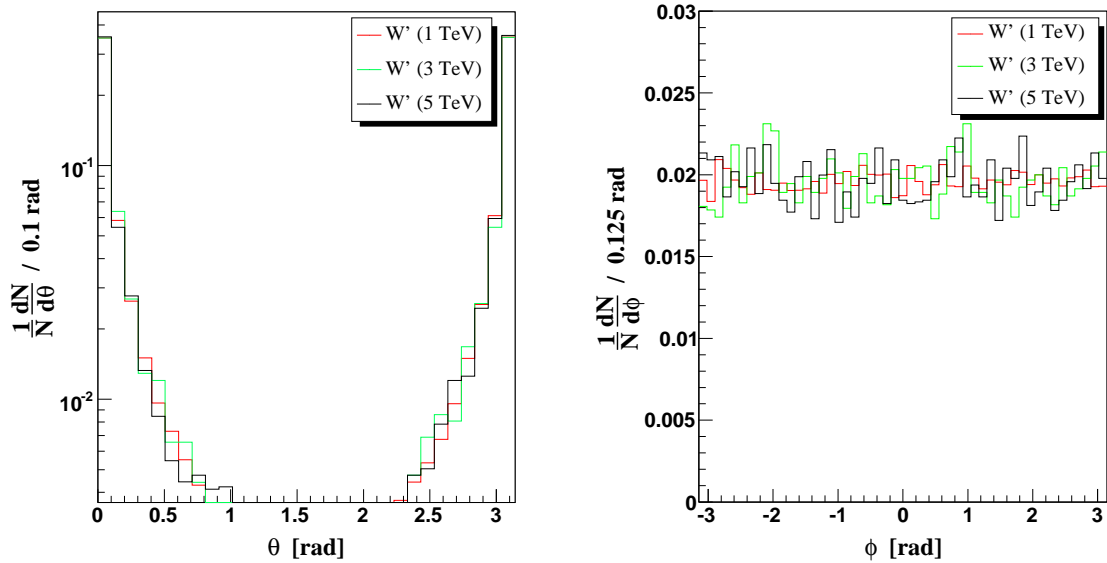
Figure 6.4: *The angular distributions of the W' for different masses are shown. Due to the similar momentum distributions for different W' masses, displayed in figure 6.2, the θ- (left) and ϕ-distributions are also mass independent. While no ϕ direction is preferred for the W', most of them are flying along the beam line.*

figure 6.5 strongly peaks in a so called Jacobian peak. Especially for the muons arising from a 1 TeV W', the distribution follows the formula above: the graph is linearly increasing with the transverse momentum and rapidly falling to zero at half of the W' mass. The distribution is not abruptly stopping at this point and slightly smeared out due to the finite width (see figure 6.1) and the non-zero transverse momentum of the W' (see figure 6.2), which had been assumed in the estimate.

It remains the question why the transverse momentum spectrum for the leptons from the 5 TeV W' looks so different? The answer is again given by the mass distribution of the W' shown in figure 6.1. Due to the significant off-shell production of W' bosons with a mass around 5 TeV the muon and neutrino transverse momenta are also following this distribution. However a small Jacobian peak is still visible at half of the nominal W' mass.

6.2.2   Transverse Invariant Mass

To obtain a more characteristic signal, not only the muon information, but also the measurable properties of the neutrino should be taken into account. Identifying the magnitude and the azimuthal angle of the missing transverse energy with transverse momentum of the neutrino, one can define the so called transverse invariant mass,

$$M_{\mathrm{T}}^2 = 2 p_{\mathrm{T}_\mu} \, p_{\mathrm{T}_\nu} (1 - \cos \Delta\phi_{\mu\nu}), \qquad (6.4)$$

with $\Delta\phi_{\mu\nu}$ as the angle between the transverse momentum of the muon p_{T_μ} and the neutrino p_{T_ν}, which are both constrained to the transverse plane. In analogy to the invariant
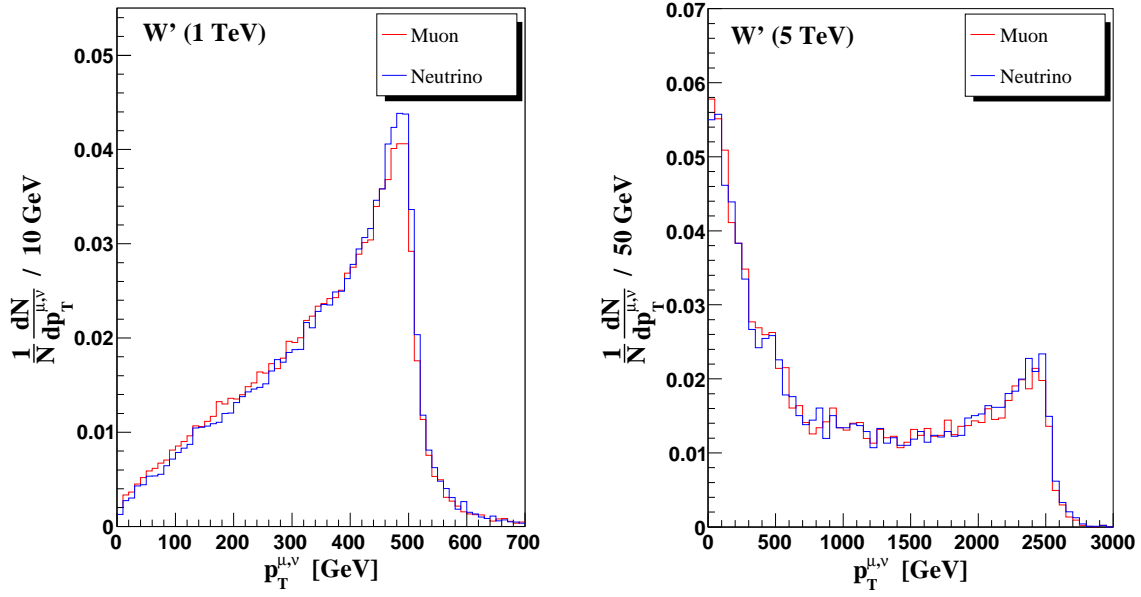
Figure 6.5: *Transverse momentum distribution of the muon and the neutrino arising from a 1 TeV (left) and a 5 TeV W'(right). The clear Jacobian peak is visible at $p_{\mathrm{T}} = M_{W'}$, despite the off-shell fraction of the 5 TeV W'.*
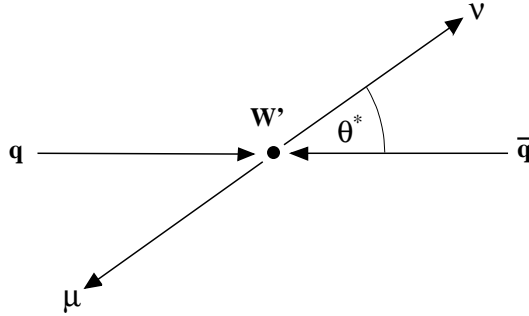
Figure 6.6: *Schematic view of the process $q\bar{q} \rightarrow W' \rightarrow \mu\nu$ in the rest frame of the reaction.*

mass also the transverse invariant mass can be defined as a four-vector product of the two decay products using only the transverse components

$$M_{\mathrm{T}}^2 = (p_{\mathrm{T}_\mu} + p_{\mathrm{T}_\nu})^2 \qquad \text{using} \qquad p_{\mathrm{T}_\mu} = \begin{pmatrix} E_{\mathrm{T}} \\ \vec{p}_{\mathrm{T}} \end{pmatrix}, \quad E_{\mathrm{T}} = E \cdot \sin\theta. \qquad (6.5)$$

For an estimate of the transverse mass distribution one can investigate the process at leading order as shown in figure 3.1, assuming a W' production at rest. Then the muon and neutrino carry the same transverse momentum $p_{\mathrm{T}_\mu} = p_{\mathrm{T}_\nu} \leq M_{W'}$ and travel in opposite directions, $\Delta\phi_{\mu\nu} = \pi$. Inserting these values into the above formula results in

$$M_{\mathrm{T}} = 2p_{\mathrm{T}_\mu} \leq M_{W'}. \qquad (6.6)$$

Thus, the transverse mass distribution (see figure 6.7) shows a Jacobian peak at the mass of the W' similar to the muon p_{T}-distribution (compare with figure 6.5). The advantage
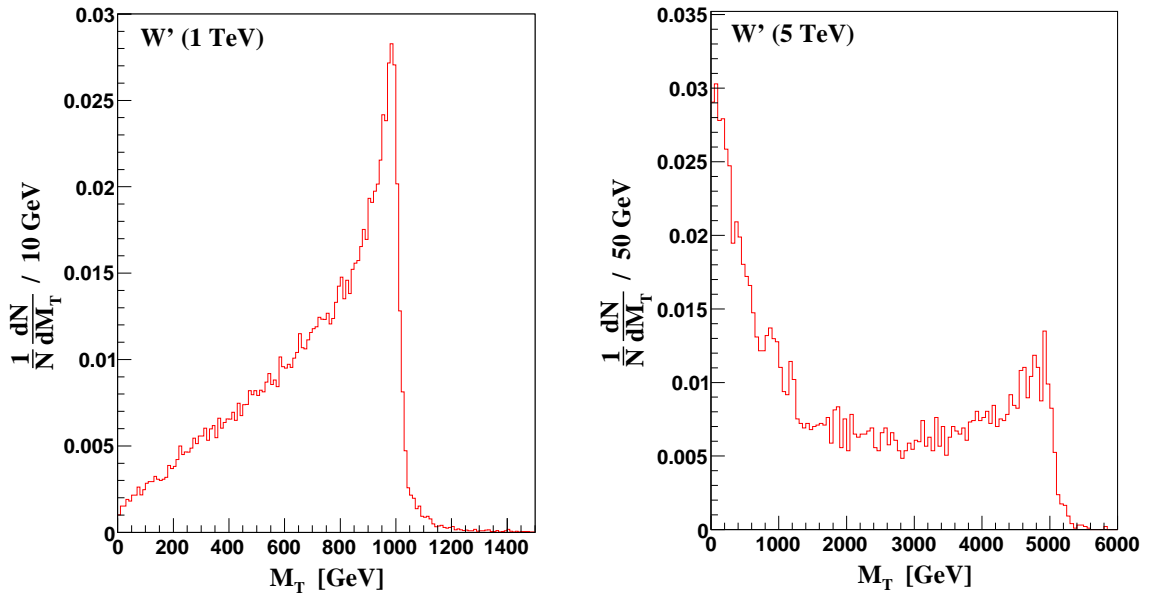
Figure 6.7: *Transverse invariant mass distribution for a 1 and 5 TeV W'. Both graphs show a Jacobian peak at the nominal mass. Due to the off-shell production of 5 TeV W' bosons the right plot has a large fraction of events at low masses (< 2 TeV).*

of using this variable compared to the transverse momentum of the muon is not obvious: since additional information from the neutrino is included the transverse mass is less sensitive to the transverse momentum of the W' boson: for small W' momenta p_T^W the transverse momenta of the leptons in the laboratory and centre of mass frame can be related approximately by Galilean transformations:

$$p_{\text{T}\mu} = p^* + \frac{1}{2}p_\text{T}^{W'}, \tag{6.7}$$

$$p_{\text{T}\nu} = -p^* + \frac{1}{2}p_\text{T}^{W'}. \tag{6.8}$$

Inserting this into the transverse invariant mass 6.4, the equation stays invariant in the first order of p_T^W.

The transverse invariant mass combines all kinematic information of the W' , which are available at hadron colliders via its decay products. Because of the weaker dependence of the invariant mass on the W' transverse momentum, compared to the transverse momentum of the muon, it is a suitable variable for the separation of W' signal events and events with the same signature (background). Therefore it has been chosen as final variable for the full detector simulation study, which is presented in the following chapters.

6.2.3   Angular Distribution

In the rest frame the angular distribution of the muon and the neutrino is given by the V-A structure of the interaction. For the polar coordinate θ^* this would result in a distribution $\sim (1+\cos\theta^*)^2$ and a uniform distribution in the ϕ-coordinate. Due to the large longitudinal momenta of the W' the muon and the neutrino are boosted along the z-direction. This changes the polar angle, but the azimuthal angle remains unaffected.

The change of the flight direction due to the boost is also dependent on the W' mass. A muon arising from a 5 TeV W' with a $p_T{}^\mu = 2$ TeV is less modified by a boost along the z-direction than a 1 TeV W' muon with an $p_T{}^\mu$ of a few 100 GeV. For the θ-distribution of the 1 TeV W' bosons this is less important since these W' bosons are produced within the Breit-Wigner resonance at one mass. But for the 5 TeV W' the mass is spread over a large range and thus leads to a mixture of θ-distributions from W' bosons with different masses.
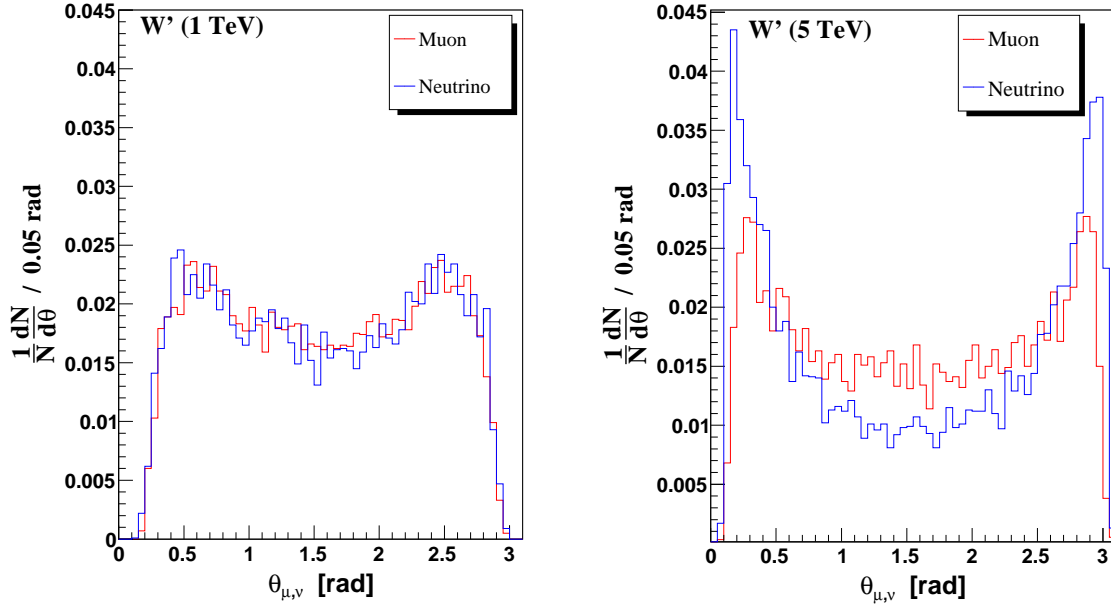
Figure 6.8: *Polar angle distribution for muons and neutrinos arising from 1 and 5 TeV W′ bosons. The angular distribution is given by the V-A structure of the decay, boosts and final-state radiation.*
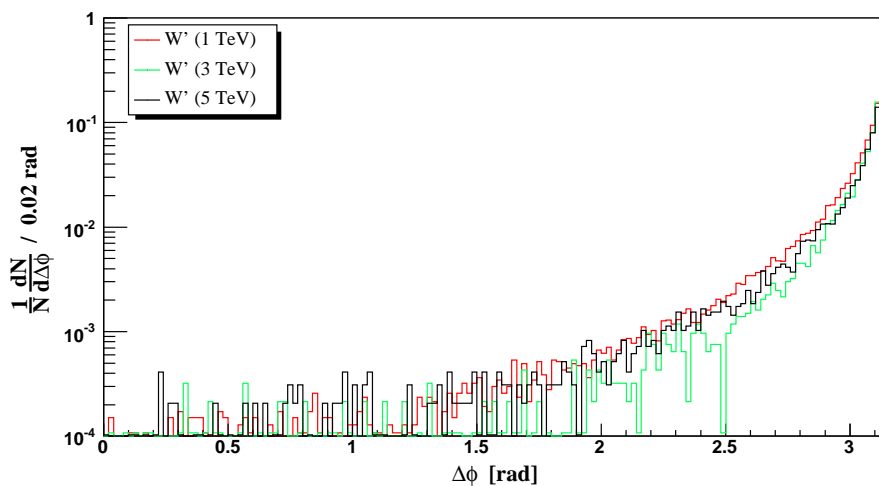
Figure 6.9: *Angular difference of the muon and the neutrino in the transverse plane for different W′ samples. In difference to the polar angle the azimuthal angle stays invariant under boosts along the z-axis.*

Due to the numerous effects the $(1+\cos\theta^*)^2$ angular distribution in the rest frame is not comparable to the one obtained in the laboratory frame as displayed in figure 6.8. Since the azimuthal angle stays invariant under longitudinal boost the uniform distribution from the rest frame is kept.

Although the polar angle distribution of the muons and the neutrinos are different from the ones in the rest frame, the difference angle between the muon and the neutrino in the transverse plane is mainly unaffected. Both particles are emitted back-to-back in the rest frame. Thus, the ϕ-angle difference in the plane perpendicular to the beam is 180°. Since the ϕ angle stays invariant under boosts along the beam line, deviations are only caused by a transverse momentum of the W' or final state radiation of the muon.

In figure 6.9 the ϕ-angle difference is plotted for various W' samples. Since the muons and neutrinos arising from a 3 TeV W' have on average larger momenta than the 1 TeV ones, they are less affected by transverse boson momenta and final state radiation and therefore stay back-to-back to a higher rate. For the 5 TeV W' bosons the effect is again smeared out due to the off-shell production.

Chapter 7

Reconstruction Performance in CMS

In this chapter the expected reconstruction performance for muons, but also for transverse missing energy, especially for the decays $W \to \mu\nu$ and $W' \to \mu\nu$, is presented. Quality plots obtained from the full detector simulation compared with the generator input reflect the present status of the CMS reconstruction software.

Since a complete review of the reconstruction and the corresponding framework is out scope for this thesis, only the performance of the global muon and missing energy reconstruction is presented. For a detailed description of the reconstruction see [67–69].

7.1 Muon Reconstruction

The CMS reconstruction software (ORCA) performs muon reconstruction in the muon system and the silicon tracker. The software is based on the principle of a regional reconstruction in order to allow its use in both, offline and high-level trigger (HLT) system reconstruction.

In principle the reconstruction of a muon is based on the following steps:

- local muon reconstruction (local pattern recognition),

- stand-alone muon reconstruction (using only the muon system, no tracker),

- global muon reconstruction (including tracker).

The first step is the local reconstruction of hits within the muons system components. These hits are used to reconstruct linear track segments in each DT and CSC chamber. In the following a so called stand-alone reconstruction is performed, combining these track segments to a muon track using only measurements from the muon system including RPC measurements. Finally, the reconstructed stand-alone muon is upgraded to an global reconstructed muon by adding matching tracker hits and performing a refit.

7.1.1 Muon Reconstruction Performance

Figure 7.1 shows the relative fraction of muons which pass the level-1 muon trigger as a function of $|\eta|$ for muons' transverse momenta of $p_T = 50$ GeV and $p_T = 500$ GeV. It states, which percentage of the muons, flying into a certain η-region at generator level,

are reconstructed at hardware level (level-1) and pass the level-1 trigger, i.e. enter the high-level trigger selection. Only muons, which pass the level-1 trigger can be further investigated for interesting physics, while all other muons remain undetected.
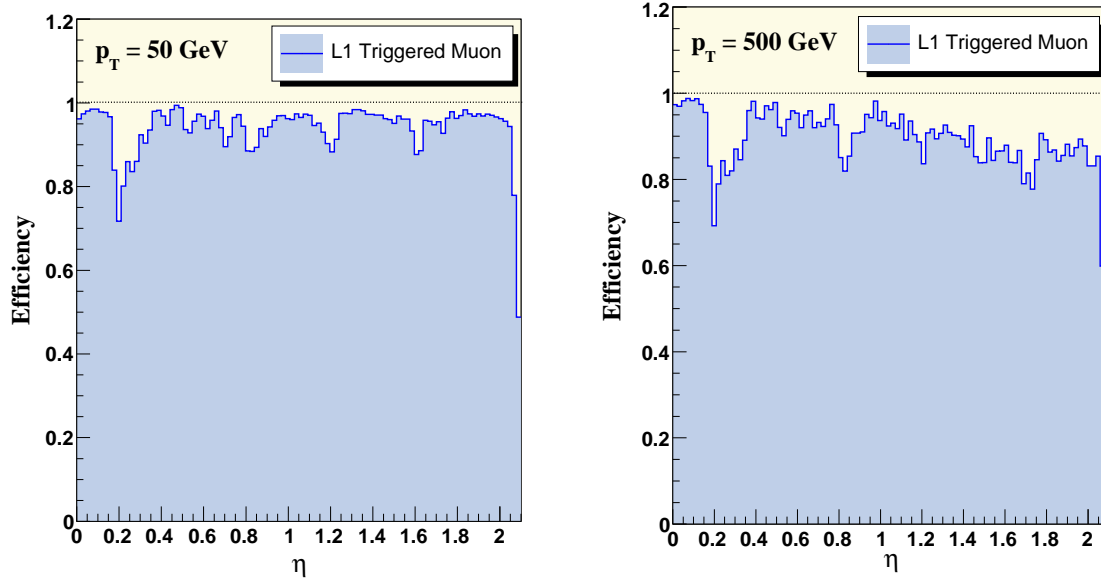
Figure 7.1: *Fraction of muons with a transverse momentum of $p_T = 50$ GeV (left) and $p_T = 500$ GeV, which pass the level-1 trigger as function of the pseudorapidity $|\eta|$.*

As shown in figure 7.1 muons are reconstructed at hardware level typically with an efficiency of 90–95% and also pass the level-1 trigger, whose decision is based on this reconstruction. Except in regions where the muon traverses cracks in the detector geometry and therefore less hits are available for the track reconstruction, the efficiency drops. This effect is visible in the transition regions between the CMS wheels at $|\eta| = 0.25$ and 0.75 and around $|\eta| = 1.2$, where the DT and CSC system overlaps.

In general the efficiency for muons with lower transverse momenta (~ 100 GeV) is larger. This arises naturally since high energetic muons have a less bended track and radiate bremsstrahlung, which gives rise to a multiplicity of hits (electromagnetic showers) like shown in figure 7.5. The reconstruction of a muon track within such a shower is challenging.

Another effect which has to be taken into account, is the fact, that muons with a fixed p_T, but different η, have different energies. At large $|\eta|$ the muons have energies above 1 TeV. Therefore the efficiencies at large $|\eta|$-values are naturally smaller (see right plot of figure 7.1).

7.1.2 Momentum Resolution

Figure 7.2 displays the muon transverse momentum resolution as a function of the transverse momentum in the range 10 GeV $\leq p_T \leq 3000$ GeV . The muons have been taken from the $W \to \mu\nu$ and $W' \to \mu\nu$ samples using muons within the barrel region ($|\eta| \leq 0.2$).

The plot has been obtained from the fit of the $(1/p_{T,rec})$ - $(1/p_{T,gen})$ distribution for different small $p_{T,gen}$-ranges with a Gaussian. The resulting width of the Gaussian fit is divided by the mean of the small $p_{T,gen}$-range and drawn into the graph.
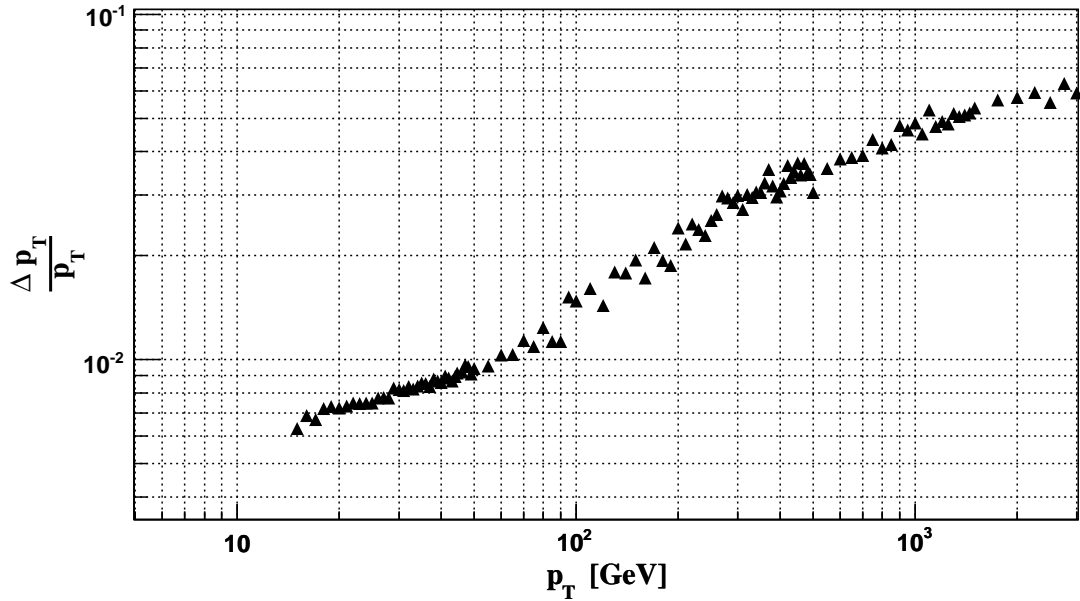
Figure 7.2: *Muon transverse momentum resolution as a function of the transverse momentum for barrel muons ($|\eta| \leq 0.2$).*

The momentum resolution plot (figure 7.2) shows two different ranges. For p_T-values below 100 GeV the resolution is given by the tracker resolution (due to multiple scattering effects in the return yoke). For larger p_T-values the momentum resolution is mainly given by the muon system. Since both detector components have different resolutions the slope is different.

7.1.3   Angular Resolution

Similar to the momentum resolution the angular resolution for the azimuthal angle ϕ and the pseudorapidity η can be calculated by fitting Gaussians to $\phi_{\mathrm{rec}} - \phi_{\mathrm{gen}}$ and $\eta_{\mathrm{rec}} - \eta_{\mathrm{gen}}$.

The angular resolutions are plotted for various muon momenta in figure 7.3. The azimuthal resolution for transverse momenta above 50 GeV is almost constant in η. Also the pseudorapidity resolution is constant over a large η- and p_T -range. Fluctuations are visible at η-regions, where the muon traverses cracks in the detector geometry (e.g. visible at $|\eta|$ = 0.25).

7.1.4   Ghost Muons

During this study it turned out, that some of the muons, especially the high energetic ones, are reconstructed twice (see figure 7.4). These so called ghosts tracks are clearly visible in the distribution of the second highest muon p_T in W' events (see figure 7.5).

Since decaying W' bosons should emit only one high energetic muon, the existence of second muons with a p_T larger 500 GeV came as a surprise. An investigation of the angular differences $\Delta\phi$ and $\Delta\eta$ between the muon "pairs" shows, that both muons fly in the same direction, i.e. $\Delta\phi \approx 0$ and $\Delta\eta \approx 0$ (see figure 7.6).
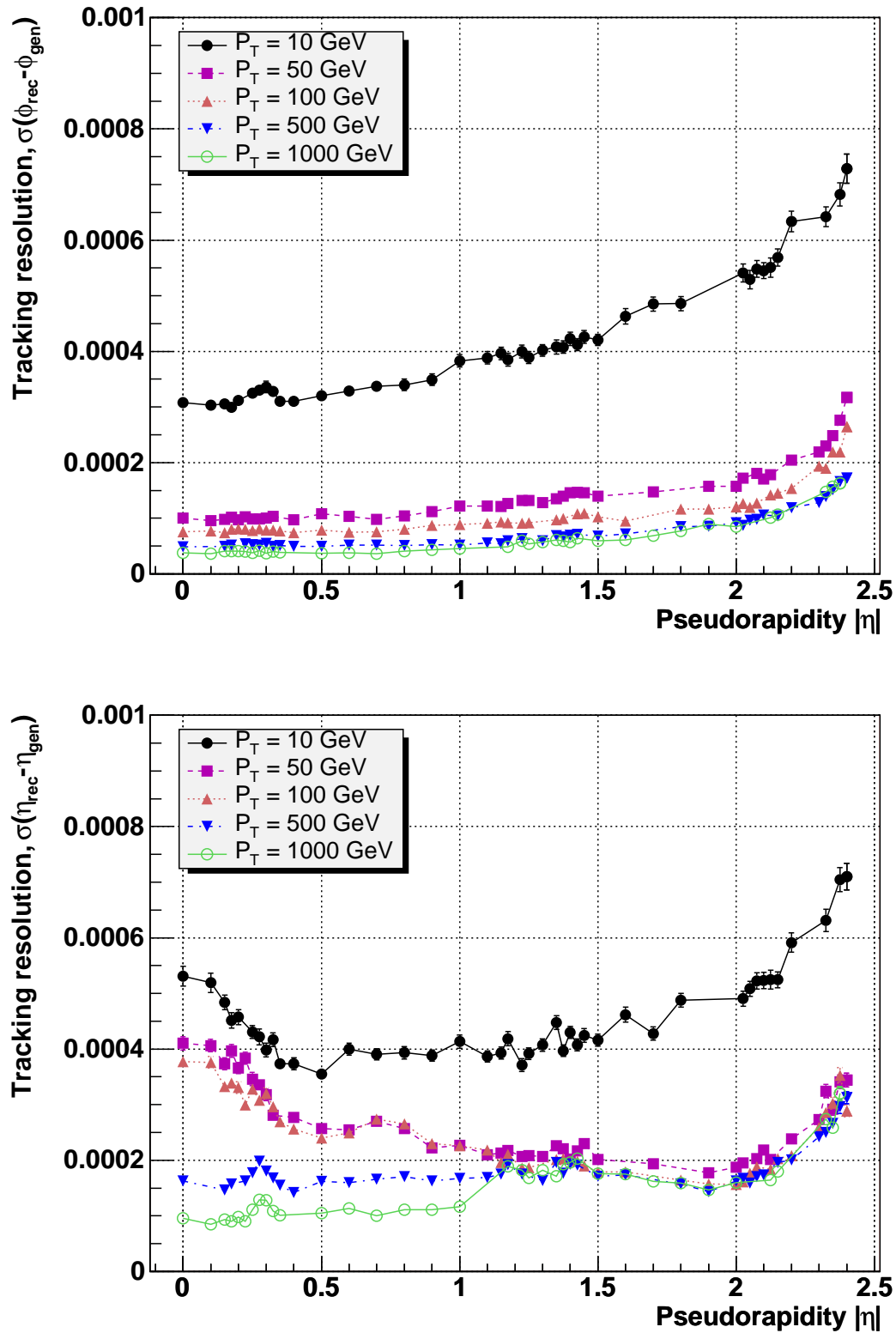
Figure 7.3: *Azimuthal (top) and pseudorapidity resolution (bottom) for various muon transverse momenta using the global muon reconstructor [67].*
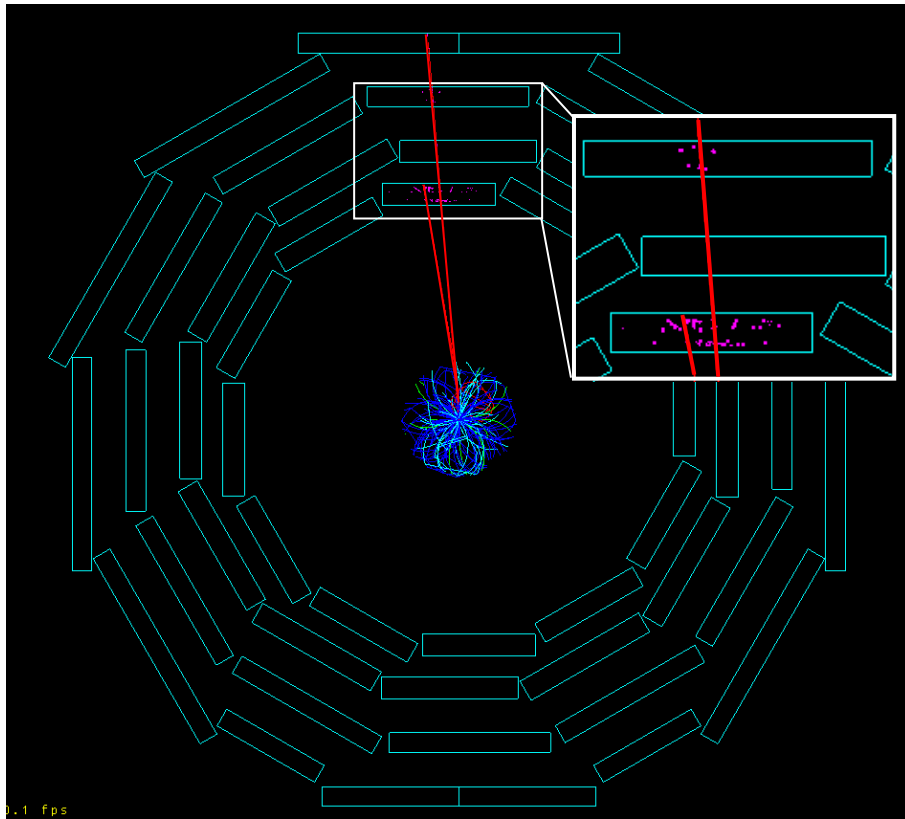
Figure 7.4: *Event display of a ghost muon. Due to the electromagnetic shower the muon is reconstructed twice.*
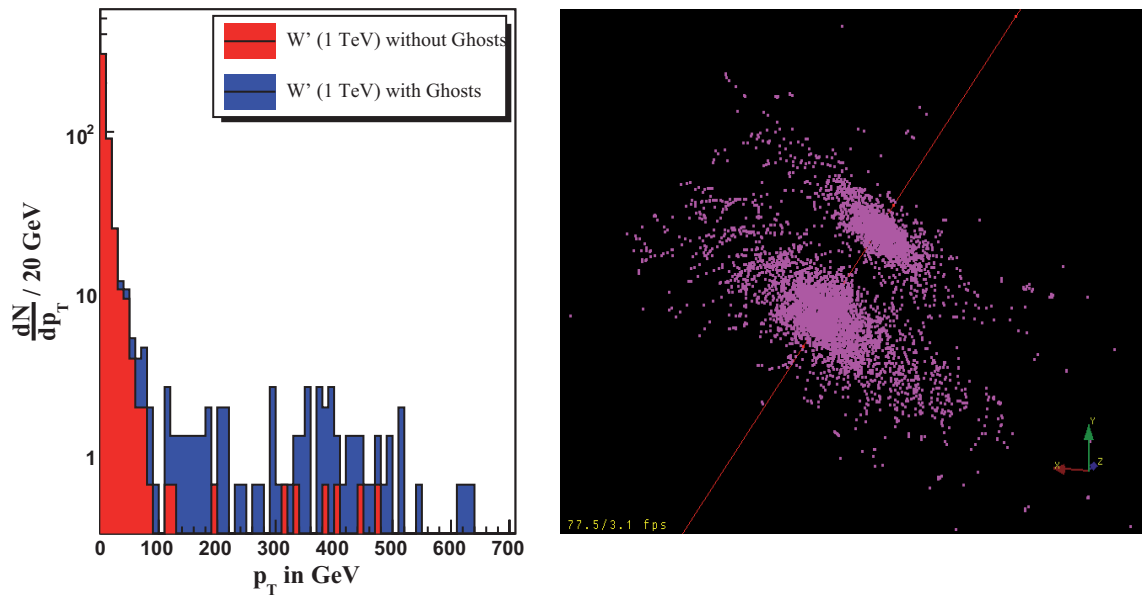
Figure 7.5: *The left plot shows the p_T-distribution of the second highest energetic muon in an 1 TeV W' event, before (blue) and after (red) ghost suppression. An electromagnetic shower within the muon system (right) can be one reason for the existence of a ghost (plot generated using* IGUANACMS*).*
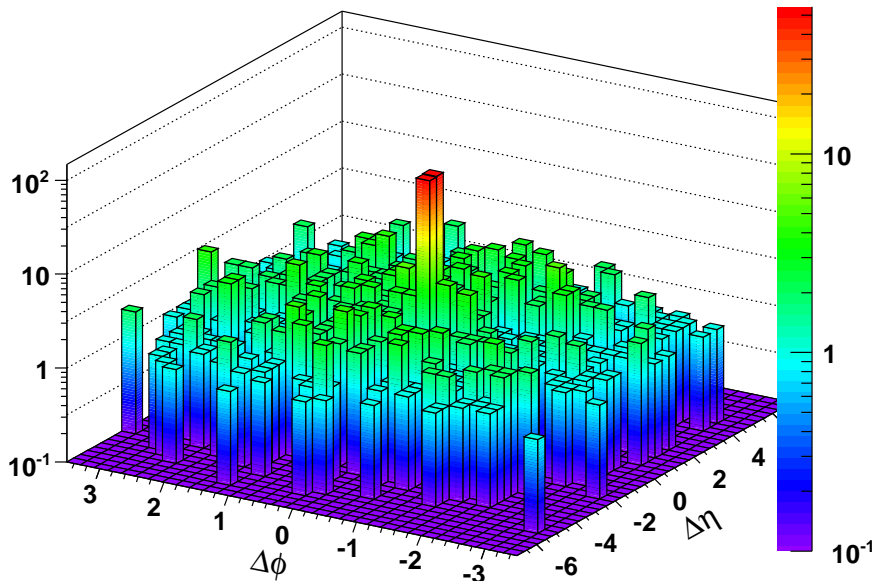
Figure 7.6: *3D-plot of the angular difference $\Delta\phi$ vs $\Delta\eta$ of the doubly reconstructed muons. The distribution strongly peaks at (0,0), i.e. both muons fly in the identical direction.*

The origin of the ghost events is a poor seed generator algorithm, which is particularly weak in the overlap region. Often the seed generator finds more than one seed, e.g. one from the DTs and an other from the CSCs. So the standalone algorithm, which creates a muon track using only informations from the muon system starts from two seeds, and, in these events, actually finds two muons. These muons are typically rather well separated, so they are not considered ghosts and survive the ORCA ghost suppression [70].

Since a better seed generator can not be implemented in a reasonable time scale, a protection to cope with this kind of problems has been included in the latest ORCA version.

To perform the global muon reconstruction the CMS software starts from each seed given by the standalone muon reconstructor separately (which are at least two in the case of ghost tracks). A ghost suppression (based on shared hits) is only performed within the candidates found starting from a given seed. But a ghost suppression looking for shared hits in different seeds is not performed, only softer criteria based on $\Delta\eta$, $\Delta\phi$ and Δp_{T} are tested.

A possible solution which has been implemented is based on the application of the ghost suppression on shared hits on all the global reconstructed muons and not only limited to those coming from the same seed.

First results show an significant improvement: more than 90% of the ghost tracks vanish [70]. However, the inclusion of this fix is out of scope for this thesis. Here a practical approach using a cone algorithm to identify these events has been implemented (see 8.3.1).

7.2   TeV-Muons

High energetic muons behave different compared to low energetic ones. While at low energies muons are minimum ionizing particles, muons with energies in the TeV-regime lose a significant amount of energy as bremsstrahlung. Studies within CMS show, that 1 TeV muons lose on average about 40% of their energy by bremsstrahlung [71]. This results in electromagnetic showers within the muon system and complicates the muon reconstruction due to the multiplicity of hits. A simulated shower (OSCAR) arising from the muon bremsstrahlung within the DT system is shown in figure 7.5.

For the time being, the CMS reconstruction software only contains one global muon reconstructor (GMR) for the reconstruction of muons in every energy regime. Dedicated studies have been started to investigate the speciality of TeV-muons and two algorithms have been implemented based on the already existing global muon reconstructor. Before entering the reconstruction framework ORCA the muon PRS[1] group wants to combine the advantages of all three algorithms in one reconstructor.

The principle of the global muon reconstructor is explained in detail in the appendix B.1.3. Here the principles of the special TeV-muon algorithms, the picky muon reconstructor and the truncated muon reconstructor, are presented.

Picky Muon Reconstructor

Since the global muon reconstructor is vulnerable to muon bremsstrahlung the picky muon algorithm [72] excludes muon detector components, which appear to contain an electromagnetic shower. The algorithm starts with the investigation of all muon detector components, which contain a reconstructed track segment used for the reconstruction of the global muon track. Each component, containing more than a fixed number of track segments is flagged as contaminated (default: one track segment per CSC, DT and one hit per RPC).

To avoid the exclusion of a good measurement the contaminated parts are not directly excluded from the track fit. Before, the χ^2 of each hit with respect to the global reconstructed track is calculated. If the χ^2 is larger than a threshold (default DT: 10, CSC: 25, RPC: 1) the contaminated detector is excluded. Also non-contaminated parts are excluded if the χ^2 is larger than 200.

With the remaining track segments the muon track is refitted. As an result one obtains a picky muon.

Truncated Muon Reconstructor

The truncated muon reconstructor algorithm compares two different track fits and chooses the best one [73]. In difference to the global muon reconstructor the truncated reconstructor uses a reduced set of information. The reconstructor compares the "tracker only" muon track with a "tracker plus first muon station" track ("truncated" track). To decide which track to choose, the χ^2-value and the degrees of freedom used for the fit are compared.

Since the algorithm is restricted to the tracker and the first muon station, it is less sensitive to electromagnetic showers originating from muon bremsstrahlung within the

---

[1]**P**hysics, **S**imulation and **R**econstruction

DT/CSC system. Also multiple scattering of the muon in the iron return yoke has no influence on this algorithm.

Comparison of the different Reconstructors

Figure 7.7 shows the resolution of all three reconstructors (global, picky and truncated muon reconstructor). In the left plot the Gaussian part of the resolution is shown, while the right plot represents the "non-Gaussian tails".
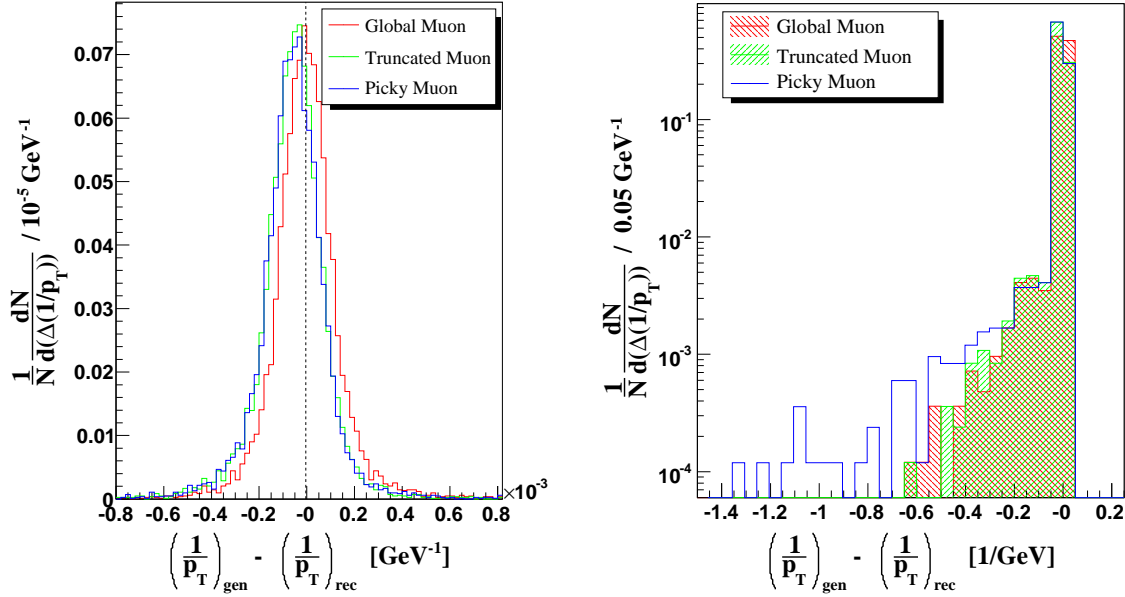
Figure 7.7: *Comparison of the three muon reconstructors. The left plot shows the Gaussian part of the resolution plot, while the right zooms into the non-Gaussian tail.*

On average the truncated and picky muons are reconstructed with too less energy. Since the non-Gaussian tails of the TeV-reconstructors are more significant (picky) or nearly identical (truncated) compared to the global muon reconstructor, the decision has been taken to use the default global muon reconstructor in this analysis.

7.3   Transverse Missing Energy

The missing transverse energy within the detector is given by the calorimeter (ECAL + HCAL) deposits and by the transverse momentum carried away by the muons, since they are not stopped within the calorimeter.

Therefore the missing transverse energy is calculated by summing up all energy deposits $\not{E}_x$, $\not{E}_y$ in the calorimeter towers (ECAL + HCAL) separately for the x and y direction, while weighting the single towers according to their angular direction seen from the vertex. Since the muons deposit only a small fraction of their energy within the calorimeter, the energy imbalance caused by the muons has to be corrected. To do this the momentum components in the x and y direction for each muon in the event are subtracted from the calorimeter deposits in x and y direction. From the obtained missing energy in x and y
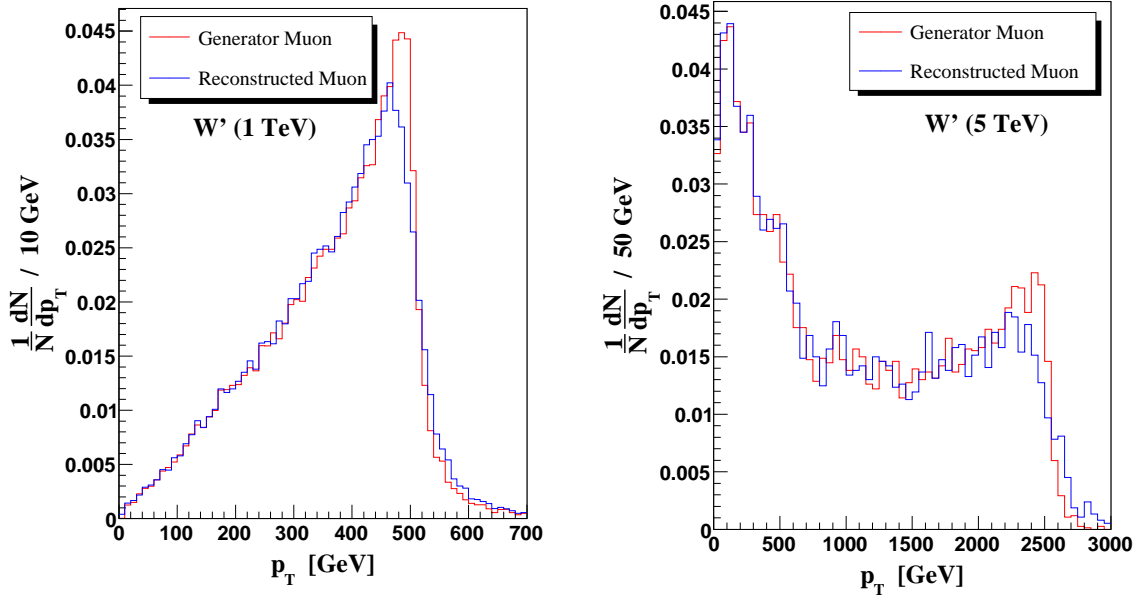
Figure 7.8: *Comparison of the three muon reconstructors. The reconstructed and generated p_T -distributions for two W' masses are shown.*
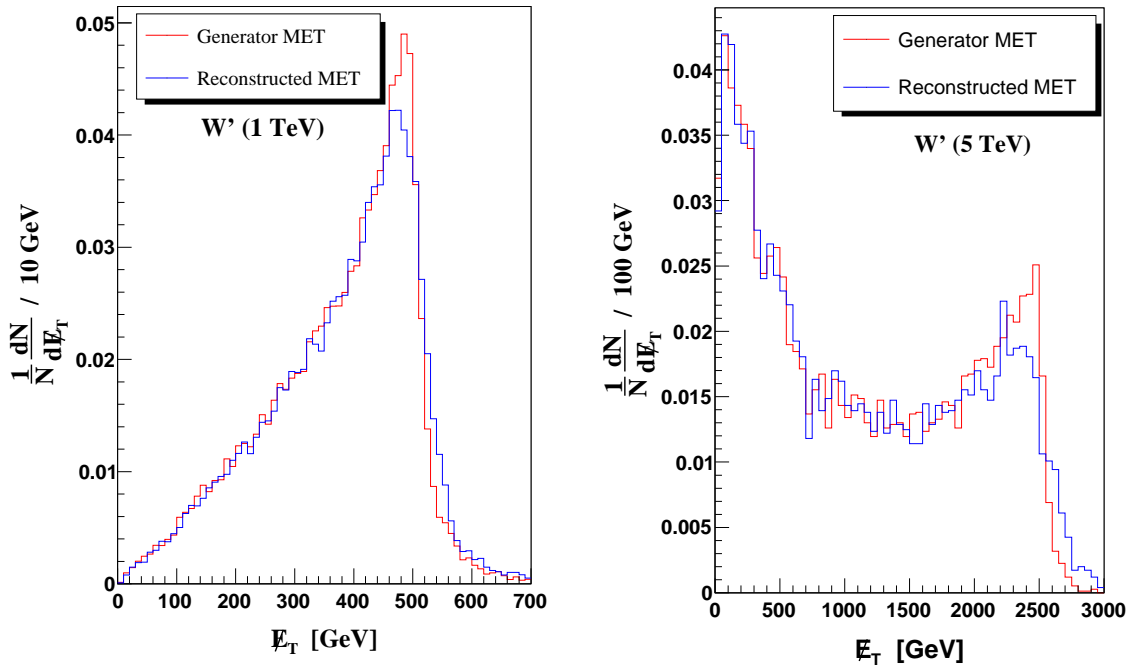
Figure 7.9: *Missing transverse energy distribution at generator and reconstruction level for a 1 and 5 TeV W'.*

direction, the missing transverse energy $\not{E}_T$ as well as the angular ϕ in the transverse plane are calculated

$$\not{E}_T = \sqrt{\not{E}_x^2 + \not{E}_y^2} \qquad \text{and} \qquad \tan\phi = \frac{\not{E}_y}{\not{E}_x}. \tag{7.1}$$

Figure 7.9 displays the missing energy distribution of the 1 and 5 TeV W'. For the signal also the missing transverse energy obtained at generator level is included in the plot. It is not identical with the generator neutrino p_T, but is calculated by adding up all transverse momenta of the generator particles flying within $|\eta| < 5$ except the neutrinos. The obtained value is the p_T-imbalance of the detector. Thus the sign of this value has to be changed to get the missing energy. The η-cut is performed to take the calorimeter acceptance into account. The missing energy calculated in that way is the best which can be achieved with CMS.

A comparison of the transverse missing energy distributions with the corresponding transverse muon momentum distributions shows a remarkable coincidence. For muon energies relevant within this study the missing energy is not determined by the calorimeter deposits, but by the muon momentum. Therefore also the missing energy resolution is mainly given by the muon resolution.

Chapter 8

Event Selection

The goal of this study, performed with the full CMS detector simulation including pile-up, is the investigation of the observability of a potentially existing new heavy charged gauge boson W' decaying into a muon and a neutrino. To extract a clear W' signal, hidden by Standard Model background, selection criteria are applied to the simulated data. The selection process results in a final variable with an improved signal to background ratio. As motivated in chapter 6, the variable, from which the observation significance is determined is chosen to be the transverse invariant mass. In figure 8.1 the final variable for signal and background is shown before applying any cuts.

In this chapter, both, the simulated signal and the simulated Standard Model background are presented as well as the cuts used to enrich the relative signal contribution within the final variable[1].

8.1 Data Samples and Cross Sections

8.1.1 The Signal

To judge which Standard Model processes occur as background in a $W' \rightarrow \mu\nu$ search, the characteristic signature of such a process has to be understood. Since the W' is a massive object it is likely to be produced without transverse momentum. The decay energy of the W' is shared among the muon and the neutrino which are emitted back-to-back in the W' rest frame carrying a large momentum (an example is shown in figure 8.2). Due to boosts the angle between the muon and the neutrino is different from $180°$ in the laboratory system. However, the angle in the transverse plane stays invariant under boosts along the z-axis. Since the neutrino is only visible as missing energy in the transverse plane, the kinematical analysis is restricted to this plane.

Beside the muon and the missing transverse energy, only the beam remnants[2], which mostly vanish through the beam pipe, result from the production and a subsequent decay

---

[1]In most of the shown plots the signal is *not* added to the background. This so called "nonstacked" drawing of the signal has the advantage, that the signal shape is clearly visible and one can directly estimate if the signal is visible within in the background or not. In addition it has the advantage, that more than one signal (i.e. for different W' masses) can be drawn in one histogram together with the background.

[2]The colour charged proton fractions from which the W' creating quarks originate.
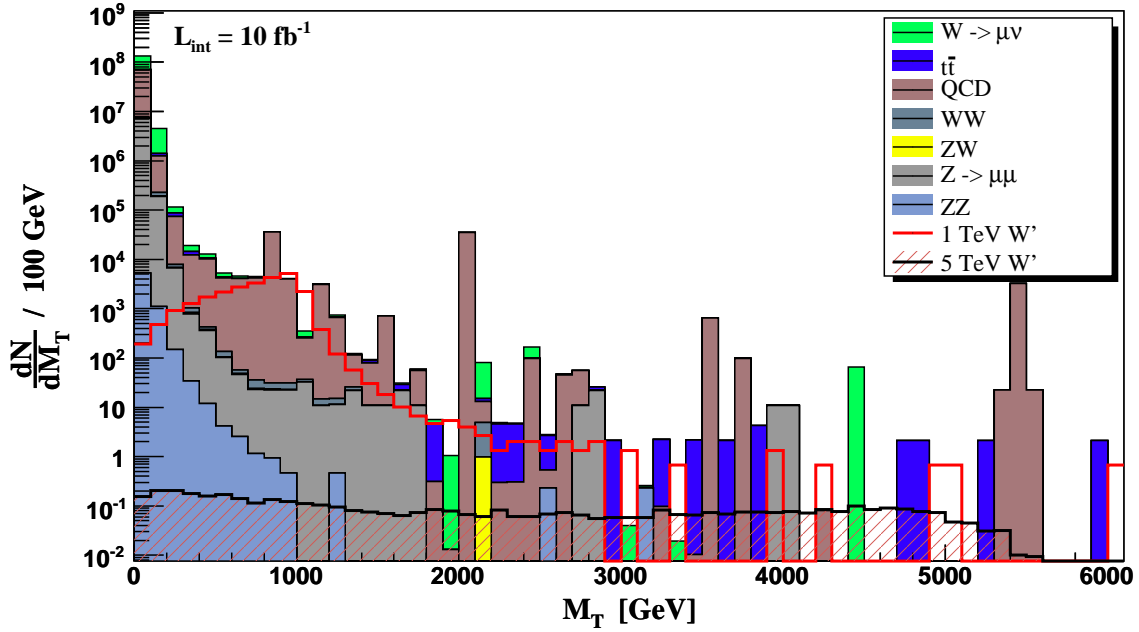
Figure 8.1: *Distribution of the transverse invariant mass without applying any cuts for the signal and SM background. The 1 and 5 TeV W' signal (not stacked) and the background (stacked) for an integrated luminosity of 10 fb^{-1} are drawn. For each event the highest energetic muon and the missing transverse energy are combined to the transverse invariant mass. Over the whole range the background (mainly QCD) is even larger than the 1 TeV W' signal.*

of a $W' \to \mu\nu$. Additional particles which might be observed, originate from initial and final state radiation and pile-up. Therefore a $W' \to \mu\nu$ event has the "clean" signature of a high energetic isolated muon, together with a large amount of missing energy pointing into the opposite direction in the transverse detector plane. Due to the small transverse momentum of the W', the transverse momentum of the muon and the missing transverse energy are of similar magnitude.

Since no official MC simulated W' sample exists in the CMS collaboration, the signal data samples have been generated in a "private" production using shell scripts developed in Aachen. A full event simulation including an average of 3.5 pile-up events per signal event, corresponding to the low LHC luminosity phase ($\mathcal{L} = 2 \cdot 10^{33}$ cm^{-2} s^{-1}), has been performed as described in chapter 5.

As input to the full detector simulation W' events based on Altarelli's Reference Model (see chapter 3.3) have been generated using PYTHIA (version 6.227). The only parameter within this model is the mass of the W'. Therefore several samples with various W' masses have been produced with the full detector simulation.

Since the current lower mass bound on the W' is slightly below 1 TeV the first sample is generated with this mass. Further samples follow with masses of 2–8 TeV, since masses of ~ 7 TeV are the kinematical limit reachable with the LHC centre of mass energy of 14 TeV. During the study the mass, up to which a possible existing W' can be discovered with an integrated luminosity of 10 fb^{-1}, turned out to be between 3 and 5 TeV and further samples in this region with mass steps of 100 GeV have been simulated.
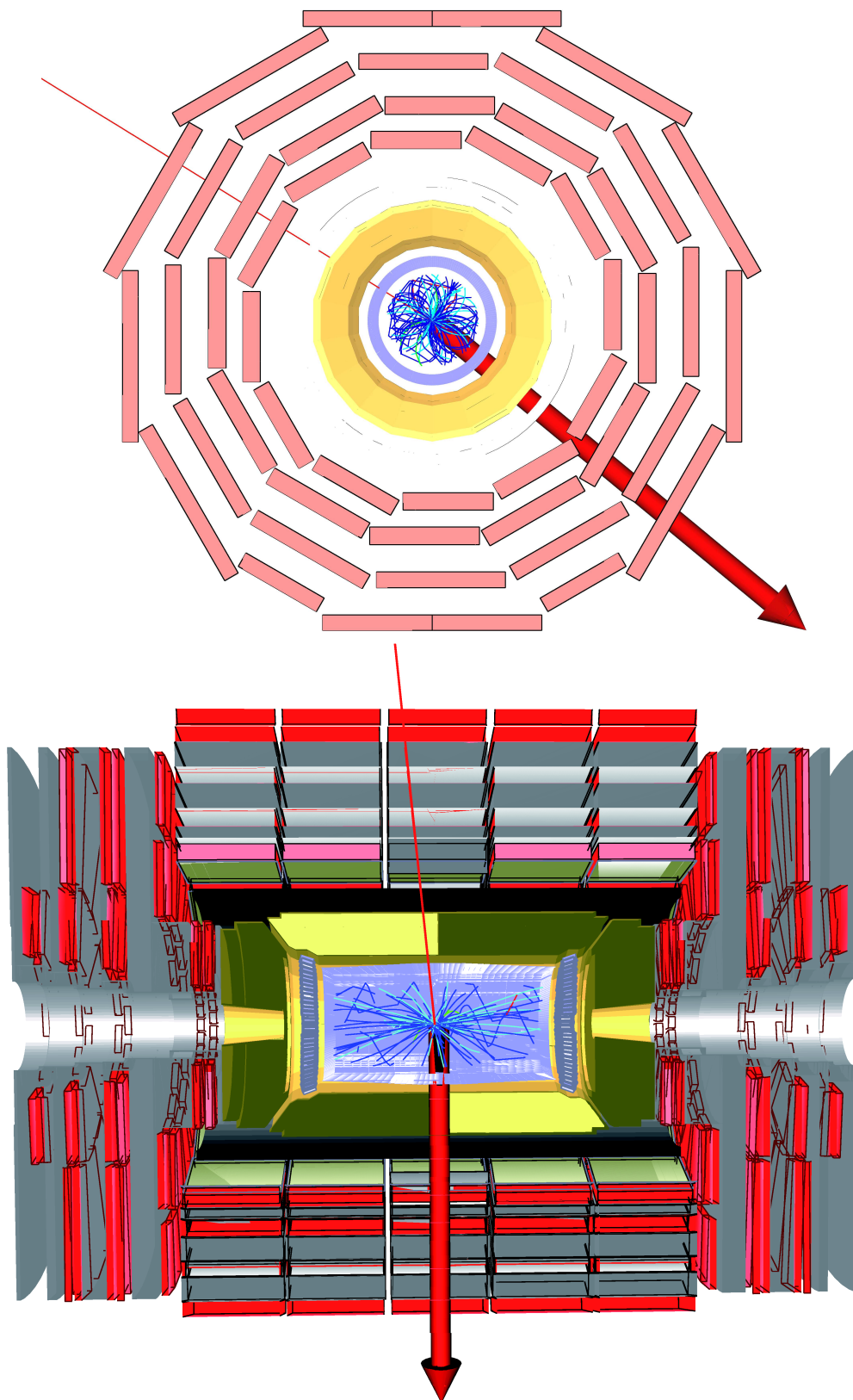
Figure 8.2: *A 1 TeV W′ displayed by the CMS event display* IGUANACMS. *In the transverse (top) and longitudinal plane (bottom) the muon (thin red line) and the missing transverse energy (thick arrow) are shown. Further tracks are visible in the tracker.*
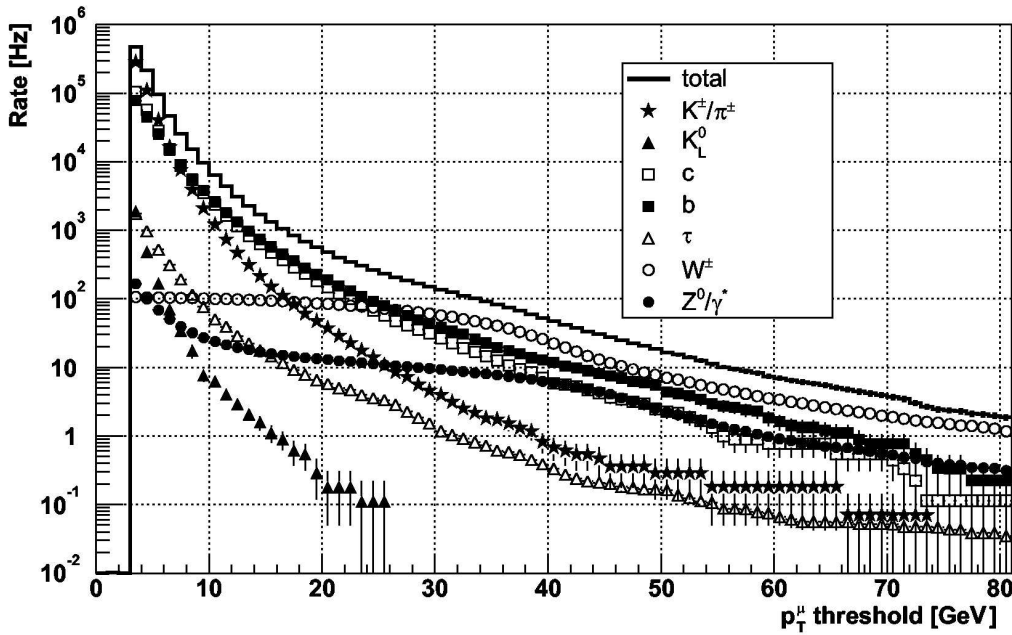
Figure 8.3: *Inclusive single muon production rate as a function of the muon p_T-threshold at the LHC with a luminosity of $\mathcal{L} = 10^{34}$ cm^{-2} s^{-1}. The plot is generated using PYTHIA with a restricted detector acceptance $|\eta| < 2.1$ [74].*

The cross sections for the main signal samples, obtained from PYTHIA at leading order of the perturbation expansion, are shown in table 8.1 as well as the number of simulated events. The full list is attached in the appendix A.2.

8.1.2 The Background

Relevant backgrounds are qualified by a very similar signature compared to the signal. Since missing transverse energy cannot be measured as precise as a muon, the selection criteria mainly address the muon properties.

From figure 8.3 one obtains that muons with transverse momenta larger than 30 GeV are mostly resulting from the decay of gauge bosons, in particular W. Since the massive charged SM gauge bosons decay in the same manner as the W', they have identical signatures. However, due to the huge mass difference of the W and the W' (> 1 TeV) the transverse momentum of the W-muon and the transverse missing energy originating from the SM W is much smaller.

Other sources of high energetic muons are the decays of heavy quarks. They hadronize and produce among others mesons, which also decay into muons (e.g. b-quarks). Since these muons are accompanied by a jet and thus are not isolated, they can be rather easily identified as background. As a cross check the statement is proved using a general QCD sample (see below) as background, which is likely to contain several non-isolated muons resulting from hadronizing quarks.

Among the quarks the top quark is an exception. Its lifetime is too short to hadronize and, since it decays nearly always into a W and a b-quark, top-antitop events are taken into account for this analysis.

Based on these facts, the considered background has been determined to be

- **single W-production** with a subsequent decay into a muon and a neutrino,

- **single Z^0-production**, decaying into two muons,

- **gauge boson pair production WW, WZ and ZZ,**

- **$t\bar{t}$ pair production,**

- **QCD** (see below).

The analysed data samples with the corresponding cross sections and number of events can be taken from table 8.1. Due to the restricted computing power and the long time which is necessary for the production of one event, the number of simulated events is limited. To reduce the needed computing time already at the generator level (PYTHIA), acceptance cuts are applied. This is mainly important for processes with a large cross section like single W- or Z^0-production, where such constraints save the simulation of several 10^5 events.

For the $W \to \mu\nu$ sample the event is only fully simulated, if the muon has a transverse momentum larger than 14 GeV and penetrates the detector with angles corresponding to $|\eta| < 2.5$. The muons in the $Z^0 \to \mu\mu$ sample are also constrained to $|\eta| < 2.5$ and must have transverse momenta larger than 20 and 10 GeV, respectively, to pass beyond the generator level. The η cuts are foreseen since the muon system only covers an area up to $|\eta| = 2.4$, while the p_T cuts arise from trigger studies.

No constraints are applied to the pair boson samples WW, WZ, ZZ and the $t\bar{t}$ sample. Another approach has been taken for the generation of the so called "QCD"-events. This synonym covers (at leading order) events of the type $qq \to qq$, $q\bar{q} \to q\bar{q}$, $q\bar{q} \to gg$, $qg \to qg$, $gg \to q\bar{q}$ and $gg \to gg$. Since these kind of processes, especially those with a low momentum transfer of the partons, dominate by far at hadron colliders (see figure 4.2), the QCD-events have been produced in various disjunct samples. The events are separately simulated for different values of the transverse momenta $\hat{p}_T$ of the final state partons in their rest frame.

For this study the samples have been analysed separately, scaled according to the cross section and finally merged into one sample. The detailed division of the QCD sample into subsamples is listed in the appendix (see table A.1).

It turned out, that the official background samples do not cover the total range of the signal's transverse invariant mass. Since the $W \to \mu\nu$ dominates the background after performing selection cuts (see below), further W samples have been produced choosing special ranges for the transverse momentum $\hat{p}_T$ of the muon and neutrino in the rest frame of the W. 200 events each have been produced in 50 GeV-steps in the $\hat{p}_T$-range from 200–500 GeV and 100 GeV-steps from 500–3000 GeV.

To obtain a precise cross section for these additional W samples from PYTHIA at generator level, at least 10000 events, have been produced each, which results in a cross section error less than 0.5%. The error on the other signal and background cross sections arising from limited event generation is negligible due to the large number of generated events.

The various additional samples can be easily scaled according their luminosity and merged into one sample, since they have been produced in disjunct $\hat{p}_T$-ranges.

Background			
Type	Cross Section $[fb]$	Analysed Events	Official Sample
$W \to \mu\nu$	$1.72 \cdot 10^7$	1483999	mu03_W1mu
$W \to \mu\nu$	depending on $\widehat{p}_\mathrm{T}$	200 per $\widehat{p}_\mathrm{T}$-range	private
Z^0 inclusive	$1.45 \cdot 10^8$	721712	mu03_DY2mu
WW inclusive	$1.88 \cdot 10^5$	483000	jm03b_WWjets_inclusive
ZZ inclusive	$1.11 \cdot 10^4$	479000	jm03b_ZZjets_inclusive
ZW inclusive	$2.69 \cdot 10^4$	276993	jm03b_ZWjets_inclusive
$t\bar{t}$ inclusive	$4.92 \cdot 10^5$	2299736	jm03b_TTbar_inclusive
QCD	$> 6 \cdot 10^8$	> 2000000	jm03b_qcd_XXX_YYY
Signal			
W' (1 TeV) $\to \mu\nu$	$3.11 \cdot 10^3$	46595	private
W' (2 TeV) $\to \mu\nu$	$1.58 \cdot 10^2$	8884	private
W' (3 TeV) $\to \mu\nu$	$1.82 \cdot 10^1$	9301	private
W' (4 TeV) $\to \mu\nu$	$2.87 \cdot 10^0$	10000	private
W' (5 TeV) $\to \mu\nu$	$6.07 \cdot 10^{-1}$	9707	private
W' (6 TeV) $\to \mu\nu$	$1.90 \cdot 10^{-1}$	5000	private
W' (7 TeV) $\to \mu\nu$	$8.56 \cdot 10^{-2}$	5000	private
W' (8 TeV) $\to \mu\nu$	$4.69 \cdot 10^{-2}$	5000	private

Table 8.1: *The simulated data samples used in this study. The cross section (times branching ratio) obtained from* PYTHIA *at leading order using the parton density function CTEQ 5L (leading order), the number of analysed events (before applying any cuts) as well as the official production name are given (see section 5.1).*

But the official sample, which has been produced without any constraints on $\widehat{p}_\mathrm{T}$, has some "overlap" with the additional produced ones. To avoid "double-counting" of W events the "overlap"-region has to be identified. Within this region a cut has to be applied to make one sample end at the cut, while the other starts at this point.

The merging of the official W sample with the privately simulated W events has been performed using the transverse invariant mass at generator level. The choice of this variable arises naturally. The small samples have been generated by defining a $\widehat{p}_\mathrm{T}$-range and can be merged according to their luminosity. The transverse momentum in the rest frame is directly proportional to the invariant mass ($M_\mathrm{T} = 2\,\widehat{p}_\mathrm{T}$). Since the $\widehat{p}_\mathrm{T}$ cannot be calculated from the data, which have been extracted from the official data, the invariant mass at generator level is used.

This choice is more conservative than using the reconstructed transverse invariant mass, because events which have a larger reconstructed than simulated transverse invariant mass might be sorted out when using the reconstructed invariant mass for the separation. With the separation at generator level this is not the case.

As shown in figure 8.4 both samples are nearly identical in the overlapping transverse mass region and can be connected continuously. Based on this plot the decision has been

taken to use the official W-sample for invariant masses up to 400 GeV, while the samples with restricted $\widehat{p}_T$ values are used starting at this point.

However, the muon p_T-distribution (see figure 8.5) of both samples shows a significant difference. This results from the different way of event generation: high energetic muons from W decays can arise either from heavy offshell W bosons or from boosts in the transverse plane, e.g. due to initial state radiation of a gluon. Since the additional samples with selected $\widehat{p}_T$-ranges only contain events of the first type, the p_T-spectrum has a lack of high-p_T muons arising from a large transverse W momentum. Nevertheless the shape of the muon p_T-distribution is well described.

Since only the first type of events give rise to background, which is well described by the transverse invariant mass, this deficit has no influence on the analysis.
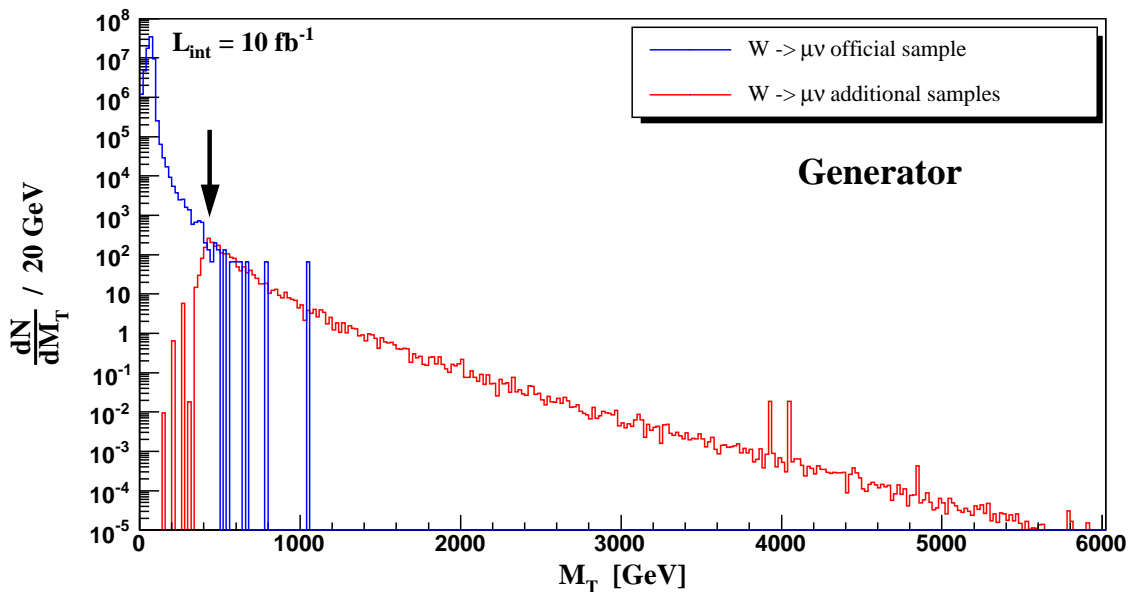
Figure 8.4: *Matching of the different W-samples using the transverse invariant mass at generator level. A smooth transition is possible if the official sample ends at 400 GeV, where the other samples start (see arrow).*

8.2 Preselection of Events

Before starting with the analysis the MC events have to pass preselection criteria, mainly to sort out events which are not accepted by the level-1 trigger. Such events are reconstructed in the full detector simulation by ORCA, but an identical event in a running CMS detector would not be written on tape. For this study it has the side effect, that the preselection reduces the amount of data, which has to be transported using grid services and later locally stored.

The applied preselection criteria ensure the basic commonality of the background and the signal. Events which enter this analysis

- have to contain at least one global reconstructed muon,

- have to pass the level-1 muon trigger ($|\eta| \leq 2.1$)
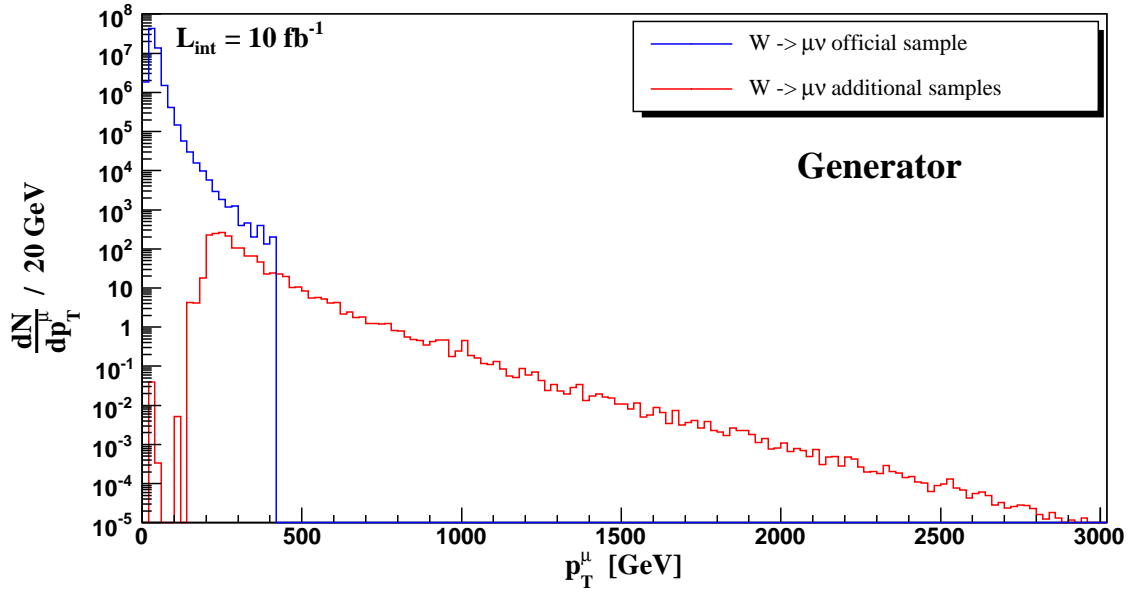
Figure 8.5: *Due to the different generation processes, the muon p_{T}-distribution of the additional samples with high transverse masses show a deficit of high energetic muons.*

- and the high level trigger.

The first criterion naturally arises from the fact, that the signal significance is determined using the transverse invariant mass calculated from the transverse momentum of the muon and missing transverse energy. The use of global reconstructed muons also demands a quality standard for the reconstructed object as shown in chapter 7. The latter two constraints ensure that the event will be recorded by a fully operational CMS detector.

Since the detector simulation uses the start-up detector geometry, the CSCs close to the beam pipe (ME1/1) have only a limited readout. This implicates that the muon trigger is restricted to a range $|\eta| < 2.1$. Therefore the second preselection criterion also limits muons to this region.

The so defined starting sample is now investigated for criteria, which allow a distinction between signal and background. The cuts applied for this purpose are stated and explained in the following.

8.3 Selection Criteria

After the preselection cuts have been applied to the data in order to suppress background and thus to improve the signal to background ratio within the final variable. According to the $W' \to \mu\nu$ signature the following cuts have been applied in this order

- **Muon Quality**
  Since a muon, which is reconstructed only from a few hits or which results from a poor track fit might fake a high energetic muon, cuts are applied to the muons to ensure a high quality reconstruction.

- **Single Muon Requirement**
  In difference to Z bosons, which decay into muons, $W' \to \mu\nu$ events give rise only to a single muon. To suppress the background from neutral gauge bosons, events with more than one muon are excluded from the final variable.

- **Muon Isolation**
  Muons arising from decaying gauge bosons are isolated. An isolation criterion reduces the background from non-isolated muons, which originate within a particle jet (e.g. QCD).

A detailed motivation and explanation of the different cuts are given in the following subsections.

8.3.1 Muon Quality

The rate of low energetic muons arising from different SM backgrounds is of several orders of magnitude larger than the rate of high energetic muons from W' bosons. Assuming that every 10^5th low energetic muon is wrongly reconstructed as a high energetic one, the high-p_{T} muon rate would be dominated by these muons. The observation of a W' signal within this "background" would be impossible.

Therefore a high quality reconstruction of muons in the full transverse momentum range of 5–4000 GeV is essential for the detection of a possible W' at the LHC.

Within this study it has turned out, that the quality of the muons can be improved by demanding criteria, in addition to the ones applied by the reconstruction software. They are based on the number of hits (degree of freedom), which are used for the muon's track fit and the deviation of the muon track from the single hits, namely the χ^2-value of the track fit. In addition an algorithm has been developed to reject ghost tracks, which occur in events where one muon is reconstructed twice.

Degrees of Freedom for the Muon Track

This quality cut takes into account, that the properties of particles which are measured at a multitude of points along a large distance can be determined very precisely. Inverting this statement the properties of a particle measured at only a few points have on average larger errors and might vastly differ from the actual properties. Therefore only muons which are measured at a certain number of points enter the final variable.

This analysis aims for high energetic muons especially with transverse momenta larger than 200 GeV. Due to the high penetration power muons are normally not stopped within the detector.

Under the assumption that the muons pass at least two muon stations, their track should be visible also inside the pixel detector and the silicon tracker. This results in a minimum of 10 measurements inside the inner tracker (2–3 within the pixel detector and at least 7–8 inside the tracker). Adding further track information from two muon stations with their RPCs results in at least 15 overall track measurements. Since these measurements always consist of two coordinates a track fit is constrained by $15 \cdot 2 = 30$ "single" measurements.

In general a track with five parameters (for details see [47]) has to be fitted to the reconstructed track informations. An equation with 5 parameters constrained by 30 measurement results in 25 degrees of freedom for the track fit. This is the minimum number of degrees of freedom required for a muon within this study.
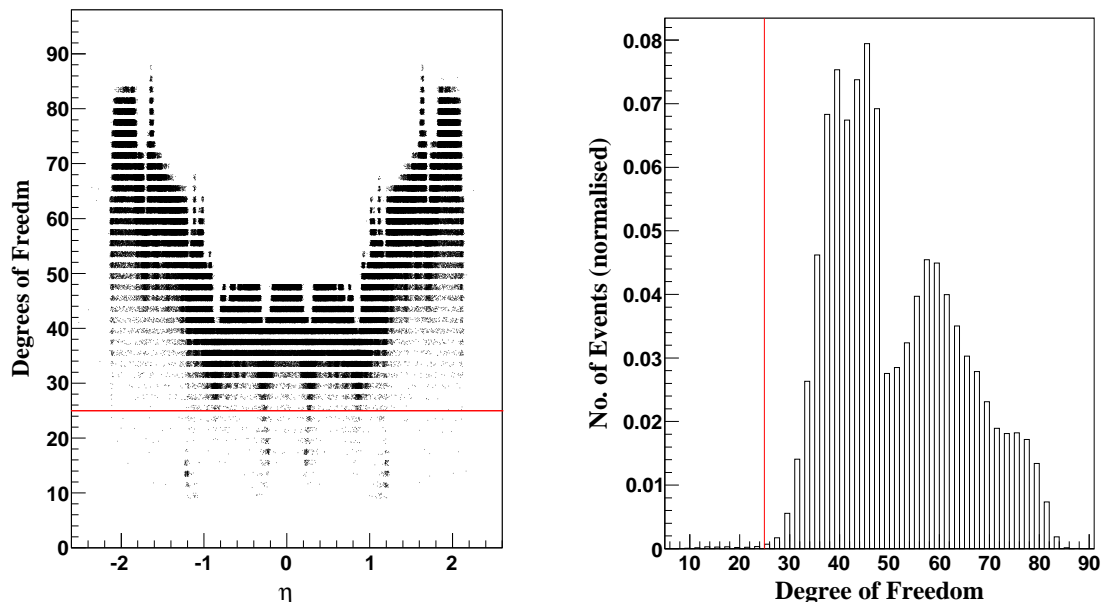
Figure 8.6: *The muon degree of freedom (= number of used measurements minus five fit parameters) as a function of η (left) and the overall distribution (right) are shown for the $W \rightarrow \mu\nu$ sample. All other cuts have been applied.*

Figure 8.6 displays the distribution of the number of degrees of freedom as a function of the pseudorapidity η for the muons in the $W \rightarrow \mu\nu$ sample. The structure of the muon system (barrel wheels and endcap discs) is clearly visible. Especially the transition regions, which are not fully covered by active detector volumes, show cracks in the acceptance. A major part of these muons, which escape through less covered detector areas, are also excluded by this cut. This is a crucial cut since the reconstruction of muons with a small number of measurements is more error-prone and might fake a high-p_T muon. As obtained from figure 8.6 only a small fraction of simulated muons do not pass this quality criterion (compare with table 8.2 and 8.3).

χ^2-Criterion for Muon Track

A high quality track fit through the track measurements obtained from the local muon reconstruction is characterised by a small deviation of the fitted track from the used measurements. The χ^2-value of the fit is a quality criterion for the reconstructed track. However, a small χ^2-value does not guarantee a good fit: a fit through only a few measurements has naturally a smaller χ^2-value than an extrapolation using a larger number of hits. The χ^2 normalised to the degrees of freedom of the muon track remedies this drawback. The value can be interpreted as a kind of mean deviation per measurement and thus provides a reasonable quality measurement.
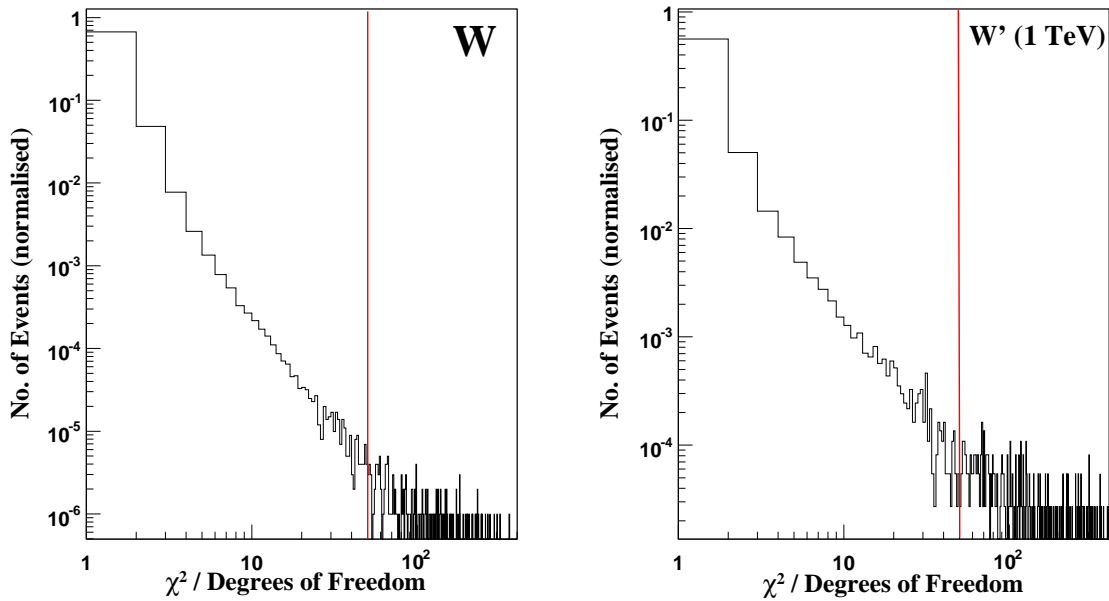
Figure 8.7: *Normalized distribution of the χ^2 of the muon track fit divided by the degrees of freedom used within the fit for the W and the 1 TeV W'. Due to the larger momentum and increased bremsstrahlung probability of TeV-muons the relative fraction of excluded muons is larger in the W' sample.*

The distributions for the $W \rightarrow \mu\nu$ sample and the 1 TeV W' sample are displayed in figure 8.7. They are characterised by an accumulation of nearly all the muon tracks at low values and a large tail giving rise to values up to 400. A sensible value for the separation of these two areas is a χ^2 divided by the degrees of freedom of 50 (see line in figure 8.7).

This cut has been chosen to further increase the quality of the reconstructed muons. The choice is confirmed by the comparison of the reconstructed muon p_T with the generator input (see figure 8.8): the relative error of the excluded muons is significantly larger. Especially those muons, which have a large p_T-deviation, are sorted out. This is a crucial selection, since those muons, faking high transverse momenta, give rise to large background.

An exact separation of well reconstructed muons from badly reconstructed ones or even fakes is not possible with this cut. However this criterion is a compromise between quality assurance and signal efficiency. Smaller values (downto 10) for this cut have been tried without a further improvement of the muon quality. Therefore only the tail of the distribution has been excluded.

Ghost Suppression

A small percentage of the muons is reconstructed twice due to a problem within the reconstruction algorithm (for details see section 7.1.4). These "pairs" of muons pass the detector in the same direction and, as further investigations showed, one muon is built out of numerous hits with a reasonable χ^2 value of the fit, whereas the other muon uses significantly less hits and has a larger χ^2. Since the parameters of the higher quality muons are matching within the errors with the generator muon properties, the decision has been taken to keep only the better one of each pair.
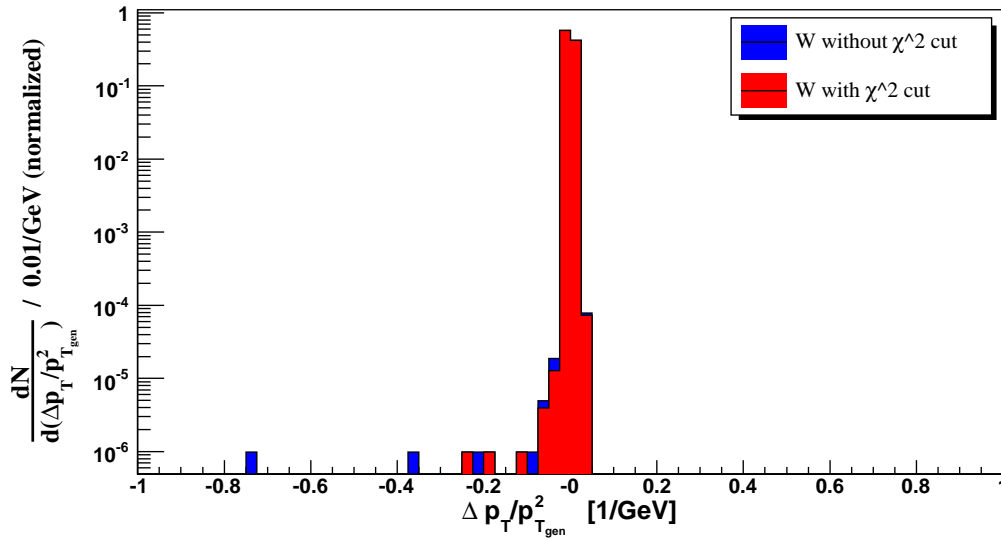
Figure 8.8: *Effect of the χ^2 cut on the muon momentum resolution. Especially muons, whose momenta have been reconstructed with a huge discrepancy compared to the generator momenta, are excluded.*

The identification of such pairs has been performed by a simple cone algorithm. For each event containing more than one muon, a cone with a radius of

$$\Delta R = \sqrt{(\Delta \phi)^2 + (\Delta \eta)^2} \le 0.1$$

around the direction of each muon is scanned for another muon. In case of a second muon within this cone, the properties of both are compared and the muon with the better χ^2-fit value divided by the degrees of freedom used for the fit is kept, while the other muon is excluded from the event.

Two high energetic muons flying in the same direction cause a massive energy and momentum imbalance in the detector. In the worst case this results in a high transverse mass from the fake muon with a by far too large reconstructed p_T and the also too large reconstructed missing energy. Thus, at the same time the missing transverse energy has to be corrected. To do this, the momenta p_x, p_y of the muon, which is excluded from the event, are added to the x and y components of the missing energy, respectively. Finally the corrected transverse missing energy and the corrected angle of the missing energy direction in the transverse plane are calculated.

8.3.2   Single Muon Cut

$W' \to \mu\nu$ events are likely to contain only a single muon. Further muons can only arise from the beam remnants and pile-up. Since the beam remnants are mainly lost through the beam pipe, the origin of these muons is restricted to additional proton-proton reactions occurring at the same time. These pile-up events are mainly QCD events containing jets and thus have a large fraction of hadronic particles, but contain only a small amount of muons. The signal events with a second global reconstructed muon are only a fraction of less than 3%.

Z^0 bosons which decay into leptons, produce, in difference to the W and W', always pairs of leptons. Since the highest energetic muon originating from a Z^0 combined with the naturally comprising missing transverse energy at pp-colliders gives rise to large transverse invariant masses, it poses background in the region above $M_T > 200$ GeV. To exclude this background the events are required to contain only one global reconstructed muon.

8.3.3 Muon Isolation

Muons from the decay of W' bosons are isolated in contrast to muons arising from the decay chain within a jet, i.e. no other particles are flying in the same direction as the muon. Only beam remnants and underlying events might produce particles casually flying in the muon direction.

As described in detail in the appendix (section B.3) three different muon isolation algorithms are implemented in the CMS reconstruction software at the moment. They are all based on the same principle: in a cone with a radius $\Delta R = \sqrt{(\Delta\eta)^2 + (\Delta\phi)^2}$ around the muon direction the transverse energy deposit or the transverse momentum excluding the muon itself is computed.

For the calorimeter isolation the transverse energy deposit, and for the pixel and tracker isolation the p_T of the particles inside a cone reconstructed by the pixel detector and the tracker, respectively, are computed. All three algorithms have been tested with some variations of the parameters. The tracker isolation with the default value ($\Delta R = 0.17$), which has already been optimised using a $W \to \mu\nu$ sample [75], gives the best results.

The calorimeter isolation algorithm has the drawback, that its quality is depending on the amount of underlying events and therefore becomes less effective at high luminosities. The pixel algorithm relies on the local track reconstruction within the pixel detector using three layers of pixel detectors. The small lever arm of the pixel detector limits a reasonable reconstruction to tracks with a p_T smaller 10 GeV and thus is also excluded (for details see B.3 or [75]).

Since the tracker isolation algorithm relies on the tracker, robust and high quality reconstruction using several silicon layers is guaranteed and thus a good basis for track isolation is provided. To have an efficient algorithm, only tracks which result in a p_T larger than 0.8 GeV are reconstructed.

In figure 8.9 the distribution of the transverse momentum within the isolation cone is shown for background and signal according to a luminosity of 10 fb^{-1}.

The cut at 0.8 GeV on this variable has been determined by optimizing signal efficiency times purity as a function of the isolation value. Since the algorithm only reconstructs tracks with p_T larger 0.8 GeV within the isolation cone, the cut is identical to the requirement of having no additional tracks within the cone around the muon.

8.4 Overview

Tables 8.2 and 8.3 give an overview of the number of events in 10 fb^{-1} which survive the cuts. The efficiency is given with respect to the number of events after the preselection.
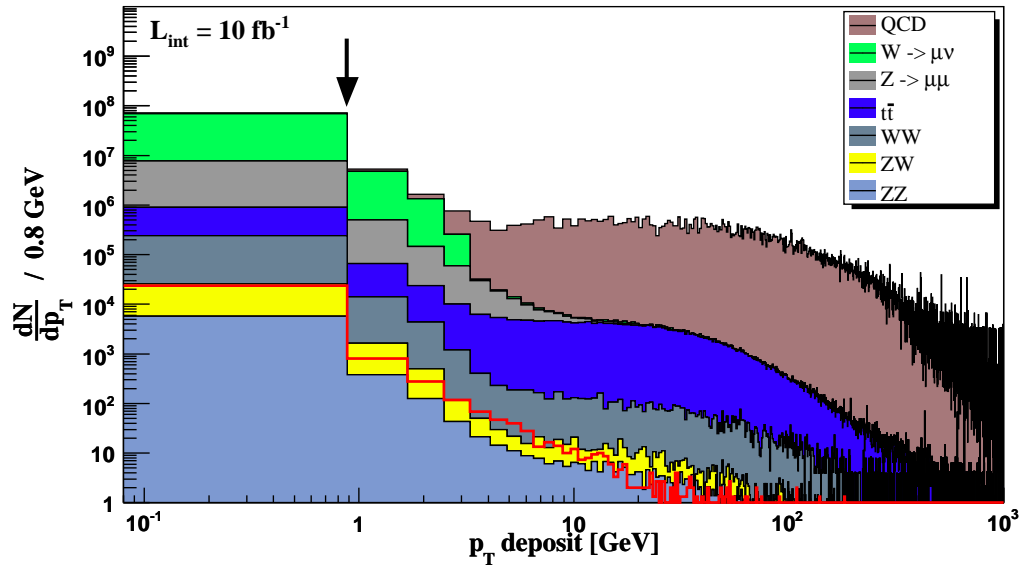
Figure 8.9: *Transverse momentum in a cone around the muon as a result of the tracker isolation algorithm. Signal efficiency times purity has been optimised to obtain the cut (arrow).*

Events in 10 fb^{-1} (Signal, $W' \to \mu\nu$ and W)					
Cut	1 TeV	3 TeV	5 TeV	7 TeV	$W \to \mu\nu$
Total	$3.11 \cdot 10^4$	$1.82 \cdot 10^{-2}$	$6.07 \cdot 10^0$	$8.56 \cdot 10^{-1}$	$9.84 \cdot 10^7$
Preselection	$2.51 \cdot 10^4$	$1.51 \cdot 10^2$	$4.83 \cdot 10^0$	$6.40 \cdot 10^{-1}$	$6.73 \cdot 10^7$
μ-Quality	$2.48 \cdot 10^4$	$1.47 \cdot 10^2$	$4.70 \cdot 10^0$	$6.32 \cdot 10^{-1}$	$6.71 \cdot 10^7$
Single μ	$2.43 \cdot 10^4$	$1.43 \cdot 10^2$	$4.61 \cdot 10^0$	$6.24 \cdot 10^{-1}$	$6.61 \cdot 10^7$
μ-isolation	$2.28 \cdot 10^4$	$1.34 \cdot 10^2$	$4.33 \cdot 10^0$	$5.86 \cdot 10^{-1}$	$6.11 \cdot 10^7$
Efficiency	90.8%	88.7%	89.6%	91.5%	90.8%

Table 8.2: *W' signal events and W background events, which remain after the subsequent application of the selection cuts.*

Events in 10 fb^{-1} (Background)					
Cut	$Z \to \mu\mu$	QCD	$t\bar{t}$	WW	ZW	ZZ
Total	$6.90 \cdot 10^9$	$4.92 \cdot 10^6$	$1.88 \cdot 10^6$	$2.69 \cdot 10^5$	$1.11 \cdot 10^5$	$1.11 \cdot 10^4$
Preselection	$7.46 \cdot 10^6$	$5.10 \cdot 10^7$	$9.84 \cdot 10^5$	$2.42 \cdot 10^5$	$2.20 \cdot 10^4$	$6.64 \cdot 10^3$
μ-Quality	$7.42 \cdot 10^6$	$5.00 \cdot 10^7$	$9.75 \cdot 10^5$	$2.41 \cdot 10^5$	$2.19 \cdot 10^4$	$6.60 \cdot 10^3$
Single μ	$4.00 \cdot 10^5$	$4.44 \cdot 10^7$	$7.05 \cdot 10^5$	$2.16 \cdot 10^5$	$1.60 \cdot 10^4$	$2.00 \cdot 10^3$
μ-isolation	$3.65 \cdot 10^5$	$1.29 \cdot 10^6$	$4.58 \cdot 10^5$	$1.93 \cdot 10^5$	$1.45 \cdot 10^4$	$1.62 \cdot 10^3$
Efficiency	4.9%	$1.8 \cdot 10^{-4}$	46.5%	79.8%	65.9%	24.4%

Table 8.3: *Background events, which remain after the subsequent application of the selection cuts.*

8.5   Distributions of Characteristic Quantities

After applying all stated selection cuts, the characteristic variables are shown for signal and background for an integrated luminosity of 10 fb^{-1}.

8.5.1   Transverse Momentum of the Muon
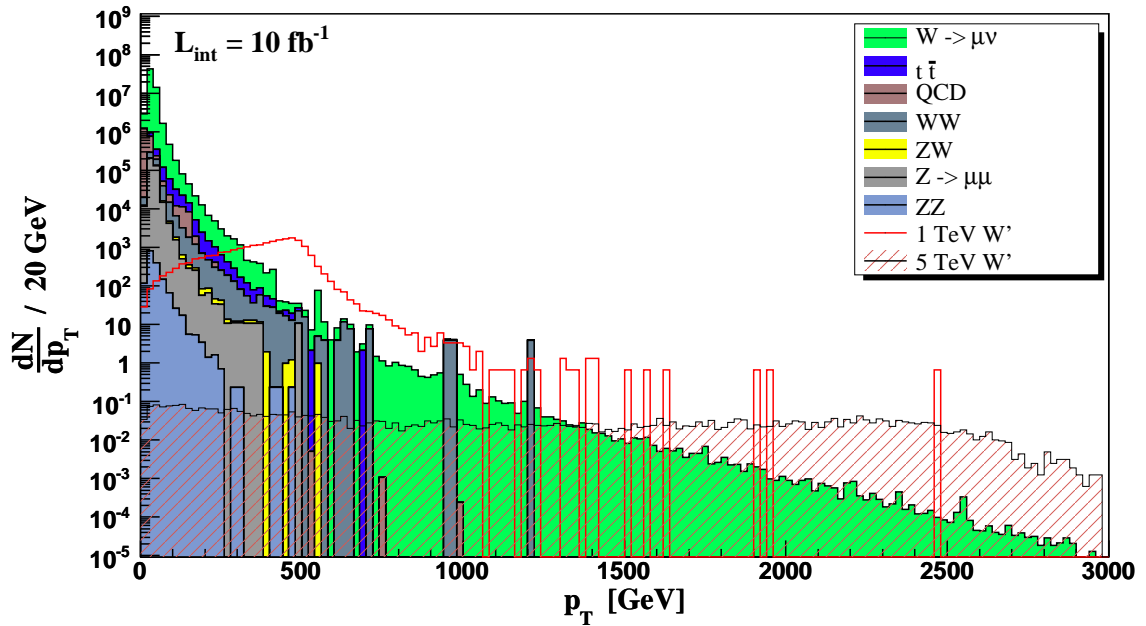
Figure 8.10: *Signal (1 TeV and 5 TeV W', non-stacked) and background (stacked) distribution of the transverse momentum of the highest energetic muon. The background is rapidly decreasing with large momenta, while the 1 TeV signal shows a Jacobian peak, which is smeared out due to the detector resolution; in case of the 5 TeV W' it is not visible.*

In figure 8.10 the p_T-distribution of the 1 and 5 TeV W' signal and the background is shown. The muons arising from background processes dominate the momentum distribution at low momenta, but their contribution falls rapidly with larger momenta. Over the whole p_T-range the fraction of $W \to \mu\nu$ represents the largest background. This justifies the fact, that for large transverse invariant masses only the $W \to \mu\nu$ background has been taken into account.

The spikes at large momenta arise from single muons, which have been reconstructed with a too large momentum. Because of the limited number of detector-simulated events, which is smaller than the number of events expected in 10 fb^{-1}, the background has to be scaled to the one expected in 10 fb^{-1}.

The 1 TeV signal distribution is hidden by the huge background at momenta smaller than 300 GeV. But a Jacobian peak, much larger then the expected background, is clearly visible around $M_{W'}/2$. The peak is smeared out due to the detector resolution.

The p_T-distribution of the 5 TeV signal is almost flat due to the offshell production (see section 6) and a Jacobian peak is hardly visible any more. For transverse momenta above 1500 GeV, the 5 TeV W' signal exceeds the background. However, the expected number

of signal events in one year LHC operation is less than 5 for a 5 TeV W' and thus the discovery of such a heavy object is only possible with a large amount of data.

For masses between 1–5 TeV the Jacobian peak, located at $M_{W'}/2$, is smeared out more and more caused by two effects: the first is the increasing W' offshell production (see section 6) and the second is the detector resolution. As shown in table 6.1 the expected number of W' events decreases rapidly with the assumed W' mass.

8.5.2 Missing Transverse Energy

The transverse missing energy distribution after the application of all selection criteria is shown in figure 8.11 for the 1 and 5 TeV signal (non-stacked) and the background (stacked).
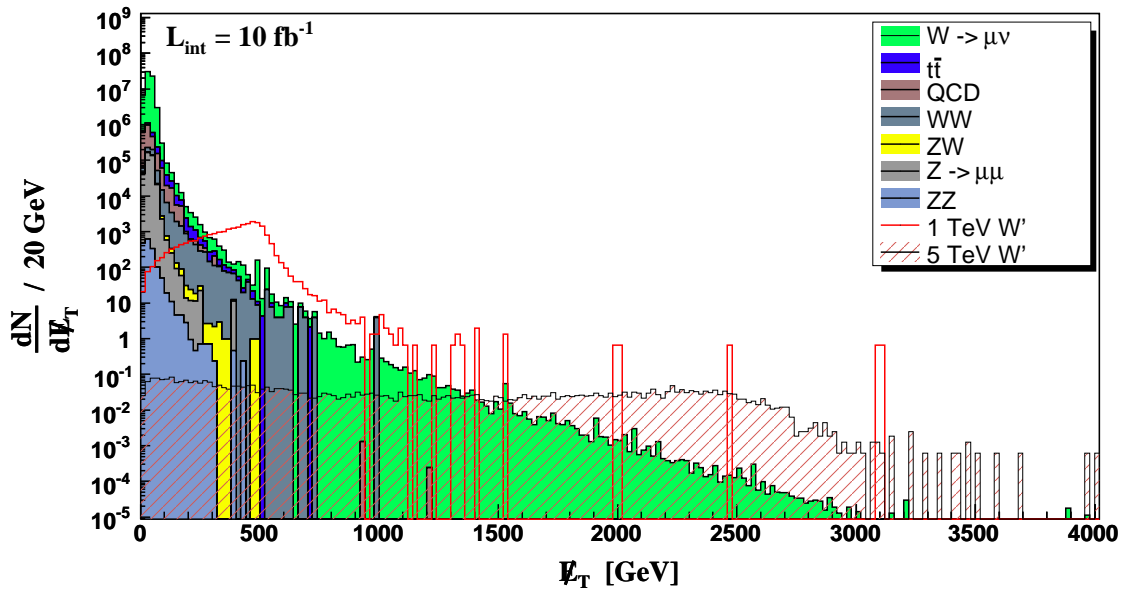
Figure 8.11: *Missing energy in the transverse plane for signal (1 and 5 TeV W', non-stacked) and stacked background. For large missing energies the distribution is determined by the missing energy produced by the large transverse momentum carried by the muon and not by calorimeter deposits.*

The distribution, especially in the signal region above 200 GeV, is almost identical to the p_T-distribution. This is evident, since the large amount of missing transverse energy is not given by calorimeter deposits, but by the large momentum of the muon, which deposits only a very small amount of its energy in the calorimeters. Roughly speaking, the missing transverse energy is approximately given by the transverse muon momentum smeared by the calorimeter deposits. Since this missing energy, which arises from underlying events and pileup, neglecting the muons p_T, is uniformly distributed, the shape of the missing energy distribution is not changed.

Due to the similarity of the p_T and $\not{E}_T$ distribution, the already stated comments in the previous section concerning signal and background are valid.

8.5.3 Angle between Muon and Missing Transverse Energy

Since the missing energy can only be determined in the transverse plane at a pp-collider, the angle between the muon and the missing energy is measured in this plane. The distribution is shown in figure 8.12.
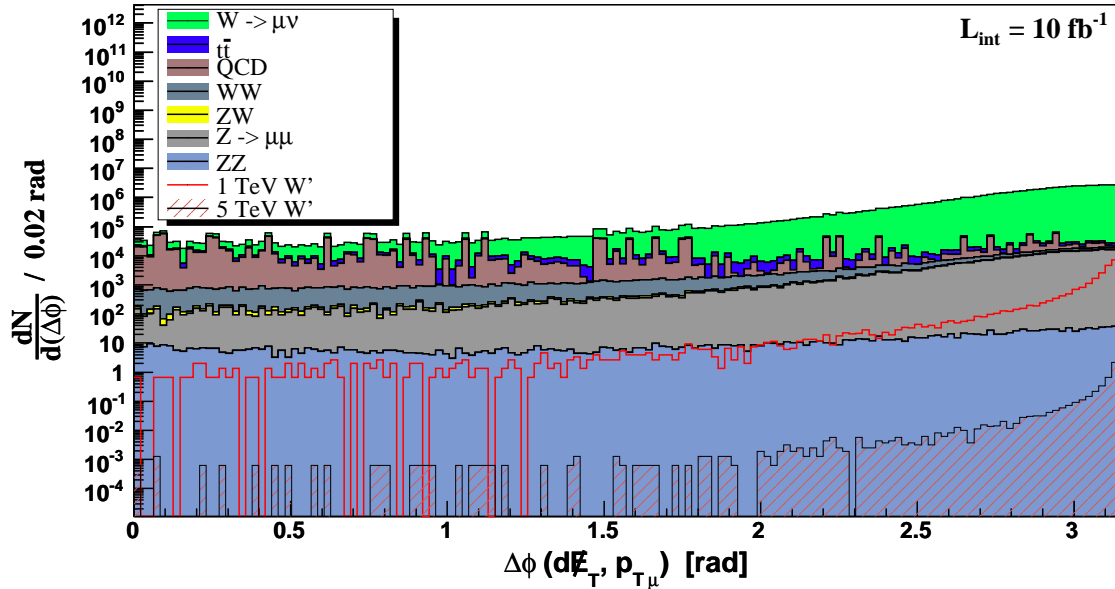
Figure 8.12: *Distribution (stacked background and non-stacked signal) of the angle between the transverse missing energy and the transverse momentum of the muon in the transverse plane. The signal strongly peaks at 180°.*

While for most backgrounds (QCD, $t\bar{t}$, ZZ) this variable is uniformly distributed, it peaks for W, Z and especially for the signal at 180°. For the W and W', this behaviour is given by the decay properties: in the rest frame of the W/W' the muon and neutrino are emitted back-to-back. The angle in the transverse plane changes due to transverse momenta of the W/W'. Due to the smaller muon and neutrino p_T in case of a W compared to ones arising from a W', boosts have a larger impact on the angle in case of a W.

The $Z \to \mu\mu$ events have also an accumulation around 180° due to the event selection and detector inefficiencies. Demanding only single muon events, one muon has to escape undetected. This causes an energy imbalance in the direction of the undetected muon, faking missing energy. As a result one obtains a W-like signature of a muon accompanied by missing energy in the opposite direction.

8.5.4 Transverse Invariant Mass

Finally these three variables, the transverse momentum of the muon, the missing transverse energy and the angle between both in the transverse plane are combined to the transverse invariant mass using the formula

$$M_T = \sqrt{2 p_{T_\mu} \not{E}_T (1 - \cos \Delta\phi_{\mu\not{E}_T})}. \tag{8.1}$$
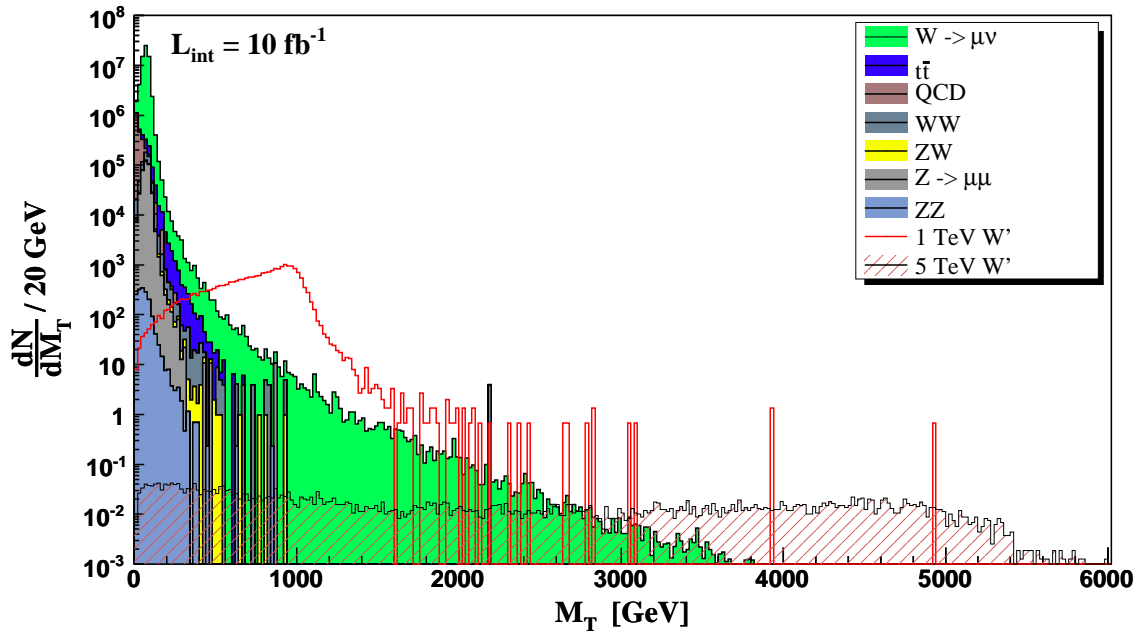
Figure 8.13: *Signal (1 TeV and 5 TeV W′) and background distribution of the transverse invariant mass.*

The already observed shapes in the p_T- and $\not{E}_T$-spectrum are visible and the separation of signal and background is even better. The background, which is mainly given by the $W \to \mu\nu$ sample, is exceeded by all considered W' masses at large transverse masses.

However, the question remains up to which W' mass a significant separation of signal and background is possible with a certain integrated luminosity. To obtain an answer, this distribution is used as an input to the significance test explained in the next chapter.

Chapter 9

Statistical Interpretation

In chapter 8 selection criteria have been applied to optimise the ratio between signal and background and to achieve the best possible separation. The results displayed in the transverse invariant mass spectrum (see figure 8.13) have to be investigated in a statistical manner to decide up to which W' masses a signal for new physics can be detected if present or excluded if absent. Of course this mass limit will be obtained at a certain significance: typically a deviation of 5σ from background expectations states a discovery, while a 95% exclusion level is quoted if there is no signal.

This chapter describes the CL_s-method ([76–78]) to obtain a limit at a certain significance before applying to the data attained from the full detector simulation.

9.1 The Statistical Method

From a mathematical point of view the decision of the observability of a signal hidden within the Standard Model background is a hypothesis test (for a detailed review see [79]). A test quantity has to be defined which can be used to model the signal significance and thus to decide if the signal can be separated from the background with a certain statistical precision. This quantity should be chosen in a way that the result, "Having a signal" (traditionally called null hypothesis) can be separated from the alternative hypothesis "There is no signal" with the minimal possible error rate. In statistics there exist two types of errors: "error of the first kind" representing the exclusion of a signal where there is one. The other type of error, "error of second kind", is the false discovery although no signal is present. The aim is to reduce both errors as far as possible.

Looking at the binned transverse invariant mass distribution for a certain W' mass with N bins in total one can interpret every single bin as a result of an independent Poisson counting experiment with the probability distribution

$$P(\mu; n) = \frac{\mu^n}{n!} \cdot e^{-\mu}. \tag{9.1}$$

For a given mean value μ, $P(\mu; n)$ reflects the probability to obtain the result n in a counting experiment if μ is expected.

In the context of a particle search the bins contain background but might as well have an amount of signal. Therefore one can think of two different "per bin counting experiments"

looking at the final variable (see figure 8.13). One counting experiment can use as mean value μ the number of *signal plus background* events ($\mu = s + b$), while the other experiment takes the number of background events ($\mu = b$) as mean.

These two probabilities, P (μ = s + b; n) and P (μ = b; n), can be used to construct a discrimination variable for the significance of the signal. The Neyman-Pearson lemma ([79], proof in [80]) states that using the likelihood ratio Q_i, calculated for each bin i,

$$Q_i(m_{W'}) = \frac{P(\mu = s_i(m_{W'}) + b_i; \ n_i)}{P(\mu = b_i; \ n_i)} \tag{9.2}$$

minimizes errors of the first and second kind. $s_i(m_{W'})$ is the number of signal events in bin i, which is a function of the W' mass $m_{W'}$, and b_i is the number of background events in bin i.

For a given signal s_i and background b_i prediction (for example given by a Monte Carlo simulation) one can calculate the likelihood ratio Q_i for having n_i events in this bin actually measured. Since in this study the number of signal events in a single bin depends on the mass of the W' it is a parameter of the likelihood. The overall combination of the N "per bin counting experiments" is gained by the multiplication of each probability ratio

$$Q(m_{W'}) = \prod_{i=1}^{N} Q_i(m_{W'}). \tag{9.3}$$

Instead of using the variable Q it is convenient and practical to work with $-2 \ln Q(m_{W'})$. A simple straight forward calculation using equation (9.2) and (9.1) leads to

$$-2 \ln Q(m_{W'}) = -2 \sum_{i=1}^{N} \left[n_i \ln \left(1 + \frac{s_i}{b_i} \right) - s_i \right] = 2s_{\text{tot}} - 2 \sum_{i=1}^{N} n_i \ln \left(1 + \frac{s_i}{b_i} \right). \tag{9.4}$$

This value has the advantage of being a difference of two χ^2-distributions in the limit of large statistics ($\mu \to \infty$): the Poisson distribution tends towards a normal distribution and therefore its natural logarithm has χ^2-character.

$$
\begin{aligned}
-2 \ln Q(m_{W'}) \quad &= \quad -2 \ln \prod_{i=1}^{N} \frac{P(\mu = s_i(m_{W'}) + b_i; n_i)}{P(\mu = b_i; n_i)} \tag{9.5} \\
&= \quad -2 \sum_{i=1}^{N} \ln P(\mu = s_i(m_{W'}) + b_i; n_i) + 2 \sum_{i=1}^{N} \ln P(\mu = b_i; n_i) \tag{9.6} \\
&\xrightarrow{\mu \to \infty} \quad \chi_{s+b}^2 - \chi_b^2. \tag{9.7}
\end{aligned}
$$

Thus, the value $-2 \ln Q$ converges against the χ^2-difference of the fits, which represent the *signal plus background* and *background only* distributions.

Looking at formula (9.4) one can interpret the likelihood ratio as the sum of measured events n_i, which are weighted with $\ln(1 + s_i/b_i)$. This sum is shifted by the sum of total measured signal events s_{tot}. For the calculation of the likelihood ratio $-2 \ln Q$ bins with a signal to background ratio lower than 5% are neglected. Although the addition of these bins would always improve the sensitivity, the systematic error introduced at the same time spoils this improvement. For a detailed explanation of this issue see [81].

In the last chapter cuts have been applied to the MC signal samples for the different simulated W' masses and for the MC background processes. In the final variable, the transverse invariant mass, which has been divided into 100 bins, the significance test is performed.

The determination of the signal significance is now performed by generating numerous so called "pseudo-experiments": for each bin in the transverse invariant mass, Poisson distributed random numbers are generated once using the mean value $\mu = s_i + b_i$ and once $\mu = b_i$ to generate different n_i (see equation (9.4)). The resulting transverse invariant mass distribution is within statistical considerations equal to the obtained Monte Carlo distribution, e.g. one can interpret this as the result of an identical experiment also measuring the transverse invariant mass distribution.

This generation of "pseudo-experiments" is repeated numerously. For each experiment the $-2 \ln Q$ using formula (9.4) is calculated and filled in a histogram (see figure 9.1). As a result one obtains two Gaussian shaped distributions centered at the $-2 \ln Q$ of $\mu = s_i + b_i$ and $\mu = b_i$, respectively (see figure 9.1).
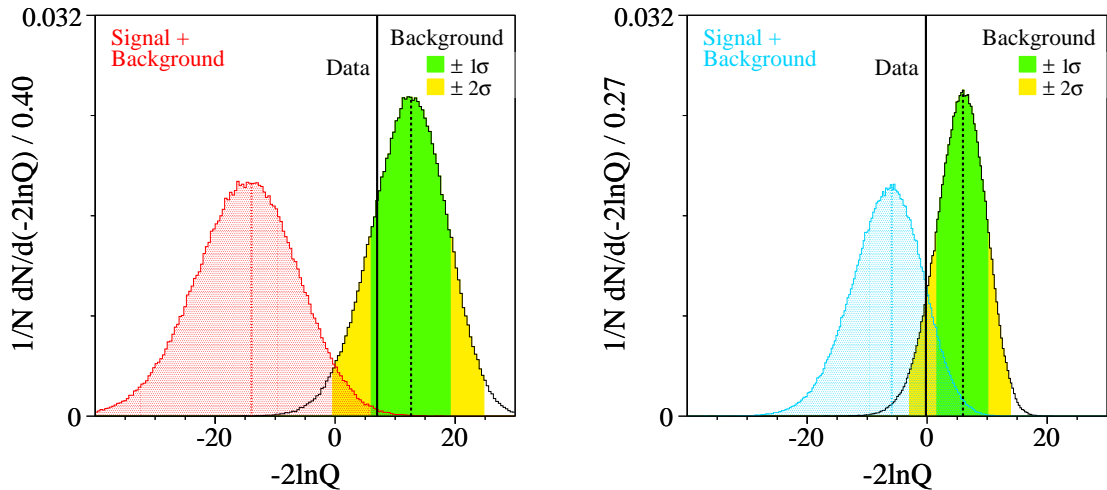
Figure 9.1: *Typical distribution of the $-2 \ln Q$ for different signals.*

By definition, as given in formula 9.4, the $-2 \ln Q$-values of the *signal plus background* are located in the negative range centered around the $-2 \ln Q$ of $\mu = s_i + b_i$, while the *background only* is cumulated at positive values centered around the $-2 \ln Q$ of $\mu = b_i$. The separation between both distributions is a measure for the signal sensitivity of an experiment: the smaller the overlap of the two $-2 \ln Q$ distributions is, the better one can distinguish between *signal plus background* and *background only*, i.e. separate signal from background. For example, the signal significance corresponding to the $-2 \ln Q$-distributions in the left plot of figure 9.1 is much larger than in the right plot (same figure).

For both Gaussian-like distributions the corresponding σ-deviation around the mean values can be extracted: 68% of the pseudo-experiments are within one σ around the centre. In figure 9.1 the $\pm 1\sigma$ and $\pm 2\sigma$-bands are plotted for the *background only* distribution. The corresponding $-2 \ln Q$ values for the σ-level are used for the calculation of the error on the significance as shown below.
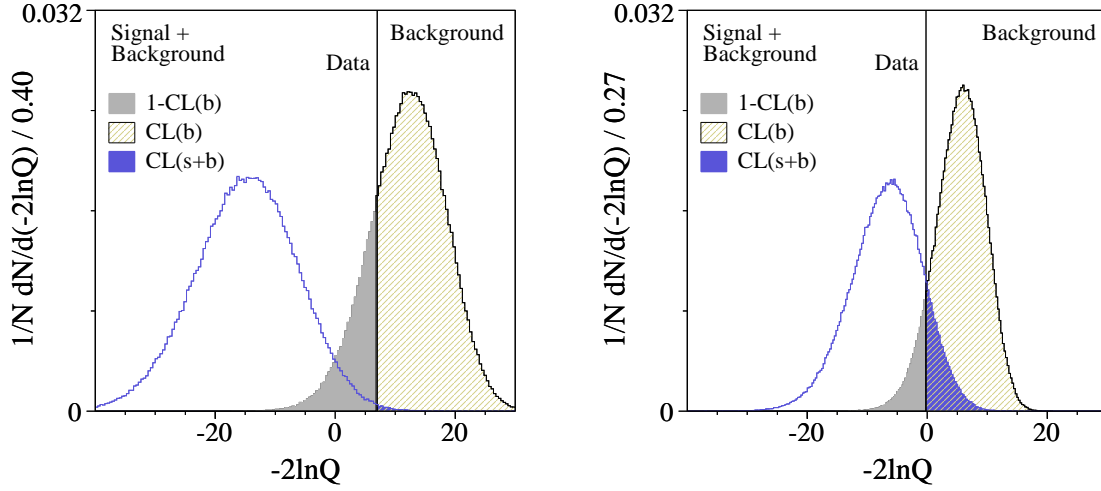
Figure 9.2: *Illustration of the different CL-integrals for the $-2\ln Q$ distributions assuming real data.*

For the determination of the different confidence level (CL) for each hypothesis, the distributions of the achieved pseudo-statistic are integral-normalised and defined as $\mathcal{P}_{\mathrm{s+b}}(x)$ and $\mathcal{P}_b(x)$ using $x := -2\ln Q$, respectively. To decide, if the hypothesis of having measured *background only* is true, the integral

$$\mathrm{CL_b} = \int_{X_0}^{\infty} \mathcal{P}_{\mathrm{b}}(x)dx \qquad (9.8)$$

is investigated. The integration border X_0 is the value of $-2\ln Q$ from an experiment (real data) or from Monte Carlo simulation. The calculation of the $\mathrm{CL_b}$ gives a measure in how far the experimental data are in coincidence with the *background only* expectation.

An X_0 smaller[1] than the mean value of $\mathcal{P}_{\mathrm{b}}(x)$ (as shown in figure 9.2) indicates, that "the data contain more than just background". Thus, the probability of a signal on top of the expected background is larger and the CL_b holds values larger than 0.5 (see figure 9.2).

An X_0 larger than the mean value of $\mathcal{P}_{\mathrm{b}}(x)$ states that the data do not even match with the background expectation and the $\mathrm{CL_b}$ is less than 0.5 (lack of background). Recapitulating, $\mathrm{CL_b}$ results in values around 0.5, when data match with background expectation, while $\mathrm{CL_b}$ holds larger values for data containing background plus additional signal.

In the same manner one can test the significance for having *signal plus background* measured, using

$$\mathrm{CL_{s+b}} = \int_{X_0}^{\infty} \mathcal{P}_{\mathrm{s+b}}(x)dx. \qquad (9.9)$$

In case an experiment has only measured background the integral is less than 0.5, while it is larger than 0.5 when the measured data exceed the signal plus background expectation. Again it is identical to 0.5, if the measurement is in coincidence with the $-2\ln Q$ MC expectation for *signal plus background* (see figure 9.1).

---

[1] Be aware that the *signal plus background* distribution $\mathcal{P}_{\mathrm{s+b}}(x)$ is left of the *background only* distribution $\mathcal{P}_{\mathrm{b}}(x)$.

Assuming a Gaussian character for both $\mathcal{P}_{\mathrm{s+b}}(x)$ and $\mathcal{P}_{\mathrm{b}}(x)$ a discovery is defined as an excess[2] in the measured data of more than 5σ:

$$1 - \mathrm{CL_b} \leq 5.7 \cdot 10^{-7}. \tag{9.10}$$

Now it is clear, that the sensitivity is correlated to the separation of the distributions $\mathcal{P}_{\mathrm{s+b}}(x)$ and $\mathcal{P}_{\mathrm{b}}(x)$, since the $1 - \mathrm{CL_b}$ reflects the overlap of both distributions.

If a discovery is not possible an exclusion limit can be calculated per convention with 95% confidence. Thus, the probability for excluding an existing signal is less than 5%, which can be mathematically described by

$$\mathrm{CL_{s+b}} < 0.05. \tag{9.11}$$

In other words: the probability to find a signal-like fluctuation compared to the background is excluded in this way with 95% confidence.

The use of $\mathrm{CL_{s+b}}$ has drawbacks, which might result in unphysical effects (see [76–78]). To avoid this, the ratio $\mathrm{CL_{s+b}}$ is normalised to $\mathrm{CL_b}$:

$$\mathrm{CL_s} = \frac{\mathrm{CL_{s+b}}}{\mathrm{CL_b}}. \tag{9.12}$$

The 95% exclusion level is given by

$$\mathrm{CL_s} < 0.05. \tag{9.13}$$

The error for the different confidence levels, i.e. the σ-deviation, can be extracted from the σ-bands of $\mathcal{P}_{\mathrm{s+b}}(x)$ and $\mathcal{P}_{\mathrm{b}}(x)$. A change of the integration border X_0 in the $\mathrm{CL_b}$-integral of $\pm\sigma$ directly results in the upper and lower error on the confidence level CL. The narrower the distributions of the pseudo-statistics, the smaller the error on the discovery or exclusion limit.

Significance within a Feasibility Study

Since there are no CMS data available yet, the integration border X_0 for the CL-integrals are not given by experimental data. Instead once the $-2\ln Q$ of the MC expectation for *signal plus background*, and, alternatively *background only* is used (see figures below). The choice of these values arises naturally, since the identical *signal plus background* and *background only* values would be measured if the MC simulation models the detector and the physics in a perfect manner.

Using this value, the calculation of $\mathrm{CL_{s+b}}$ for *signal plus background* and the calculation of the $\mathrm{CL_b}$ for *background only* is trivial. Since the integration border X_0 is identical with the mean of the $\mathcal{P}_{\mathrm{s+b}}(x)$ or $\mathcal{P}_{\mathrm{b}}(x)$ the $\mathrm{CL_{s+b}}$ or the $\mathrm{CL_b}$, respectively, is 0.5 .

The discovery definition, given by $1 - \mathrm{CL_b}$ analysed for *signal plus background*, is easier to visualize than in the case of real data: a discovery is claimed if the tail of $\mathcal{P}_{\mathrm{b}}(x)$, which exceeds the mean of $\mathcal{P}_{\mathrm{s+b}}(x)$, contains less than $2.85 \cdot 10^{-5}\%$ of the normalised pseudo-events (one-sided 5σ-deviation).

---

[2]If an excess of 5σ appears, one still has to check that the excess results from the investigated signal!

The drawbacks of the CL_{s+b} are also irrelevant for a feasibility study due to a lack of measured data. The relevant CL_s analysed for *background only* is given by

$$CL_s = 2 \cdot CL_{s+b}. \tag{9.14}$$

Therefore the limit determination using CL_s is more conservative, and thus, has been used within this study.

In order to determine the expected discovery limit or the expected 95% exclusion level for the CMS detector the W' mass, up to which the relation (9.10) (discovery) or (9.13) (95% exclusion) is valid, respectively, has to be found.

9.2 The Discovery and Exclusion Limit

The likelihood ratio for the different W' masses (1–8 TeV) and for the Standard Model background can be calculated according to equation (9.4). Figure 9.3 shows the result of the calculations for the different investigated W' masses. It represents the $-2 \ln Q$ mean values of the $\mathcal{P}_b$ (*background only*) and $\mathcal{P}_{s+b}$ (*signal plus background*) (see figure 9.1) as a function of the W' mass. The plot shows how well both hypotheses, *background only* and *signal plus background*, can be separated for masses below 5 TeV.
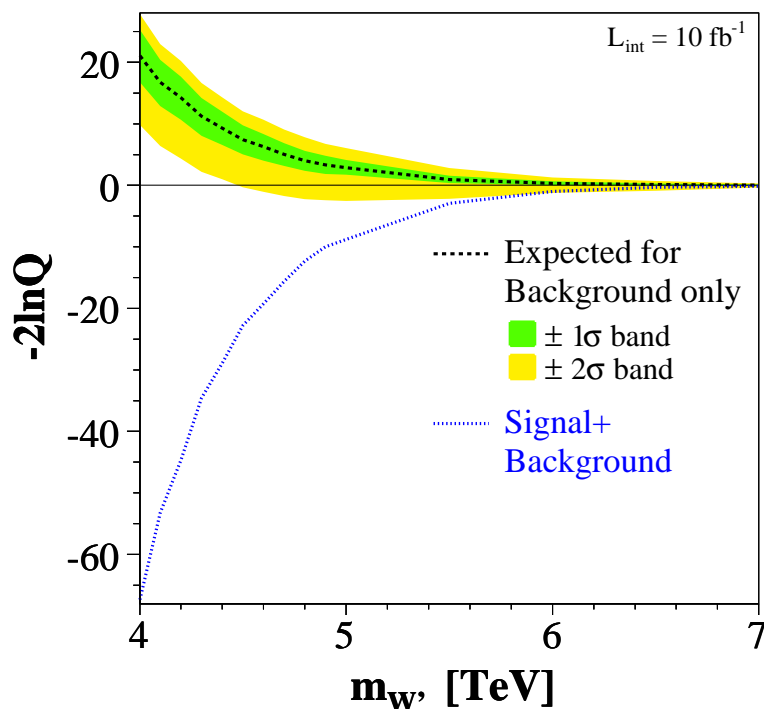
Figure 9.3: $-2 \ln Q$ *distribution for* signal plus background *and* background only *as a function of the* W' *mass. For the* background only *graph also the* $\pm 1\sigma$ *and* $\pm 2\sigma$*-bands are plotted. Both curves are well separated for masses below* 5 TeV.

9.2.1 Discovery

Based on the calculated likelihood ratio the significance for the *background only* hypothesis given by CL_b can be determined. As explained in section 9.1 the CL_b is a measure for the probability of having measured only background. By definition the CL_b for *background only* (and therefore also the $1 - CL_b$) are identical to 0.5 (see equation (9.8)). This statement is validated by figure 9.4. The CL_b value for *signal plus background* is larger than 0.5 and reflects the fact, that the hypothesis contains "more than only background", i.e. additional signal.
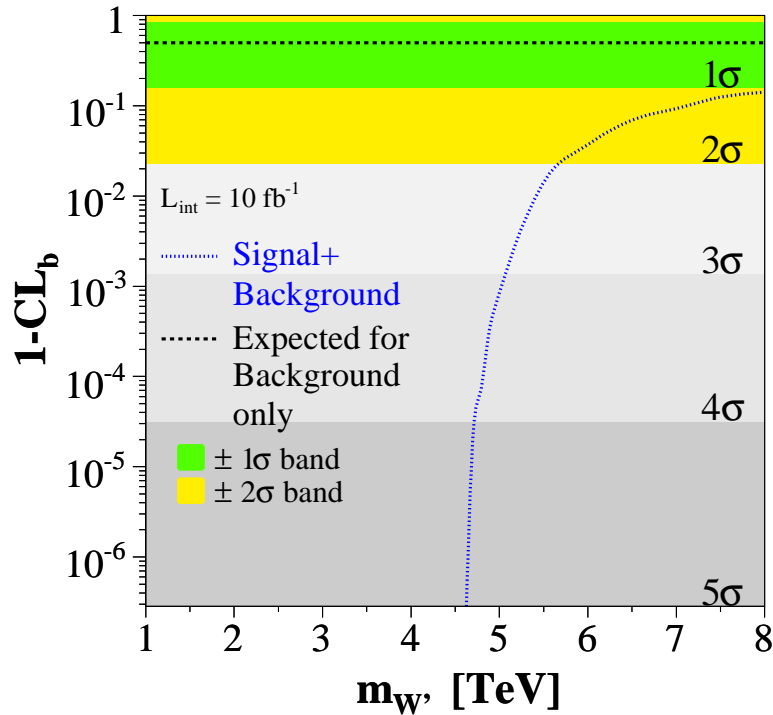
Figure 9.4: $1 - CL_b$ *distribution for* signal plus background *and* background only. *By definition the* background only *curve is independent from the tested W' mass at 0.5. According to the σ-deviation of the* signal plus background *curve from the background the discovery limit is determined to be $m_{W'} < 4.6$ TeV.*

For a significant discrimination between the *signal plus background* and the *background only* distribution, the CL_b is close to 1. Therefore, $1 - CL_b$ is used for the determination of the signal significance. In figure 9.4 the $1 - CL_b$ for *background only* (black dotted) and the σ-bands, which state the significance of a deviation, are plotted.

According to relation (9.10) a discovery is claimed if a 5σ deviation from *background only* appears. Since the likelihood method investigates one-sided deviations a 5σ deviation equals $1 - CL_b < 2.85 \cdot 10^7$.

Figure 9.4 states, that for an integrated luminosity of 10 fb^{-1} an expected W' with a mass up to 4.6 TeV can be discovered. For larger W' masses the *signal plus background* curve converges against the *background only* expectation. However, for a 8 TeV W' and a luminosity of 10 fb^{-1} a deviation of more than 1σ is still observable.

9.2.2 Exclusion

In case of no signs for new heavy charged gauge bosons, a 95% CL exclusion limit can be set. It states up to which mass an expected W' can be exluded at a significance level of 95%. This limit corresponds to a CL_s less than 5%. The CL_s distribution according to an integrated luminosity of 10 fb^{-1}, which is equal to one year of LHC operation, as a function of the W' mass is shown in figure 9.5. A limit of

$$m_{W'} < 4.71 \text{ TeV} \qquad \text{at 95\% CL}$$

can be set. The statistical errors are given by the $\pm 1\sigma$- and $\pm 2\sigma$-bands.
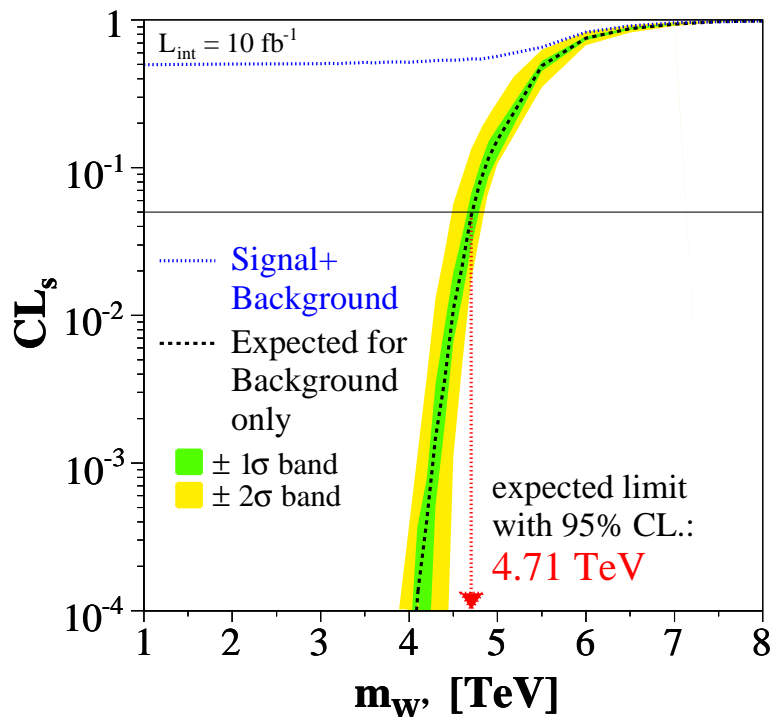
Figure 9.5: *CL_s distribution for* signal plus background *and* background only. *The exclusion limit at 95% CL, given at CL_s = 0.05, is $m_{W'}$ = 4.71 TeV.*

9.2.3 Luminosity Dependence of the Limit

In order to investigate the limit improvement the statistical method is repeated using a scaled integrated luminosity in the range 1–300 fb^{-1}. Within this luminosity range the discovery limit (see figure 9.6) and the 95% exclusion limit (see figure 9.7) is calculated for various luminosities with the corresponding statistical errors.

Already with an integrated luminosity of 1 fb^{-1} a W' boson with a mass smaller than 3.5 TeV can either be discovered or excluded with 95% CL. Including more data, the discovery as well as the exclusion limit increase up to 6 TeV for an integrated luminosity of 300 fb^{-1}.
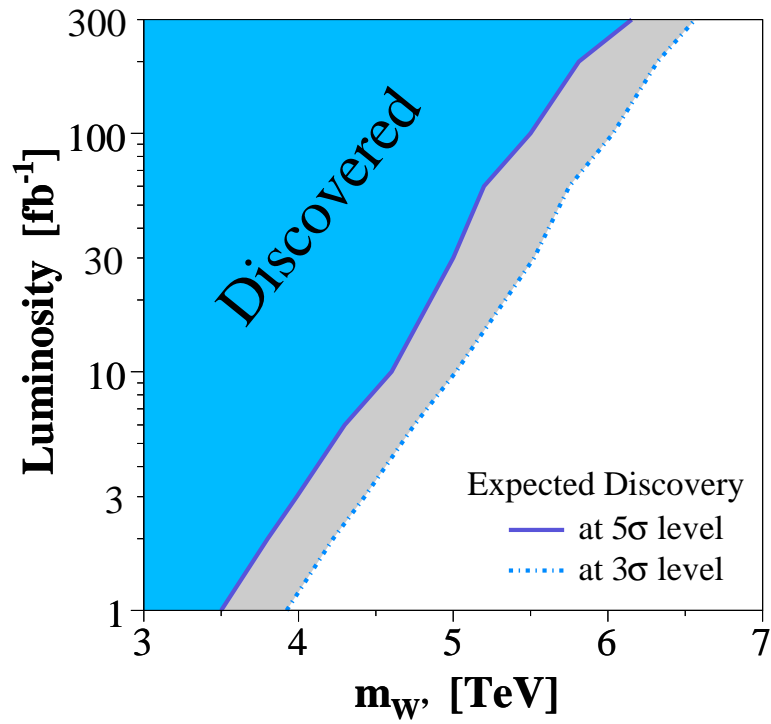
Figure 9.6: *Discovery limit as a function of the investigated integrated luminosity.*
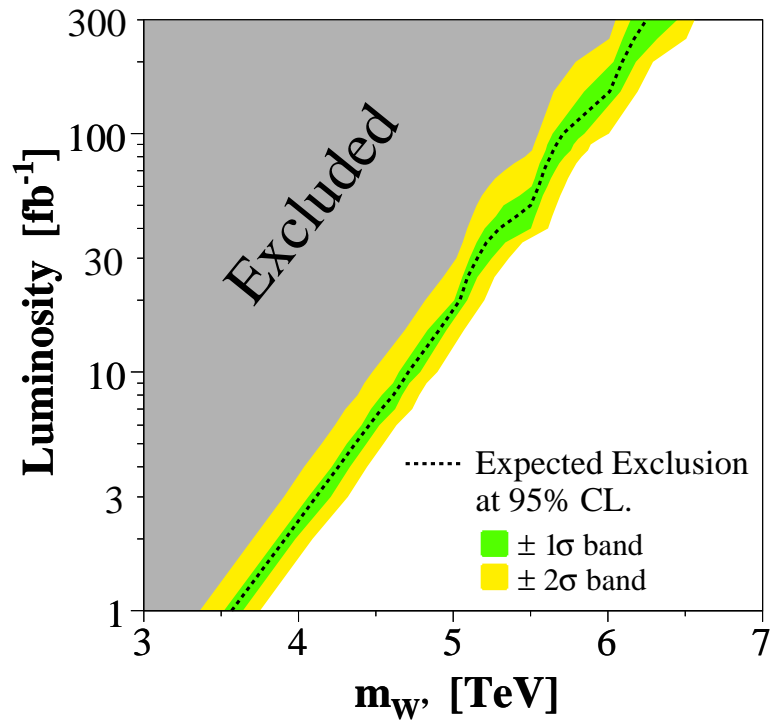
Figure 9.7: *95% CL exclusion limit as a function of the investigated integrated luminosity.*
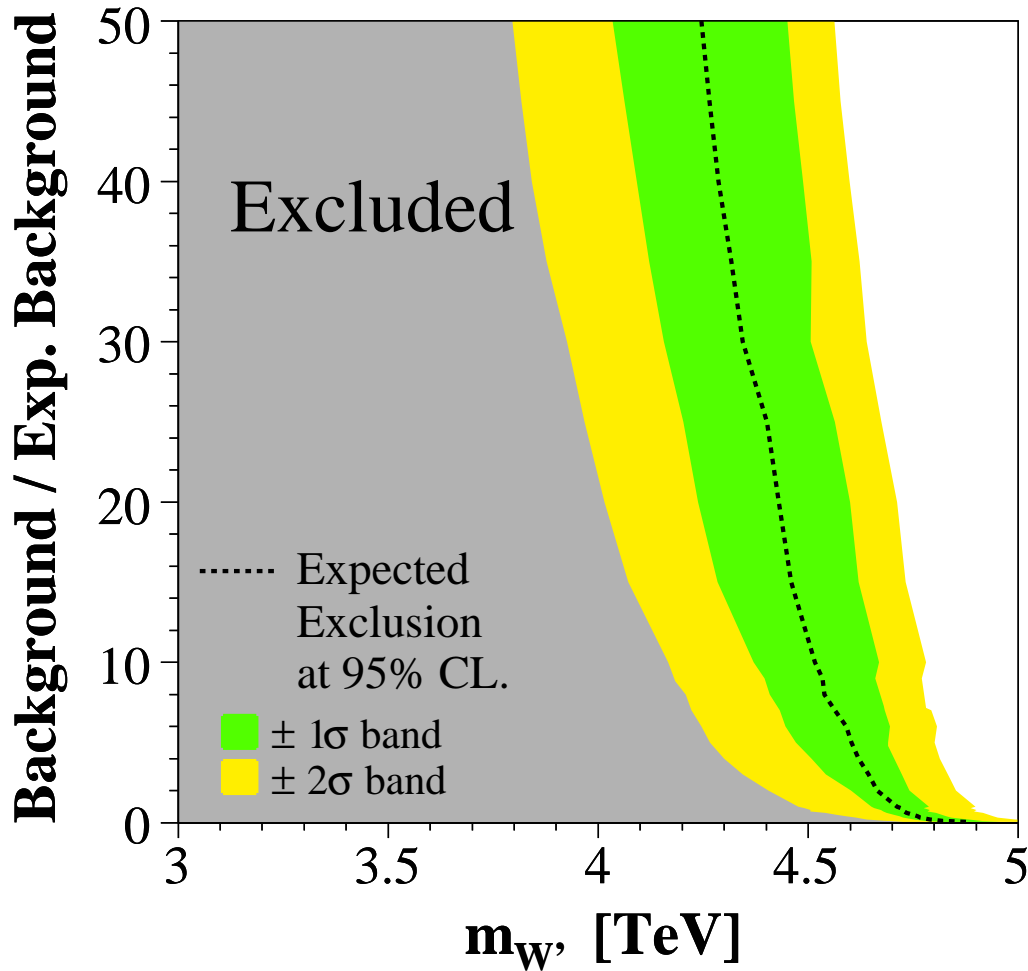
Figure 9.8: *95% CL exclusion limit as a variation of the expected background.*

9.2.4   Signal and Background Variation

To investigate the influence of a background under- or overestimation on the exclusion limit, the background is scaled. The same procedure has been repeated with the signal to investigate the sensitivity of the limit.

Figure 9.8 shows the exclusion limit as a variation of the background normalised to the expected background obtained from the Monte Carlo simulation. Thus, the y-axis value 1 is equivalent to the MC background expectation for an integrated luminosity of 10 fb^{-1}. While scaling the background the signal cross section is kept constant.

Even if the background has been underestimated by a factor 50 within this feasibility study the upper exclusion limit drops only slightly below 4.3 TeV.

The same variation has been performed for the signal, while keeping the background identical to the MC expectation. The signal cross section, normalised to the cross section of the Reference Model, has been varied in the range 0.01–2. The former case corresponds to a 100 times lower cross section, while the latter is equal to a doubled cross section.
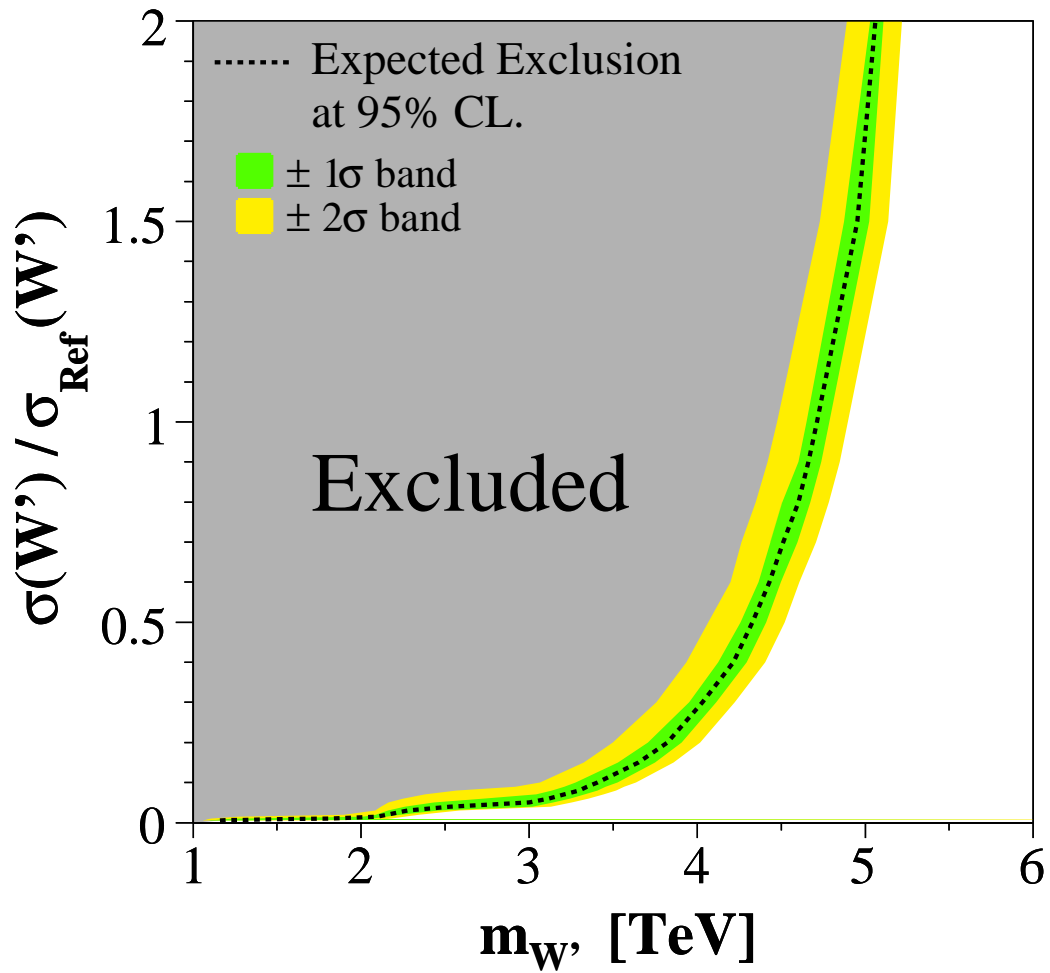
Figure 9.9: *95% CL limit as a variation of the expected signal.*

As shown in figure 9.9 the 95% exclusion limit is above 4 TeV taking signal scaling factors of above 0.25 into account. For smaller scaling values the exclusion limit rapidly falls to zero.

Chapter 10

Conclusions and Outlook

In this thesis a feasibility study for new heavy charged gauge bosons with the full CMS detector simulation has been presented. These new particles have been investigated within the Reference Model in the decay muon plus a light non-detectable particle, such as the Standard Model neutrino. The model assumes a new heavy charged gauge boson W' to be a carbon copy of the Standard Model W, but with a different mass. The W' mass, which is the only free parameter of the Model, has been investigated in the range 1–8 TeV.

All Standard Model background processes have been taken into account. According to the low luminosity phase of the LHC ($\mathcal{L} = 2 \cdot 10^{33}$ cm^{-2} s^{-1}) on average 3.5 pileup events have been mixed with the signal and background samples.

It has been shown, that new heavy charged gauge bosons, which behave similar to the SM ones, can be discovered (5σ) with an integrated luminosity of 10 fb^{-1} in the mass range of 0.1–4.6 TeV. If no signal is visible at CMS, an exclusion limit with 95% CL of $m_{W'} < 4.71$ TeV can be set. With an integrated luminosity of 300 fb^{-1} both limits can be extended to a W' mass $m_{W'}$ above 6 TeV.

Variations of the signal and background cross sections have been performed to investigate the influence of an underestimation of the background or an overestimation of the signal on the expected exclusion limit. Within a wide range of variations the mass exclusion limit remains above 4 TeV for an integrated luminosity of 10 fb^{-1}.

Systematic uncertainties resulting from higher order cross sections, parton density functions and scale dependencies have not been taken into account. Further studies are necessary to determine uncertainties arising from detector misalignment, dead detector components and the consideration of cosmic background.

From 2007 onwards CMS will start data taking and will give a chance for the investigation of new physics. If new heavy charged gauge bosons are realised within nature at the TeV-scale, they should be discovered.

Appendix A

Technical Details

A.1 Example of a Production Card

```
C
C     W' --> mu nu (W' mass = 1000 GeV)
C     ============

LIST

C  Specify output file and RUN:

   CFIL 'EVTO' 'mcevents_wprime_1000_munu.ntpl'
   KRUN 001

C -------------------------
C PYTHIA Particle Properties and Process Selection
C -------------------------

   PMAS 34, 1 = 1000           ! mass of W'
   MSEL = 22                   ! W'+- production (ISUB = 142)

C Switch off all W' decay channels beside W' --> mu nu

   MDME 311, 1 = 0             ! W' --> dbar + u
   MDME 312, 1 = 0             ! W' --> dbar + c
   MDME 313, 1 = 0             ! W' --> dbar + t
   MDME 314, 1 = -1            ! W' --> dbar + t'
   MDME 315, 1 = 0             ! W' --> sbar + u
   MDME 316, 1 = 0             ! W' --> sbar + c
   MDME 317, 1 = 0             ! W' --> sbar + t
   MDME 318, 1 = -1            ! W' --> sbar + t'
   MDME 319, 1 = 0             ! W' --> bbar + u
   MDME 320, 1 = 0             ! W' --> bbar + c
   MDME 321, 1 = 0             ! W' --> bbar + t
   MDME 322, 1 = -1            ! W' --> bbar + t'
   MDME 323, 1 = -1            ! W' --> b'bar + u
   MDME 324, 1 = -1            ! W' --> b'bar + c
   MDME 325, 1 = -1            ! W' --> b'bar + t
   MDME 326, 1 = -1            ! W' --> b'bar + t'
   MDME 327, 1 = 0             ! W' --> e    + nu_e
   MDME 328, 1 = 1             ! W' --> mu   + nu_mu           <=========
   MDME 329, 1 = 0             ! W' --> tau  + nu_tau
   MDME 330, 1 = -1            ! W' --> tau' + nu_tau'
   MDME 331, 1 = -1            ! W' --> W+   + Z0
   MDME 332, 1 = -1            ! W' --> W+   + gamma
```

```
   MDME 333, 1 = -1            ! W' --> W+   + h0

   MSTU 21 = 2                 ! particle/parton configuration check
   MSTJ 11 = 4                 ! fragmentation function D = 4
   MSTJ 22 = 2                 ! A particle is decayed only
C                                 if its proper lifetime is smaller than PARJ(71)
C                                 default should be ok. Other idea define the
C                                 detector volume with MSTJ 22 = 4
   MSTP 51 = 7                 !structure function chosen (D = 7)
   MSTP 81 = 1                 !multiple parton interactions (D = 1)
   MSTP 82 = 1                 !Defines the multi-parton model (D = 1)


C ---------
C GENERATOR
C ---------

   KSEL = 0                   !similar to Pythia's MSEL
   NSEL = 1                   !number of events to produce
   TRIG = 10000000            !maximum number of tries
   ECMS = 14000.              !center of mass energy
   MRPY 1 = 231304            !random seed for PYTHIA
END
EOF
```

A.2   Used Data Samples

Background			
Type	Cross Section $[fb]$	Analysed Events	Official Sample
$W \to \mu\nu$	$1.719 \cdot 10^7$	1483999	mu03_W1mu
$W \to \mu\nu$	various	200 per $\widehat{p}_{\mathrm{T}}$-range	private
Z^0 inclusive	$1.453 \cdot 10^8$	721712	mu03_DY2mu
WW inclusive	$1.880 \cdot 10^5$	483000	jm03b_WWjets_inclusive
ZZ inclusive	$1.111 \cdot 10^4$	479000	jm03b_ZZjets_inclusive
ZW inclusive	$2.686 \cdot 10^4$	276993	jm03b_ZWjets_inclusive
$t\bar{t}$ inclusive	$4.920 \cdot 10^5$	2299736	jm03b_TTbar_inclusive
QCD	$4.997 \cdot 10^8$	286982	jm03b_qcd_120_170
QCD	$1.010 \cdot 10^8$	335000	jm03b_qcd_170_230
QCD	$2.386 \cdot 10^7$	384978	jm03b_qcd_230_300
QCD	$6.391 \cdot 10^6$	195000	jm03b_qcd_300_380
QCD	$1.890 \cdot 10^6$	191989	jm03b_qcd_380_470
QCD	$6.903 \cdot 10^5$	153987	jm03b_qcd_470_600
QCD	$2.025 \cdot 10^5$	89996	jm03b_qcd_600_800
QCD	$3.574 \cdot 10^4$	44000	jm03b_qcd_800_1000
QCD	$1.085 \cdot 10^4$	89748	jm03b_qcd_1000_1400
QCD	$1.056 \cdot 10^3$	35998	jm03b_qcd_1400_1800
QCD	$1.448 \cdot 10^2$	17997	jm03b_qcd_1800_2200
QCD	$2.382 \cdot 10^1$	46498	jm03b_qcd_2200_2600
QCD	$4.284 \cdot 10^0$	40164	jm03b_qcd_2600_3000
QCD	$8.439 \cdot 10^{-1}$	34742	jm03b_qcd_3000_3500
QCD	$9.654 \cdot 10^{-2}$	26497	jm03b_qcd_3500_4000

Table A.1: *Full list of the background samples used from the official CMS production and additional private produced $W \to \mu\nu$ samples (200 events per $\widehat{p}_{\mathrm{T}}$-range; 50 GeV $\widehat{p}_{\mathrm{T}}$-steps for 200 $< \widehat{p}_{\mathrm{T}} < 500$ and 100 GeV $\widehat{p}_{\mathrm{T}}$-steps for $500 < \widehat{p}_{\mathrm{T}} < 3000$). The cross section, number of analysed events and the official name is given. For more details on the data samples see the official CMS production page [82].*

Signal			
Type	Cross Section [fb]	Analysed Events	Sample
W' (1 TeV) $\rightarrow \mu\nu$	$3.110 \cdot 10^3$	46595	private
W' (2 TeV) $\rightarrow \mu\nu$	$1.583 \cdot 10^2$	8884	private
W' (3 TeV) $\rightarrow \mu\nu$	$1.824 \cdot 10^1$	9301	private
W' (3.1 TeV) $\rightarrow \mu\nu$	$1.490 \cdot 10^1$	10000	private
W' (3.2 TeV) $\rightarrow \mu\nu$	$1.236 \cdot 10^1$	10000	private
W' (3.3 TeV) $\rightarrow \mu\nu$	$1.015 \cdot 10^1$	10000	private
W' (3.4 TeV) $\rightarrow \mu\nu$	$8.406 \cdot 10^0$	10000	private
W' (3.5 TeV) $\rightarrow \mu\nu$	$6.986 \cdot 10^0$	9615	private
W' (3.6 TeV) $\rightarrow \mu\nu$	$5.829 \cdot 10^0$	9713	private
W' (3.7 TeV) $\rightarrow \mu\nu$	$4.832 \cdot 10^0$	10000	private
W' (3.8 TeV) $\rightarrow \mu\nu$	$4.065 \cdot 10^0$	10000	private
W' (3.9 TeV) $\rightarrow \mu\nu$	$3.387 \cdot 10^0$	10000	private
W' (4 TeV) $\rightarrow \mu\nu$	$2.869 \cdot 10^0$	10000	private
W' (4.1 TeV) $\rightarrow \mu\nu$	$2.428 \cdot 10^0$	9690	private
W' (4.2 TeV) $\rightarrow \mu\nu$	$2.076 \cdot 10^0$	10000	private
W' (4.3 TeV) $\rightarrow \mu\nu$	$1.750 \cdot 10^0$	10000	private
W' (4.4 TeV) $\rightarrow \mu\nu$	$1.484 \cdot 10^0$	10000	private
W' (4.5 TeV) $\rightarrow \mu\nu$	$1.268 \cdot 10^0$	9600	private
W' (4.6 TeV) $\rightarrow \mu\nu$	$1.086 \cdot 10^0$	10000	private
W' (4.7 TeV) $\rightarrow \mu\nu$	$9.239 \cdot 10^{-1}$	10000	private
W' (4.8 TeV) $\rightarrow \mu\nu$	$8.007 \cdot 10^{-1}$	10000	private
W' (4.9 TeV) $\rightarrow \mu\nu$	$6.982 \cdot 10^{-1}$	10000	private
W' (5 TeV) $\rightarrow \mu\nu$	$6.073 \cdot 10^{-1}$	9707	private

Table A.2: *Full list of the simulated signal samples used in this study. The cross section and the number of analysed events are given.*

Appendix B

Muons in ORCA

From the user's point of view there are two distinct ways to access muons in ORCA. With the first method one is able to perform "local" tasks, that means tasks which are closely related to a single detector component like a drift tube or a cathod strip chamber. It gives the possibility to retrieve all local information about simulated hits (SimHits), digitized hits (Digis) and local reconstructed track segments.

While the first method provides information which is of special interest for the muon experts and those who want to become one, the second method is absolutely essential for everyone whose work is related to muons, like a four-vector analysis with a muon in the final state. Everything related to reconstruction, which is global in the ambit of the muon system, such as global muon tracks, is accessible via this method.

Since the second method is of more general interest and gives already an overview of the muon as an object in the object-oriented reconstruction framework, this part is introduced first and later, tending towards greater depth, some components and the access to local muon objects are described.

Naming convention

In order to have a clear structure in the ORCA source code [83] the muon sub-packages are named after the detector component they model:

- **drift tube** related ones: begin with **MB** (short for **M**uon **B**arrel);

- **cathode strip chambers** related ones: begin with **ME** (short for **M**uon **E**ndcap);

- **resistive plate chambers** related ones: begin with **MRpc**.

B.1 Principle of Reconstruction

B.1.1 Local Reconstruction

The reconstruction of a muon track in CMS starts with the construction of track segments combining associated hits within the DT and CSC system.

For the DT system the obtained hits (with left-right ambiguity) are combined separately in the two different projections $r\phi$ and $r\theta$, building 2D-segments performing a linear fit. Left-right ambiguities are resolved by requiring the smallest χ^2. Since a track angle can

be determined for a 2D-segment the position of the hits is recomputed taking the impact angle into acount. Finally the two projections are combined to a so called 4D-segment.

In difference to the DT system each cathode strip chamber provides the measurement of two coordinates by a wire and a strip signal. Both coordinates are associated using a time coincidence of the hits. To complete the local track reconstruction within the CSCs a linear fit through the 3D-hits is performed starting with one hit in each, the first and the last layer, adding further hits according to a χ^2 compability.

B.1.2   Stand-alone Muon Reconstruction

As the name of the reconstructor implies only data from the muon system, i.e. excluding the tracker, are used in this algorithm. Starting from the local reconstructed track segments (4D/2D in DT) or 3D-hits (CSC) including RPC information the track is propagated outwards starting from the innermost DT/CSC using a Kalman filter technique. Its principle is to extrapolate the track to the next measurement surface, compare it with the measurement and update the track accordingly. In order to reject bad hits, which result mainly from bremsstrahlung showers and delta electrons, a χ^2-cut is applied. In case of a lack of hits in the measurement surface, due to detector inefficiencies, geometrical cracks or too many hits (electromagnetic shower), the track is extrapolated to the next station taking the muon energy loss in the material, multiple scattering effects and the non-constant magnetic field into account (GEANE). Iteratively the procedure is repeated until the outermost measurement is reached, updating the track parameters including errors at each step.

Finally, the track is extrapolated inwards using a backward Kalman filter to achieve the track parameters at the innermost muon station, but also at the nominal interaction point using a vertex constrained fit.

B.1.3   Global Muon Reconstructor

The global muon reconstructor starts with stand-alone muon tracks and includes hits in the silicon tracker and pixel detector. Again, using GEANE, which takes the energy loss and the magnetic field into account, the track is extrapolated from the muon system through the magnet coil and calorimeters into the tracker. Based on the track uncertainties and assuming the muon origin at the interaction point, regions of interest within the inner tracker are selected.

In these regions of interest regional track reconstruction is performed using all hit pairs of combinations of compatible pixel and double-sided silicon strip layers as candidates for the muon trajectory as regional seeds. From these regional seeds a track reconstruction based on a Kalman filter is done. It is performed in the following steps: starting in the innermost layer the track is iteratively propagated to the next layer including matching measurements and updated. A trajectory cleaner resolves ambiguities between multiple trajectories resulting from a single seed on the basis of the χ^2 and the number of hits used for the track fit.

Finally, the reconstructed track is fitted again, adding the hits, which fulfill a χ^2 criterion, from the standalone reconstruction.

B.2   Access to Muons within ORCA

Access to Global Reconstructed Muons

The reconstructed high level objects are given by so called *RecQuery*s (**rec**onstruction **query**s). With these *RecQuery*s one can access the *RecCollection*s (**rec**onstructed object **collection**s) defining an iterator, which points to the first reconstructed object. In case of a muon it is a so called *RecMuon*:

```
RecQuery q("GlobalMuonReconstructor");
RecCollection<RecMuon> recmuons(q);
RecCollection<RecMuon>::const_iterator muon = recmuons.begin();
```

The number of muons is given by the size of the *RecCollection*:

```
cout << "   Number of reconstructed muons: " << recmuons.size() << endl;
```

Looping over all muons their properties such as the degree of freedom, χ^2, momentum components, angles, etc. can be accessed by:

```
while ( muon != recmuons.end() ) {
  int nmeas        = (*muon).foundHits();
  int dof          = (*muon).degreesOfFreedom();
  double chi2      = (*muon).chiSquared();
  double normChi2 = (*muon).normalisedChiSquared();

  cout << setiosflags(ios::showpoint | ios::fixed)
       << setw(2) << idx+1 << '\t'
       << "number of measurements = " << nmeas
       << "  Chi2/DoF = " << setw(6) << chi2
       << "/" << setw(2) << dof
       << " = " << setw(6) << setprecision(3) << normChi2 << endl;

  TrajectoryStateOnSurface traj_vertex =
        ((*muon).stateAtVertex().isValid()) ?
            (*muon).stateAtVertex() : (*muon).innermostState();

  GlobalVector mom = traj_vertex.globalMomentum();
  GlobalPoint  pos = traj_vertex.globalPosition();
  int charge       = traj_vertex.charge();

  float pt    = mom.perp();
  float eta   = mom.eta();
  float theta = mom.theta();
  float phi   = mom.phi();
  float P     = mom.mag();

  cout << endl << setiosflags(ios::showpoint | ios::fixed)
```

```
            << setw(2) << idx+1 << '\t'
            << " E  = " << setw(7) << m_MuonE[idx]  << " GeV    "
            << " px = " << setw(7) << m_MuonPx[idx] << " GeV    "
            << " py = " << setw(7) << m_MuonPy[idx] << " GeV    "
            << " pz = " << setw(7) << m_MuonPz[idx] << " GeV    " << endl
            << " pt = " << setw(5) << pt             << " GeV    "
            << " charge = " << setw(2) << charge << " "
            << " eta   = " << setw(6) << eta << "     "
            << " theta = " << setw(6) << theta << "     "
            << " phi   = " << setw(5) << phi << " rad    " << endl
            << " Innermost/Vertex position = " << pos << endl;
 }
```

The muon track within the tracker and the track within the muon system can be printed and accessed separately by

```
    cout << "  Muon Track:" << endl << "  ===========" << endl;
    cout << *(*muon).muonTrack() << endl << endl;
    cout << "  Muon Tracker Track:" << endl
         << "  ===================" << endl;
    cout << *(*muon).trackerTrack() << endl;
```

An example listing of all hits/track segments from which a global reconstructed muon is constructed including the detector component, which has measured the hit, is given by

```
    vector<RecHit> rec_Hits = (*muon).recHits();
    for ( vector<RecHit>::const_iterator ihit = rec_Hits.begin();
          ihit != rec_Hits.end(); ihit++ ) {
      if ( ihit->isValid() ) {
        const DetType& type = ihit->det().detUnits().front()->type();
        cout << endl << "Measured hit " << setw(2) << i
             << " in " << setw(8) << type.module() << " ("
             << setw(7) << type.part() << ")"
             << " at " << ihit->globalPosition()
             << " (dim=" << (*ihit).dimension() << ")";
      }
      i++;
    }
```

A typical listing for a muon in the overlap region passing the DT and the CSC system would be:

```
 Hit  1 in   pixel  (barrel ) at  (-3.939,-2.482,-8.022)         (dim=2)
 Hit  2 in   pixel  (barrel ) at  (-5.982,-3.765,-10.700)        (dim=2)
 Hit  3 in   pixel  (barrel ) at  (-8.848,-5.571,-14.463)        (dim=2)
 Hit  4 in silicon  (barrel ) at  (-20.309,-12.789,-29.531)      (dim=2)
 Hit  5 in silicon  (barrel ) at  (-27.720,-17.455,-39.212)      (dim=2)
```

```
Hit  6 in silicon  (barrel ) at  (-33.814,-21.303,-45.619)      (dim=2)
Hit  7 in silicon  (barrel ) at  (-40.693,-25.645,-60.546)      (dim=2)
Hit  8 in silicon  (barrel ) at  (-58.160,-36.663,-79.254)      (dim=2)
Hit  9 in silicon  (barrel ) at  (-64.221,-40.480,-82.242)      (dim=2)
Hit 10 in silicon  (barrel ) at  (-74.237,-46.817,-98.981)      (dim=2)
Hit 11 in     rpc  (barrel ) at  (-348.694,-222.146,-469.697)   (dim=2)
Hit 12 in      dt  (barrel ) at  (-363.837,-230.917,-532.950)   (dim=2)
Hit 13 in      dt  (barrel ) at  (-359.345,-251.697,-488.935)   (dim=2)
Hit 14 in     rpc  (barrel ) at  (-379.086,-239.505,-469.697)   (dim=2)
Hit 15 in     rpc  (barrel ) at  (-418.298,-265.487,-591.197)   (dim=2)
Hit 16 in      dt  (barrel ) at  (-433.015,-274.996,-532.950)   (dim=2)
Hit 17 in     rpc  (barrel ) at  (-448.023,-284.002,-610.450)   (dim=2)
Hit 18 in     csc  (forward ) at  (-527.728,-333.753,-696.000)  (dim=2)
Hit 19 in     csc  (forward ) at  (-529.032,-335.287,-698.540)  (dim=2)
Hit 20 in     csc  (forward ) at  (-532.156,-337.463,-701.080)  (dim=2)
Hit 21 in     csc  (forward ) at  (-531.879,-337.943,-703.620)  (dim=2)
Hit 22 in     rpc  (forward ) at  (-560.998,-351.043,-715.400)  (dim=2)
```

The code to access other muons is mainly identical to the one used in the case of a global reconstructed muon. Only the *RecQuery* has to be changed:

- Standalone Reconstructor:
  RecQuery q("StandAloneMuonReconstructor")

- Isolated Muon Reconstructor (see section B.3):
  RecQuery q("IsolatedGlobalMuonReconstructor")

- Picky Muon Reconstructor (see section 7.2):
  RecQuery q("PickyMuonReconstructor")

- Truncated Muon Reconstructor (see section 7.2):
  RecQuery q("TruncatedMuonReconstructor").

B.3   Isolated Global Muon

For every global reconstructed muon one or more isolation criteria can be assigned, e.g. in order to reject muons arising from b- and c-quarks or K- and π-mesons, which dominate the muon rate at LHC but are a background to many physics processes.

In the ORCA reconstruction software there are three different isolation techniques implemented. The principle is quite simple: in a cone with a radius

$$\Delta R = \sqrt{(\Delta\eta)^2 + (\Delta\phi)^2} \tag{B.1}$$

around the direction of the muon the transverse energy deposit or the transverse momentum is computed. After subtraction of the muon contribution the gained value is compared to a (user-)defined threshold.

As a general behaviour these algorithms strongly depend on the muon's transverse momentum, since low energetic muons within the range of 4–30 GeV are dominantly produced

by b- and c-quark decays [84] they are accompanied by a jet. The origin for higher energetic muons are mainly due to gauge bosons, decaying into isolated muons without any jet correlation.

The optimisation of isolation criteria is also dependent on the LHC luminosity since the threshold parameters have to be adjusted to the average deposit in an angular element. Due to underlying events the number of particle tracks increases with a raising luminosity.

For all three algorithms the isolation parameters have been studied on reference samples with isolated muons (like $W \to \mu\nu_\mu$) and have been optimized for background reduction. The default values in ORCA are chosen to be the optimal ones (see [75]).

B.3.1 Calorimeter isolation

This algorithm uses the transverse energy deposited in a cone around the direction of the muon in the electromagnetic (ECAL) and hadronic calorimeter (HCAL). Independently, the deposits in the ECAL around the muon direction seen from the vertex and the HCAL deposits in a cone centered at the middle of the HCAL tower[1], which is hitted by the muon, are summed up.

In order to reject underlying events E_T cuts are applied and E cuts are used to suppress electronic and detector noise in the calorimeter towers. The thresholds for the HCAL are $E_\mathrm{T} > 0.5$ GeV and $E > 0.6$ GeV. For the ECAL the according thresholds are $E_\mathrm{T} > 0.2$ GeV and $E > 0.12$ GeV (barrel), $E > 0.45$ GeV (endcap).

To subtract the energy deposited by the muon itself the muon track is extrapolated to the boundary between ECAL and HCAL, to determine the precise point of incidence. The muon transverse deposit in the ECAL is defined to be the one in a cone of $\Delta R \leq 0.07$ around this point, while in the HCAL the tranverse energy of the single tower with the highest deposit in a cone of $\Delta R \leq 0.1$ around the incidence point is subtracted.

As the final isolation variable the transverse energy of both calorimeters is added with different weights

$$E_\mathrm{T} = \alpha \cdot \sum E_\mathrm{T}^{ECAL} + \sum E_\mathrm{T}^{HCAL} \tag{B.2}$$

and an optimal weight parameter of $\alpha = 1.5$. Since this algorithm is based on calorimeters it becomes less effective at high luminosities due to an "intrinsic" noise caused by underlying events in the calorimeters (pile-up sensitivity).

Typical thresholds on the summed transverse energy vary from 6.5 to 9 GeV for cone values between 0.13 and 0.45 with the optimum around 0.24. The isolation value is extracted from ORCA with the help of an instance of the *MuIsoByCaloEt* class. The cone size and the weight parameter can be changed by the user.

```
MuIsoByCaloEt MyCaloIsolation;
MyCaloIsolation.setConeSize(0.24);  // default value
MyCaloIsolation.setEcalWeight(1.5); // default value
```

Having a *RecCollection* of reconstructed muons *RecMuon* the isolation method returns the amount of transverse energy deposited within the cone subtracted by the muon fraction. It is also possible to specify the threshold and to obtain a *true/false* if the muon isolation is within/outside the threshold.

---

[1]different cone axes are used because of the higher granularity of the ECAL

```
RecQuery qIsolatedGMR("IsolatedGlobalMuonreconstructor");
RecCollection<RecMuon> MuonColl(qIsolatedGMR);
RecCollection<RecMuon>::const_iterator muon = MuonColl.begin();

while (muon != MuonColl.end()) {
  TrajectoryStateOnSurface traj;
  if ((*muon).stateAtVertex().isValid()) {
    traj = (*muon).stateAtVertex();
  } else {
    traj = (*muon).innermostState();
  }
  if (traj.isValid()) {
    float CaloIsoValue = MyCaloIsolation.isolation(*muon);
    bool IsIsolated = MyCaloIsolation.isIsolated(*muon, 8.0 );
    cout << "Transv. energy around the muon: " << CaloIsoValue << endl;
    cout << "Muon isolated? " << IsIsolated << endl;
  }
}
```

B.3.2   Pixel isolation

The pixel algorithm uses as an isolation criteria the sum of transverse momenta measured by the pixel detector in a cone around the muon direction neglecting the p_{T} of the muon itself. It takes only p_{T}-contributions from tracks into account, which originate from the same vertex as the muon to reduce contamination from underlying events and thus to be a powerful tool also at high luminosity. Since a precise vertex constraint for the muon is only available at an improved level of the reconstruction chain the pixel tracks of the global reconstructed muon are used to apply this algorithm. For a typical cone of $\Delta R = 0.2$ one applies an isolation cut of 2–4 GeV.

Since a 3D-track reconstruction within the pixel detector is only possible with three hits out of three pixel detector layers, the algorithm is highly reliant on the detector performance. Due to inefficiencies of the detector, geometrical acceptances and electronic read-out failures the functionality of the isolation extraction might be significantly restricted. For the start-up scenario this technique is not appropriate because of the staging of one out of three layers. The interrogation of the p_{T}-isolation value is done in an identical way as in the calorimeter isolation. The dedicated class providing this functionality is namend *MuIsoByPixelPt*.

```
MuIsoByPixelPt MyPixelIsolation;
MyPixelIsolation.setConeSize(0.2);  // default value
```

Caution: *The p_{T} assignment for pixel tracks is not precise for high transverse momenta tracks and thus the tracks inside the cone are programmatically limited to 10 GeV by an if-statement. This might result in spikes at 10, 20, 30, ... GeV when drawing the distribution of the isolation $\sum p_{\mathrm{T}}$ value for a high statistic data sample. The spikes correspond to 1, 2, 3, ... higher energetic tracks inside the cone with a p_{T} of more than 10 GeV [85].*

B.3.3   Tracker isolation

The tracker isolation is nearly identical to the pixel isolation algorithm: instead of using only the reconstructed tracks within the pixel detector it is fed by fully reconstructed tracks. The isolation value, which is the sum of transverse momenta $\sum p_\mathrm{T}$ is extracted from a cone around the muon by neglecting the muons contribution.

The tracks inside the cone (region of interest) are reconstructed with a regional algorithm ("regional tracking"). Track seeds are gained by pairs of pixel hits inside the isolation region with additional vertex and momentum constraints. Only tracks with $p_\mathrm{T} > 0.8$ GeV pointing towards the region of interest are included and the distance between the muon origin and the primary vertex should be smaller than $\Delta r = 0.1$ cm and $\Delta z = 0.2$ cm. To speed up the algorithm a track fit is stopped as soon as five hits are used for the fit. With an additional χ^2 cut for ghost suppression, the tracks contributing to the isolation cone are reconstructed sufficiently enough. Typically the cones used with this algorithm are around $\Delta R = 0.2$ and cuts applied to the p_T sum range from 2.0 to 3.0 GeV.

As in the two other cases the isolation information is provided by an instance of an isolation class (*MuIsoByTrackerPt*).

```
MuIsoByTrackerPt MyTrackerIsolation;
MyTrackerIsolation.setConeSize(0.17);  // default value
```

B.4   Access to local DT Muon Components

The inevitable starting point for an access to local muon information is the building of the detector geometry (map) from a XML-File[2]. (There is no other access to the local components than through the detector component to which the muon information belongs to.) This Builder constructs the different DT objects like wires (*MuBarWire*), layers of wires (*MuBarLayer*), superlayers (*MuBarSL*) and chambers (*MuBarChamber*) in a simple manner, which is sufficient for reconstruction purposes.

As the construction of the detector geometry is not a users' task this is done via the few lines:

```
MuBarrelSetup* MBSetup = Singleton<MuBarrelSetup>::instance();
const MuBarDetectorMap& MuonDetectorMap = MBSetup->map();
```

An instance of the muon barrel setup is generated. It is accesses the geometry map, which provides pointers to all of its subdetectors and their components. Now all chamber-, superlayer- and layer-pointers, stored in *vector*s, can be retrieved. And it can be checked if there are indeed 250 DT muon chambers in total.

```
const vector<MuBarChamber*> MuonChambers    = MuonDetectorMap.chambers();
const vector<MuBarSL*>      MuonSuperLayers = MuonDetectorMap.SLs();
const vector<MuBarLayer*>   MuonLayers      = MuonDetectorMap.layers();
cout << "Check: Number of DT chambers: " << MuonChambers.size() << endl;
```

---

[2]eXtensible Markup Language

B.4.1 Navigation through the DT system

The direct access to a special chamber, superlayer or layer is done in two steps: first an ID-object is needed, which specifies the location of the detector component (e.g. wheel, station, sector *etc.*). In a second step the map is asked to return a pointer to the desired detector object.

```
\\ access to the chamber in wheel 1, station 4, sector 3
MuBarChamberId ChamberID(1, 4, 3);
MuBarChamber* SingleChamber = MuonDetectorMap.getChamber(ChamberID);


\\ access to the second superlayer in wheel -2, station 3, sector 5
MuBarSLId SuperlayerID(-2, 3, 5, 2);
MuBarSL* SingleSL = MuonDetectorMap.getSL(SuperlayerID);


\\ access to layer 1 in SL 2 in chamber in wheel -2, station 4, sector 8
MuBarLayerId LayerID(-2, 4, 8, 2, 1);
MuBarLayer* SingleLayer = MuonDetectorMap.getLayer(LayerID);
```

It is also possible to navigate through or loop over the substructure of a detector component. The parent detector always holds the pointers to its children and via an iterator one can loop over them:

$$MuBarChamber \xrightarrow{accessto} MuBarSL \xrightarrow{accessto} MuBarLayer \xrightarrow{accessto} MuBarWire \qquad (B.3)$$

As an example the length of each wire in the DT system is printed starting from the vector which holds the pointers to the chambers. To handle this, one loops over all chambers and gets the *vector* containing the pointers to the superlayer within a single chamber. Then this procedure is repeated: a loop over each superlayer of a chamber is executed and the *vector* with the pointers to its layers is gained.

The last step is to access all wires within this layer. The loops are always realised via *iterator*s, which is the standard procedure for *vector*s. The iterator points to an element of the vector, which can be accessed so.

Now it would be natural to get a *vector* with the pointers to *MuBarWire*s, but unfortunately this is not possible. Thus, the access has to be gained by picking a special wire, like it is done for a single chamber, superlayer or layer as shown above: first build an ID-object *MuBarWireID* then ask the layer for the pointer.

```
for (vector<MuBarChamber*>::const_iterator
        ChamberIter = MuonChambers.begin();
        ChamberIter != MuonChambers.end(); ChamberIter++) {
  vector<MuBarSL*> SLinChamber = (*ChamberIter)->getSLs();
  for (vector<MuBarSL>::const_iterator SLIter = SLinChamber.begin();
          SLIter != SLinChamber.end(); SLIter++) {
    vector<MuBarLayer*> LayerinSL = (*SLIter)->getLayers();
    for (vector<MuBarLayer*>::const_iterator LayerIter=LayerinSL.begin();
            LayerIter != LayerinSL.end(); LayerIter++) {
```

```
        for (int i=1; i <= (*LayerIter)->nWire(); i++) {
           MuBarWireId WireID((*LayerIter)->id(), i);
           MuBarWire* wire = (*LayerIter)->getWire(WireID);
           cout << "Lenght of wire: " << wire->wireType()->length()
                << endl;
        }
     }
   }
 }
```

B.4.2   Digitized Hits in the DT system

Since every reconstructed hit or track segment is assigned to the detector component in which it is reconstructed, the *DetUnit*, only the pointer to the component under investigation has to be caught in order to obtain the digitized hit (Digi).

Figure B.1: *Overview of the relations between the detector objects and the reconstructed hit objects in the DT system.*

The derived *DetUnit*, which holds the pointer to the Digis is a *MuBarLayer* (access to a *MuBarLayer* see B.4.1). As an example the drift time of reconstructed hits (RecHit) is printed.

```
for (vector<MuBarLayer*>::const_iterator itDTLayer = DTLayer.begin();
        itDTLayer != DTLayer.end(); itDTLayer++) {
  // loop over all digis in one MuBarLayer
  vector<MuBarDigi> DTDigis = (*itDTLayer)->digis();
  int digiIdx = 0;
  for (vector<MuBarDigi>::const_iterator itDTDigis = DTDigis.begin();
         itDTDigis != DTDigis.end(); itDTDigis++) {
    cout << "     " << setw(2) << digiIdx + 1 << ". Hit: (Wire: "
         << itDTDigis->wire() << ", Layer: " << itDTDigis->layer()
         << ", SL: " << itDTDigis->slayer()
         << ", # of Digis in Layer: " << itDTDigis->number()
         << ", TDCCounts: " << setw(4) << itDTDigis->countsTDC()
         << ", Drift time: " << setw(5) << itDTDigis->time() ;
    if (itDTDigis->viewCode()==MuBarEnum::RZed) {
```

```
      cout << " in Theta-Layer" << endl;
    } else if (itDTDigis->viewCode()==MuBarEnum::RPhi) {
      cout << " in Phi-Layer" << endl;
    }
    digiIdx++;
  }
}
```

B.4.3   Access to Local Reconstructed Objects in the DT System

In this part the access to the local reconstructed track segments within the DT system is stated. The listing of all 4D-segments reconstructed within all DT superlayers is printed. Since the access to 2D-segments is similar, this challenge is ceded to the reader. As visualized in figure B.1 the 2D-segments and 4D-segments are given by the *DetUnit*s *MuBarSL* and *MuBarChamber*, respectively.

```
for (vector<MuBarChamber*>::const_iterator itChamber=DTChambers.begin();
        itChamber!=DTChambers.end(); itChamber++) {
  /// print DT segments 4D
  vector<RecHit> Segs4D =(*itChamber)->recHits();
  if (Segs4D.size()) {
    cout << endl << "There are " << Segs4D.size()
         << " 4D segments in Chamber "
         << (*itChamber)->id() << ": " << endl;
    // loop over 4D segments in the Chamber
  int Seg4DIdx = 0;
  for (vector<RecHit>::const_iterator itSeg4D = Segs4D.begin();
          itSeg4D != Segs4D.end(); itSeg4D++) {
      const Det* Detwith4DSeg = &(*itSeg4D).det();
    const MuBarChamber*
          MuCham = dynamic_cast<const MuBarChamber*>(Detwith4DSeg);
    if (MuCham) {
      cout << Seg4DIdx + 1 << ". 4D-Seg: Chamber in " << MuCham->id()
              << " (has " << MuCham->nSL() << " SL) " << endl
              << "   Position(local) : " << (*itSeg4D).localPosition()
              << ",  direction " << (*itSeg4D).localDirection() << endl
              << "   Chi2: " << setw(4) << (*itSeg4D).chi2()
              << ",  NDOF: " << setw(2) << (*itSeg4D).degreesOfFreedom();
    }
  }
 }
}
```

To access the 2D-segments the *MuBarChamber* iterator has to be replaced by a *MuBarSL*.

Another way to get the 2D-segements, is to ask the 4D-segments (given as the iterator *itSeg4D*) from which 2D-components are created via the *recHits()* method:

```
  vector<RecHit> Segs2D = (*itSeg4D).recHits();
  cout << " 4D segment made of "
       << (*itSeg4D).recHits().size() << " 2D-Seg(s)";
int Seg2DIdx = 0;
for (vector<RecHit>::const_iterator itSeg2D = Segs2D.begin();
        itSeg2D != Segs2D.end(); itSeg2D++) {
   ...
```

Since the 2D-segments are made of *RecHit*s, which are in this case reconstructed hits, they can again be accessed via the *recHits()* method this time using the 2D-segment iterator *itSeg2D*.

```
  vector<RecHit> hits = (*itSeg2D).recHits();
  for (vector<RecHit>::const_iterator itHits = hits.begin();
          itHits != hits.end(); itHits++) {
... loop over all RecHits (real hits) from which the 2D segment is built
```

However, the access to the drift time is only possible when having a *MuBarDigi*. To get the according *MuBarDigi* having a *RecHit* a special helper class has to be called, the *MuBarRecHitHelper*.

```
  MuBarRecHitHelper rhHelper = MuBarRecHitHelper((*itHits))
  vector<MuBarDigi> DigisfromRecHit = rhHelper.digis();
  for (vector<MuBarDigi>::const_iterator
     itDigisfromRecHits = DigisfromRecHit.begin();
       itDigisfromRecHits != DigisfromRecHit.end();
              itDigisfromRecHits++) {
   cout << "   " << setw(2) << hitIdx + 1
        << ". Hit: (Wire: " << itDigisAusRecHits->wire()
       << ", L: " << itDigisAusRecHits->layer()
       << ", SL: " << itDigisAusRecHits->slayer()
       << ", # of Digis: "  << itDigisAusRecHits->number()
    << ", TDCCounts: " << setw(4) << itDigisAusRecHits->countsTDC()
    << ", Drift time: " << setw(5) << itDigisAusRecHits->time() ;
if (itDigisAusRecHits->viewCode()==MuBarEnum::RZed) {
  cout << " in Theta-Layer" << endl;
} else if (itDigisAusRecHits->viewCode()==MuBarEnum::RPhi) {
  cout << " in Phi-Layer" << endl;
 }
 }
```

B.4.4   Simulated Hits in the DT System

Simulated hits (GEANT4) are accessed via a *MuBarLayer*. Since it has already been explained above how to get the pointer to a *MuBarLayer* only the essential lines of code are listed.

From the *MuBarLayer* the simulation detector class *SimDet*, which holds the simulated hits, is requested through the *simDet()* method and asked for the hits (*simHits()*). For the simulated data the particle ID, the direction and the momentum are printed.

```
const vector<MuBarLayer*> DTLayer = map.layers();
for (vector<MuBarLayer*>::const_iterator itDTLayer = DTLayer.begin();
     itDTLayer != DTLayer.end(); itDTLayer++) {
  if ((*itDTLayer)->simDet()->simHits().size() != 0 ) {
    cout << " Layer in " << (*itDTLayer)->id() << " contains "
         << (*itDTLayer)->simDet()->simHits().size() << " SimHits ";
    cout << "and " << (*itDTLayer)->nDigis() << " Digis " <<  endl;
    vector<SimHit*> Simis = (*itDTLayer)->simDet()->simHits();
    // loop over SimHits
    for (vector<SimHit*>::const_iterator itSimis = Simis.begin();
         itSimis != Simis.end(); itSimis++) {
      cout << "            " << SimIdx + 1
           <<  ". Type: " << (*itSimis)->particleType()
           << " at Pos: " << (*itSimis)->globalPosition()
           << ", Direction " << (*itSimis)->globalDirection()
           << " Momentum: " << (*itSimis)->pabs() << endl;
      SimIdx++;
    }
  }
}
```

Bibliography

[1] J. W. VON GOETHE: *Faust I.* 1808

[2] THE CMS COLLABORATION: *The Electromagnetic Calorimeter Project – Technical Design Report.* CERN/LHCC 97-33, December 1997

[3] DESY: TESLA, an International, Interdisciplinary Center for Research. (2001). – http://tesla.desy.de/new_pages/TDR_CD/brochure/

[4] G. ARNISON ET AL.: Experimental Observation of Isolated Large Transverse Energy Electrons with Associated Missing Energy at $\sqrt{s} = 540$ GeV. *Phys. Lett.* B122 (1983), p. 103–116

[5] G. ARNISON ET AL.: Experimental Observation of Lepton Pairs of Invariant Mass around 95 GeV at the CERN SPS Collider. *Phys. Lett.* B126 (1983), p. 398–410

[6] G. ARNISON ET AL.: Observation of the Muonic Decay of the Charged Intermediate Vector Boson. *Phys. Lett.* B134 (1984), p. 469

[7] G. ARNISON ET AL.: Observation of Muonic Z^0 Decay at the $\overline{p}$p-Collider. *Phys. Lett.* B147 (1984), p. 241

[8] M. BANNER ET AL.: Observation of Single Isolated Electrons of High Transverse Momentum in Events with Missing Transverse Energy at the CERN $\overline{p}$p-Collider. *Phys. Lett.* B122 (1983), p. 476–485

[9] P. BAGNAIA ET AL.: Evidence for $Z^0 \rightarrow e^+e^-$ at the CERN $\overline{p}$p-Collider. *Phys. Lett.* B129 (1983), p. 130–140

[10] P. BAGNAIA ET AL.: A Study of High Transverse Momentum Electrons Produced in $\overline{p}$p-Collisions at 540 GeV. *Z. Phys.* C24 (1984), p. 1

[11] F. HALZEN ; A. D. MARTIN: *Quarks and Leptons: An Introductory Course in Modern Particle Physics.* John Wiley & Sons, February 1984. – ISBN 0–471–88741–2

[12] M. PESKIN ; D. V. SCHROEDER: *An Introduction to Quantum Field Theory.* Westview Press, 1995. – ISBN 0–201–50397–2

[13] C. BERGER: *Elementarteilchenphysik.* Springer, Juli 2001. – ISBN 3–540–41515–7

[14] P. SCHMÜSER: *Feynman-Graphen und Eichtheorien für Experimentalphysiker.* Springer, August 1994. – ISBN 3–540–58486–2

[15] R. MOHAPATRA: *Unification and Supersymmetry*. Second Edition. Springer Verlag, 1996

[16] S. L. GLASHOW: Partial Symmetries of Weak Interactions. *Nucl. Phys.* 22 (1961), p. 579–588

[17] A. SALAM ; J. C. WARD: Electromagnetic and Weak Interactions. *Phys. Lett.* 13 (1964), p. 168–171

[18] S. WEINBERG: A Model of Leptons. *Phys. Rev. Lett.* 19 (1967), p. 1264–1266

[19] C. S. WU ; E. AMBLER ; R. W. HAYWARD ; D. D. HOPPES ; R. P. HUDSON: Experimental Test of Parity Conservation in Beta Decay. *Phys. Rev.* 105 (1957), p. 1413–1414

[20] M. ZÖLLER: *Suche nach dem Higgs-Boson in hadronischen Endzuständen mit fehlender Energie bei LEP*, RWTH Aachen, Ph. D. Thesis, 2005

[21] THE SUPER-KAMIOKANDE COLLABORATION: Evidence for an Oscillatory Signature in Atmospheric Neutrino Oscillation. *Phys. Rev. Lett.* 93 (2004), p. 101801

[22] W. GRIMUS: Introduction to Left-Right Symmetric Models. *Lectures given at the 4th Hellenic School on Elementary Particle Physics, Corfu, Greece* (1992)

[23] J. C. PATI ; A. SALAM: Lepton Number as the Fourth Color. *Phys. Rev.* D10 (1974), p. 275–289

[24] R. N. MOHAPATRA ; J. C. PATI: Left-Right Gauge Symmetry and an 'Isoconjugate' Model of CP Violation. *Phys. Rev.* D11 (1975), p. 566–571

[25] R. N. MOHAPATRA ; G. SENJANOVIC: Neutrino Mass and Spontaneous Parity Nonconservation. *Phys. Rev. Lett.* 44 (1980), p. 912

[26] G. SENJANOVIC ; R. N. MOHAPATRA: Exact Left-Right Symmetry and Spontaneous Violation of Parity. *Phys. Rev.* D12 (1975), p. 1502

[27] M. GELL-MANN ; P. RAMOND ; R. SLANSKY: Supergravity. (1979)

[28] T. YANAGIDA: Proceedings of the Workshop on the Baryon Number of the Universe and Unified Theories. (1979)

[29] Z. SULLIVAN: Searching for W' Bosons at Hadron Colliders. (2004), September. – Talk at TeV4LHC Meeting

[30] T. HAN ; H. E. LOGAN ; B. McELRATH ; L.-T. WANG: Phenomenology of the Little Higgs Model. *Phys. Rev.* D67 (2003), p. 095004

[31] Z. SULLIVAN: How to Rule Out Little Higgs (and Constrain Many Other Models) at the LHC. *Proceedings of XXXVIIIth Rencontres de Moriond: QCD*, The Goi Publishers, March 2003, p. 379

[32] G. ALTARELLI ; B. MELE ; M. RUIZ-ALTABA: Searching for New Heavy Vector Bosons in $\overline{\mathrm{p}}$p-Colliders. *Z. Phys.* C45 (1989), p. 109

[33] T. AFFOLDER ET AL.: Search for Quark Lepton Compositeness and a Heavy W' Boson Using the $e\nu$-Channel in $\overline{\mathrm{p}}$p-Collisions at $\sqrt{s} = 1.8$ TeV. *Phys. Rev. Lett.* 87 (2001), p. 231803

[34] C. MAGASS: Analysis in Progress, Private Communications.

[35] P. LANGACKER ; S. UMA SANKAR: Bounds on the Mass of W_R and the W_L - W_R Mixing Angle ξ in General $SU(2)_L \times SU(2)_R \times U(1)$ Models. *Phys. Rev.* D40 (1989), p. 1569–1585

[36] S. EIDELMAN ET AL.: Review of Particle Physics. *Phys. Lett.* B592 (2004), p. 1

[37] G. BEALL ; M. BANDER ; A. SONI: Constraint on the Mass Scale of a Left-Right Symmetric Electroweak Theory from the K_L K_S Mass Difference. *Phys. Rev. Lett.* 48 (1982), p. 848

[38] M. ALLET ET AL.: Search for Right-Handed Weak Currents in the Beta-Asymmetry-Polarization Correlation from N_{12} Decay. *Phys. Lett.* B383 (1996), p. 139–144

[39] THE CMS COLLABORATION: *The Level-1 Trigger – Technical Design Report.* Vol. I. CERN/LHCC 2000-038, December 2000

[40] O. BRUNING ET AL.: *LHC Design Report. Vol. I: The LHC Main Ring*

[41] PIMIA, M. ET AL.: Compact Muon Solenoid. G. JARLSKOG (ed.) ; D. RAIN (ed.): *Proc. Large Hadron Collider Workshop, Aachen* Vol. III, CERN 90-10, October 1990, p. 547

[42] CMS INFORMATION: `http://cmsinfo.cern.ch`.

[43] THE CMS COLLABORATION: *The Tracker System Project – Technical Design Report.* CERN/LHCC 94-38, December 1994

[44] THE CMS COLLABORATION: *The Hadron Calorimeter Project – Technical Design Report.* CERN/LHCC 97-31, June 1997

[45] THE CMS COLLABORATION: *The Magnet Project – Technical Design Report.* CERN/LHCC 97-10, May 1997

[46] THE CMS COLLABORATION: *The Muon Project – Technical Design Report.* CERN/LHCC 97-32, December 1997

[47] THE CMS COLLABORATION: *The Trigger and Data Acquisition Project – Technical Design Report.* Vol. II. CERN/LHCC 2002-026, December 2002

[48] THE CMS COLLABORATION: *Addendum to the CMS Tracker TDR.* CERN/LHCC 2000-016, February 2000

[49] W. FUNK: The Electromagnetic Calorimeter of CMS. *CMS Note* CMS CR-2004/040 (2002)

[50] http://iguanacms.web.cern.ch/iguanacms/

[51] CERN PHOTO DATA BASE: http://cdsweb.cern.ch.

[52] M. BONTENACKELS ; H. REITHLER: Private Communications.

[53] C. ALBAJAR ET AL.: Test Beam Analysis of the First CMS Drift Tube Muon Chamber. *Nucl. Instrum. Meth.* A525 (2004), p. 465–484

[54] G. BRUNO: Resistive Plate Chambers in Running and Future Experiments. *Eur. Phys. J.* C33 (2004), p. s1032–s1034

[55] THE TOTEM COLLABORATION: *TOTEM – Total Cross Section, Elastic Scattering and Diffraction Dissociation at the LHC.* CERN/LHCC 97-49, August 1997

[56] S. KASSELMANN: Private Communications.

[57] http://cmsdoc.cern.ch/cmsoo/projects/CMKIN/index.html

[58] T. SJOSTRAND ; P. EDEN ; C. FRIBERG ; L. LONNBLAD ; G. MIU ; S. MRENNA ; E. NORRBIN: High-Energy-Physics Event Generation with PYTHIA 6.1. *Computer Physics Communications* 135 (2001), p. 238

[59] T. SJOSTRAND ; L. LONNBLAD ; S. MRENNA: PYTHIA 6.2: Physics and Manual. *hep-ph/0108264* (2001)

[60] G. MARCHESINI ET AL.: HERWIG: A Monte Carlo Event Generator for Simulating Hadron Emission Reactions with Interfering Gluons. Version 5.1 – April 1991. *Comput. Phys. Commun.* 67 (1992), p. 465–508

[61] S. R. SLABOSPITSKY ; L. SONNENSCHEIN: TopReX Generator (version 3.25). Short Manual. *Computer Physics Communications* 148 (2002), p. 87

[62] http://cmsdoc.cern.ch/oscar/

[63] S. AGOSTINELLI ET AL.: GEANT4: A Simulation Toolkit. *Nucl. Instrum. Meth.* A506 (2003), p. 250–303

[64] http://cmsdoc.cern.ch/orca/

[65] THE CMS COLLABORATION: ORCA – User Guide. (2005). – http://cmsdoc.cern.ch/orca

[66] THE CMS COLLABORATION: *The Computing Project – Technical Design Report.* CERN/LHCC 2005-023, June 2005

[67] I. BELOTELOV ; N. NEUMEISTER: Performance of the CMS Offline Muon Reconstruction Software. *CMS Note* 010 (2005)

[68] THE CMS COLLABORATION: *CMS Physics – Technical Design Report.* Vol. I. CERN/LHCC 2006, 2005

[69] THE CMS COLLABORATION: *CMS Physics – Technical Design Report.* Vol. II. CERN/LHCC 2006, 2005

[70] S. LACAPRARA ; I. BELOTELOV ; N. NEUMEISTER ; T. COX ; U. GASPARINI: Private Communications.

[71] D. BOURILKOV: TeV Muons. . – Talk given at the CMS Physics Week, April 2005, FNAL

[72] P. TRACZYK: *Optimizing Global Muon Reconstruction for TeV Muons.* December 2004. – Talk given at PRS-Muon Meeting, CERN

[73] R. COUSIN ; J. MUMFORD: *Progress in Fitting High-Momentum Muons in ORCA.* September 2003. – Talk given at PRS-Muon Meeting, CERN

[74] N. AMAPANE ET AL.: Monte Carlo Simulation of Inclusive Single- and Di-Muon Samples. *CMS Note* 041 (2002)

[75] N. AMAPANE ; M. FIERRO ; M. KONECKI: High Level Trigger Algorithms for Muon Isolation. *CMS Note* 040 (2002)

[76] A. L. READ: Presentation of Search Results: The CL_s Technique. *J. Phys.* G28 (2002), p. 2693–2704

[77] E. GROSS ; A. L. READ: Prospects for Standard Model Higgs Search in the LEP 2000 Run. *Proceedings of 14th Rencontres de Physique de la Valle d'Aoste: Results and Perspectives in Particle Physics, La Thuile, Valle d'Aoste, Italy* (2000), February/March

[78] A. L. READ: Modified Frequentist Analysis of Search Results (The CL_s Method). (2000), January. – Prepared for Workshop on Confidence Limits, Geneva, Switzerland

[79] G. COWAN: *Statistical Data Analysis.* Oxford University Press, New York, 1998

[80] S. BRANDT: *Statistical and Computational Methods in Data Analysis.* Springer, New York, 1997

[81] A. FAVARA ; M. PIERI: Optimal Statistical Analysis of Search Results. (1997). – L3 Internal Note 2066

[82] `http://cmsdoc.cern.ch/cms/production/www/html/general/index.html`

[83] `http://cmsdoc.cern.ch/swdev/lxr/ORCA/source/ORCA/src/?v=snapshot`

[84] C. ALBAJAR ; G. WROCHNA: Isolated Muon Trigger. *CMS Note* 067 (2000)

[85] M. KRONECKI: Private Communications.

[86] S. ABDULLIN ET AL.: Summary of the CMS Potential for the Higgs Boson Discovery. *Eur. Phys. J.* C39S2 (2005), p. 41–61

[87] A. Tricomi: Performance of the ATLAS and CMS Silicon Tracker. . – Talk and Proceedings EPS 2003, Aachen

[88] J. Pumplin et al.: New Generation of Parton Distributions with Uncertainties from Global QCD Analysis. *JHEP* 07 (2002), p. 012

[89] LEP Electroweak Working Group: A Combination of Preliminary Electroweak Measurements and Constraints on the Standard Model. *CERN-PH-EP/2004-069* (2004)

List of Figures

List of Tables

Acknowledgements